UTERINE FOLDS: ROLE IN EMBRYO-UTERINE ORIENTATION AND IMPLANTATION CHAMBER FORMATION DURING EARLY PREGNANCY

By

Manoj Krishna Madhavan

A DISSERTATION

Submitted to
Michigan State University
in partial fulfillment of the requirements
for the degree of

Biomedical Engineering – Doctor of Philosophy

2023

ABSTRACT

During morphogenesis 2D epithelial tissue undergo architectural changes to form 3D structures called folds. Epithelial folding is essentially origami where a 2D sheet of paper can be transformed via folding and sculpting into a 3D structure. Folding is a key phenomenon during embryogenesis and organogenesis and is essential for several physiological functions. For example, folds in the stomach (rugae) and intestine (crypts) increase surface area for nutrient absorption and in the brain increase cortical surface area for neural processing. The uterine luminal epithelium in mammals including humans, horses and rodents undergoes structural changes to form folds. Although improper uterine folding in horses results in pregnancy failure, the precise role of folds in embryo implantation remains unknown. Using a focused time course around implantation in the mouse model, we uncover dynamic changes in the 3D uterine structure with the entire lumen forming pre-implantation transverse folds along the mesometrial-antimesometrial axis. During embryo-implantation the mouse uterine lumen forms a second structure called an implantation chamber. Whether uterine folds transform into implantation chambers has not been investigated. Using quantitative 3D methods, we show that uterine transverse folds are formed prior to spacing of embryo clusters whereas chambers form once an embryo begins to attach to the uterus and thus are two distinct structures. We also show that transverse folds resolve to form a flat implantation region before an embryo arrives in the center of this region (the implantation site) to form a post-implantation chamber. Although, it is known that the mouse embryo aligns itself along the uterine mesometrial-antimesometrial axis, our data suggests that the implantation chamber facilitates embryo rotation to enable embryo-uterine axes alignment. Further,

using mice deficient in WNT5A and RBPJ as models of aberrant uterine folding, we show that embryos get trapped in longitudinal folds leading to embryo-uterine axes misalignment, abnormal chamber formation and defective post-implantation embryo morphogenesis. Further, we show that increased estrogen signaling and reduced progesterone signaling lead to aberrant longitudinal folds. Finally, we extend our findings to examine the effects of excess estrogen signaling on folding during hyperstimulation – a clinical procedure performed during In Vitro Fertilization (IVF) to increase egg numbers for higher success rate of implantation and pregnancy. In women, pregnancies following hyperstimulation often lead to preterm birth, placental abnormalities, and other complications. Our findings suggest that hyperstimulation in mice leads to longitudinal folds and downstream pregnancy loss due to embryo trapping. Such research can be potentially used to improve pregnancy outcomes following IVF and fresh embryo transfer. Our mouse models with disrupted uterine folds provide an opportunity to understand uterine structure-based mechanisms crucial for implantation and pregnancy success. In addition to fueling future research on endometrial folds in humans, our research will open up new avenues for the treatment of infertility and provide new targets for diagnosis based on uterine 3D structure.

ACKNOWLEDGEMENTS

I would like to express my deepest gratitude to my advisor, Dr. Ripla Arora for her guidance and support during my PhD. Her passion and enthusiasm for her work has inspired and motivated me to be a scientific researcher. I have learnt a lot from her including critical thinking, scientific writing and mentorship. She has always encouraged me to come up with challenging ideas that has helped propel my research forward. In addition to being a mentor, she has also been a good friend who has been very kind and understanding.

I would like to thank Dr. Diana Flores and Sarah Fitch for training me and helping me get started in the lab. I would like to thank Maddie Dawson and Kaylie Chiles for assisting me with my experiments when I was away from the lab. I would like to thank Noura Massri, Hannah Lufkin, Katrina Granger, Lindsey Royer and all the other Arora lab members (previous and current) for helping with my experiments.

I would like to thank Dr. Asgi Fazleabas and his lab members for providing me with $Rbpj^{cKO}$ mouse line, baboon samples and uterine samples. I would also like to thank the Fazleabas lab for their suggestions and valuable advice in joint meetings. I would like to thank Dr. Amy Ralston and her lab for their valuable advice and providing us with antibodies. I would like to thank Dr. Emmanuel Paul for helping me with the single cell sequencing analysis. I would like to thank my committee members Dr. Christina Chan, Dr. Aitor Aguirre and Dr. Sudin Bhattacharya for their guidance and advice during my PhD.

Finally, I would like to thank my friends and family for their support and encouragement.

PREFACE

Uterine folds have been observed in humans during the luteal phase but their role in implantation and pregnancy remain unknown. Our study is the first to provide evidence for the detrimental effects of aberrant uterine folding pattern on implantation chamber formation, embryo-uterine orientation and embryo morphogenesis during early pregnancy. Chapter 1 introduces the concept of epithelial folds and uterine folds. The first section of Chapter 1 demonstrates the known existence and significance of epithelial folds in different organs. The second section of Chapter 1 delves into the available literature on uterine folds in humans, mice and other species and sets the basis for the studies conducted in this thesis. Finally, the third section of Chapter 1 provides a detailed review on the mechanisms of folding during morphogenesis and organogenesis in various tissue structures and organs. Chapter 2 details the materials and methods that were used in the study. In Chapter 3, we performed a fine time course analysis of luminal folding dynamics and its relationship to embryo location. We introduce the two major orientation of folds – transverse folds and longitudinal folds, and how these two types of folding pattern change with timing of pregnancy. In Chapter 4, using two mouse models deficient for WNT5A and RBPJ, we explain how aberrant folding affects embryo-uterine axes alignment and chamber formation leading to pregnancy loss. Chapters 3 and 4 have been published in "Manoj K. Madhavan, Francesco J. DeMayo, John P. Lydon, Niraj R. Joshi, Asgerally T. Fazleabas, Ripla Arora; Aberrant uterine folding in mice disrupts implantation chamber formation and alignment of embryo-uterine axes. *Development* 1 June 2022; 149 (11): dev200300. doi: https://doi.org/10.1242/dev.200300". Further, in Chapter 5, we delve into the role of ovarian hormones - estrogen and progesterone in regulating folding pattern.

Finally, in Chapter 6, we explain the clinical significance of our findings using the hyperstimulation mouse model where hormone levels are dysregulated and that impacts uterine folding. We end with an eye to the future in Chapter 7 where we discuss the applications of our work and propose potential experiments to build on our findings.

TABLE OF CONTENTS

LIST OF ABBREVIATIONS

ACTA2	Alpha Smooth Muscle Actin
ART	Assisted Reproductive Technologies
E2	Estrogen
ECM	Extra Cellular Matrix
Em-AbEm	Embryonic – Abembryonic axis
Esr	Estrogen receptor
GD	Gestational day
IIR	Inter-Implantation Region
IVF	In Vitro Fertilization
M-AM	Mesometrial – Antimesometrial axis
P4	Progesterone
PCP	Planar Cell Polarity
Pgr	Progesterone receptor
PIR	Peri-Implantation Region

Chapter 1: Introduction to epithelial folds and uterine folds

1.1 Epithelial Folds

1.1.1 Definition and structure

Epithelial tissue is a thin layer of squamous, cuboidal or columnar epithelial cells that line the internal surface of organs and body cavities as well as the external surface of multicellular organisms including both vertebrates (humans, mice, drosophila, etc.) and invertebrates. In the body, epithelium has multiple roles including secretion, absorption, transport, filtration and protection from external environment. During body morphogenesis and organogenesis, epithelial tissue undergoes dynamic morphological changes to form structures called **folds** to facilitate specific functions and processes. **Epithelial folds** are invaginations or indentations on the surface of simple linear epithelium which gives rise to complex 3D patterns. Folds are formed as a result of an interplay of multiple biochemical and mechanical processes. Changes in cell shape and orientation are triggered by biochemical pathways and the resulting physical forces shape tissues. Mechanical forces in tissues arise due to contraction and relaxation of cells, changes in cell shape, changes in extra-cellular matrix stiffness, etc. Moreover, the mechanical forces that cause epithelial folds can be generated locally from the epithelial cells involved in the fold formation or globally from the surrounding cells and tissue layers (Tozluoğlu and Mao, 2020). Since epithelial cells are connected to each other via intercellular junctions, mechanical forces generated by a cell or a group of cells are transmitted across the entire layer and to surrounding cell layers (Chanet and Martin, 2014).

1.1.2 Epithelial folds in various organs - significance for disease and therapeutics

Epithelial folding morphogenesis is a key phenomenon that occurs in several species including humans, mice and drosophila, and is important for shaping and sculpting tissues and organs. Epithelial folding is a prominent event during embryo morphogenesis, specifically during gastrulation and neurulation, contributing to body shape and organ structure. In addition to its role in embryonic development, epithelial folding is a characteristic feature of a variety of organs including the gut, stomach, bladder, airway, brain, uterus and fallopian tube.

a. Intestine and stomach

In the digestive tract, epithelial folds exist in the form of intestinal villi and stomach rugae which increase surface area for absorption of nutrients. Defective villi formation leading to intestinal failure causes short bowel syndrome and intestinal pseudo-obstruction syndrome (Goulet et al., 2004). Rugae or folds in the stomach also facilitate expansion and stretching of lumen when food enters to increase volume without affecting pressure. Thickened rugae leading to inflammation of the stomach is a common observation in conditions such as gastritis and gastropathies (Agarwala et al., 2018).

b. Brain and spinal cord

Neurulation involves bending or folding of the neuroepithelium to enable neural tube closure, eventually leading to the formation of brain and spinal cord. Defective neural tube closure leads to neural tube defects (NTDs) such as spina bifida and anancephely (Botto et al., 1999). NTDs are one of the most common birth defects worldwide and hence understanding the mechanisms of neural tube closure is critical for advancing treatment of NTDs. Gyrification of the brain leading to the formation of folds or wrinkles in the cerebral cortex of brain allow for increased cognitive function (Borrell, 2018). Excessive folding or reduced folding is a sign of poor cognitive development. For example, in Polymicrogyria, the brain develops too many folds that are smaller and fused during neonatal development leading to cognitive issues (Jansen and Andermann, 2005). Recently, Transmembrane Protein 161B (TMEM161B) has been shown to be critical for determining the number of folds in the neocortex of human brain (Wang et al., 2023). Such discoveries can help in developing treatments for aberrant folding related brain disorders.

c. Lung and airway

In the lungs, during alveologenesis, new alveoli are formed by secondary septation of the alveolar sacs. The alveolar epithelial cells fold to form secondary septa giving rise to more alveoli which greatly increase the surface area for gas exchange. Defective alveologenesis leading to simplification of alveoli is a cause of bronchopulmonary dysplasia (BPD) in premature infants (Branchfield et al., 2016; Jobe, 1999). The airway mucosal epithelium also forms folds that protrude into the lumen of the airway tube (Wiggs et al., 1997). Excessive folding or thickened folds can also be detrimental in the case of the airway leading to conditions such as asthma (Veerati et al., 2020).

d. Female reproductive tract - fallopian tube, uterus and cervix

The mucosal epithelium in the fallopian tube in humans (uterine tube), mice (oviduct) and cows forms multiple longitudinal folds which play a role in gamete transportation, fertilization and early embryonic development (Shi et al., 2014; Varga et al., 2018). Thickened or inflamed longitudinal folds in the human and bovine fallopian tube is indicative of an underlying pathological condition such as salpingitis (Benjaminov and

Atri, 2004). In the mouse oviduct, deletion of flamingo genes, leads to ectopic branches in the folds compromising oocyte transport and pregnancy (Shi et al., 2014). The epithelium of the uterus, cervix and vagina also form folds (Sokol, 2011). A detailed review of uterine folds in provided in chapters 1.2.

1.2 Uterine folds

1.2.1 Definition and structure

The uterus in humans and other mammals is composed of two layers - the endometrial layer which includes the stroma and the epithelium, and the myometrial layer. The epithelium of the endometrial layer lines the uterine cavity. In humans and horses, using ultrasound, the morphology of the endometrial layer is characterized based on (1) echogenicity, which is the ability of tissue to return the signal during ultrasound examination and (2) appearance of the midline or interface between the endometrial lining on either sides of the uterine cavity (Leone et al., 2010). The morphology of the endometrium is considered regular if it has a linear midline formed by uniform hyperechogenic boundaries. On the other hand, it is considered irregular if it has a wavy non-linear midline formed by non-uniform hyperechogenic boundaries. These irregularities in the surface of the endometrium are defined as '**uterine folds**' or '**endometrial folds**'. In other mammals including mice, rats and rabbits, uterine folds have been described as irregular appearance of the endometrial lining based on 2D histological sections (Abd-Elkareem, 2017; Enders, 1975; Winkelmann and Spornitz, 1997).

1.2.2 Uterine (Endometrial) folds in humans - history and evidence

In humans, the earliest evidence of uterine (endometrial) folds dates back to 1973, when longitudinal folds were discovered in the uterine cavity of women using hysterography in both the proliferative and secretory phase of the menstrual cycle (Slezak and Tillinger, 1973). The longitudinal folds are about 5-10mm and run parallel to the long axis of the uterine cavity (Slezak and Tillinger, 1973). Although initially the folds were thought to be defects associated with a pathological condition, the endometrium was found to be of normal thickness. The study concluded that folds were not caused due to any pathological changes or menstrual irregularities (Slezak and Tillinger, 1973). In 1994, Goldstein discovered folds or irregularities in the lining of the endometrium using ultrasonohysterography, and called them ‘endometrial moguls’ (Goldstein, 1994). Goldstein also implicated that the moguls (or folds) are different from endometrial polyps or hyperplasia and are a normal occurrence during the late proliferative and secretory phases (Goldstein, 2010). In 2015, an observational study was performed used saline infusion sonohysterography (SIH) to describe the morphology of the endometrium in women during the luteal phase of menstrual cycle. Out of the 26 women with regular menstrual cycles included in the study, 12 (46%) of them had endometrial folds. The study also showed that endometrial folds occurred in women during the luteal phase irrespective of uterine pathology (Jokubkiene et al., 2015). There was no significance difference in the endometrial thickness between women that had folds and those that did not. In addition, the number of folds ranged between 1-6 with a median of 3 folds. The study does not distinguish why folds occur only in some women and not the others and whether folds occurred during the other phases of menstrual cycles such as the proliferative phase was also not studied. Due to limitations of current technologies and ethical concerns associated with research in pregnant women, how endometrial folds form during the window of implantation, and their function in pregnancy remains unknown.

1.2.3 Uterine folds across other species

a. Horses

Uterine folds have been detected in mares using ultrasound. The presence or absence of folds in the uterus is visualized using echogenicity and is used to determine the stage of menstrual cycle. The diestrus stage is characterized by absence of distinct endometrial folds where the lumen is uniformly echogenic. In contrast, the estrus stage is characterized by the presence of prominent endometrial folds where the lumen is unevenly echogenic (Ginther and Pierson, 1984). Interestingly, the endometrial folds in mares during the estrus cycle have a cartwheel appearance with hyperechogenic borders and hypoechogenic centers (Samper, 2010).

A study on physical examination methods of mare uterus for breeding studies also describes the presence of numerous folds that are edematous during the estrus cycle. The number of folds is minimal as estrus progresses and ovulation starts. Interestingly, the folds disappear when the progesterone levels are high after formation of the corpus luteum (Hagstrom, 2003).

b. Cows

In the non-pregnant bovine uterus, using ultrasonography, endometrial folds are clearly visible during the estrous phase and are occasionally visible during the diestrus phase.

Interestingly, during early pregnancy around the time of embryo implantation, the endometrium appears smooth and folds are absent (Fissore et al., 1986). However, another study found prominent circular folds in the pregnant bovine uterus using 3D nuclear magenetic resonance imaging. The folds are about 2-3cm long and protrude at right angles to the uterine wall dividing the uterus into pockets (Kähn et al., 1989).

c. Rodents – rat and mouse

Using 2D histological analysis, several studies have observed invaginations (folds) in the rat and mouse uterus (Akinloye and Oke, 2015; Cha et al., 2014; Enders, 1975; Zhang et al., 2014). Uterine folds were detected in the pregnant rat uterus using scanning electron microscopy (SEM). Folds were detected in the luminal epithelium using changes in alkaline phosphatase activity on the surface of luminal epithelial cells as captured by SEM. Interestingly, during the pre-implantation period (GD5), luminal folds were shown to divide the uterine horn into 'implantation segments'(Winkelmann and Spornitz, 1997). In mice, uterine folds are commonly referred to as crypts in the literature. Several genes including *Wnt5a*, *Rbpj* and *Msx* have been shown to important for uterine fold formation (Cha et al., 2014; Daikoku et al., 2011; Zhang et al., 2014). More recently, with advances in microscopy, the structure of uterine folds have been described in 3D (Arora et al., 2016). This study has opened doors for understanding the role of folds in the uterus especially during pregnancy. While there is limited knowledge on uterine folds, there is a plethora of research that has been done on understanding mechanisms of folding in several other tissue structures and organ systems. A review on the mechanisms of epithelial folding has been provided in chapter 1.3.

1.3 Mechanisms of epithelial folding

1.3.1 Forces generated locally by epithelial cells - Apical-basal polarity mediated folding

An intrinsic property of epithelial cells is apical-basal polarity and cell-cell adhesion through junction proteins. Apical-basal polarity is established in epithelial cells due to the differential localization of proteins along the apical-basal axis whereas Planar Cell Polarity (PCP) is established due to differential localization of proteins along the plane of the epithelial sheet perpendicular to the apical-basal axis. In addition to polarity, cell-cell adhesion is another defining property of epithelial cells. Cell adhesion is regulated by tight junctions (e.g. Occludins, Claudins), adherens junctions (e.g. Cadherins), gap junctions (e.g. Connexins) and desmosomes. In particular, the tight junctions and adherens junctions together comprise the apical junctions and define apical-basal polarity of cells. The intra-cellular domain of adherens junction (AJ) proteins such as E-Cadherin anchors the actin-myosin cytoskeletal networks towards the apical side of the cell. Apical-basal polarity of epithelial cells contributes to fold formation via several mechanisms including apical constriction, apoptosis, apical junction shifting and basal polarity.

a. Apical constriction

Apical constriction has been shown to play key role in the formation of folds in several morphogenetic events such as gastrulation in embryos and neurulation in vertebrate embryos (Heer et al., 2017). Apical constriction is a change in cell architecture from cuboidal or columnar to a wedge shape. Apical constriction is caused due to accumulation of non-muscle myosin II at the apical end followed by contraction of the actin-myosin cytoskeletal networks. The resulting forces are transmitted to the apical circumference of the cell, which in turn are transmitted to the neighboring cells via adherens junctions. These events lead to the shrinkage of the epithelial cell on the apical side facing the lumen followed by a series of events including basal relaxation, lateral shortening and volume conservation to affect the formation of a fold (Fig. 1.1A). During gastrulation in Drosophila, RhoA signaling through ROCK is required for activation of myosin II through phosphorylation of the myosin light chains which in turn cause actomyosin contractions that mediate mesodermal folding. Additionally, RhoA signaling through Dia is required for the organized assembly of F-actin filaments (Martin and Goldstein, 2014). Shroom, an actin binding protein has been shown to be critical for apical constriction in several structures including lens placode invagination, gut folding and neural tube closure (Haigo et al., 2003; Hildebrand and Soriano, 1999; Plageman Jr et al., 2010). During neural tube closure in Xenopus, expression of Shroom causes apical accumulation of actin filaments leading to bending of neuroepithelial sheets. Interestingly, Shroom can only cause apical actin accumulation in polarized epithelial cells suggesting that Shroom mediated apical actin accumulation is dependent on the apical-basal polarity of epithelial cells (Haigo et al., 2003). This is further supported by studies using Shroom deficient mice (*shrm* $^{-/-}$), which show that polarity of neuroepithelial cells is disrupted when *shrm* is knocked out (Hildebrand and Soriano, 1999). During lens placode formation in mice, Shroom3 expression is mediated by Pax6 and Sox2 (Plageman Jr et al., 2010). Other studies have shown that Shroom3 also facilitates apical constriction via Rho-ROCK signaling. In chick embryo neural tube formation, Shroom3 and ROCK colocalize in the apical junctions of neuroepithelial cells (Nishimura and Takeichi, 2008). In the absence of Shroom3, ROCK is localized throughout the epithelial cell whereas in the presence of Shroom3, ROCK is localized specifically to the apical side suggesting that Shroom3 recruits ROCK to the apical junctions to mediate acto-myosin contractions. Live imaging studies have shown that the actin-myosin contractions that cause apical constriction are pulsatile in nature. In addition these studies have shown that Snail and Twist are required to initiate and maintain the contractions that cause the constricted shape of the cell (Martin et al., 2009).

b. Apoptosis

Apoptosis or programmed cell death in combination with apical constriction plays an important role in fold formation in several structures including the leg imaginal disc in drosophila embryos and neural tube bending in chick embryos (Manjón et al., 2007; Roellig et al., 2022). The apoptotic cell generates a myosin cable that spans the length of the cell along the apical-basal axis causing a pulling force at the apical end (Monier et al., 2015). Since the myosin cable is also connected to the adherens junctions, the pulling force from the dying cells forms an adhesion peak with the neighboring cells. The adhesion peak results in the formation of junctions between the neighboring cells surrounding the apoptotic cell. In addition, the apical-basal myosin cable is also connected to the adhesion peak. The pulling force generated by the cable leads to extrusion of the dying cell which leads to apical myosin accumulation in the neighboring cells leading to apical constriction and generation of a fold (Fig. 1.1B). Other studies have shown that the actomyosin networks in the apoptotic cell form an inner ring at the apical end which in turn triggers an outer ring of actomyosin cables in the neighboring cells. The acto-myosin contractions from the outer ring in the neighboring cells cause apoptotic cell extrusion. Sphingosine-1-phosphate (S1P) pathway has been shown to crucial for the formation of the outer acto-myosin ring (Gu et al., 2011). S1P accumulates in the apoptotic cell and binds to S1P receptors in the neighboring cells. Moreover, inhibition of S1P pathway prevents formation of outer ring and cell extrusion. In Drosophila, Hox genes regulate apoptosis for folding during head morphogenesis. In the head lobes, the boundary between the maxillary and mandibular subunits is formed by induction of *reaper (rpr)*, a pro apoptotic factor, by the Hox gene *deformed (Dfd) (Lohmann et al., 2002).*

c. Apical junction shifting

In addition to apical constriction, modifications to apical-basal polarity have also been shown to mediate fold formation. Adherens junctions and tight junctions are the two major types of apical junction proteins that maintain the apical-basal polarity of cells. Apical junctions play a key role in epithelial cell polarity by anchoring actin complexes towards the apical side of the cell. During gastrulation in Drosophila embryos, dorsal fold formation occurs via apical junction shifting (Wang et al., 2012). The adherens junctions of the initiating cell are shifted towards the basal end while the adherens junctions in the neighboring cells remain in the apical end. This shift alters the apical shape of the initiating cell thereby forcing the lateral membrane of neighboring cells to readjust towards the initiating cell resulting in the formation of a fold (Fig. 1.1C). In the gastrulating Drosophila embryo, Par-1 signaling is downregulated in the initiating epithelial cells to enable apical junction shifting (Wang et al., 2012). The decrease in levels of Par-1, which is normally localized in the basolateral end, results in basal shift of adherens junctions. The subsequent apical surface shift leads to cell shortening and initiation of fold formation. Par-3/Bazooka (Baz) also plays a key role in apical junction shifting during mesodermal folding (Weng and Wieschaus, 2017). Baz is normally localized between the apical and basal boundaries in mesodermal epithelial cells and is responsible for maintaining the adherens junctions between cells. However, in the presence of Snail (Sna), Baz expression is reduced at the subapical sites leading to disassembly of adherens junction. Following activation of actomyosin contractions, the adherens junctions shift basally and Baz localization is repositioned to subapical sites resulting in cell shrinkage. Patronin has also been shown to mediate basal polarity shift in the drosophila embryo by modulating the microtubule networks in the apical end which generate the constricting forces for cell shortening (Takeda et al., 2018).

d. Basal constriction

Fold formation can also occur independent of apical mechanisms. Basal constriction mediates fold formation in several structure including intestinal epithelium, optic cup formation and brain boundary formation in zebrafish and bud formation in Hydra (Bogdanović et al., 2012; Holz et al., 2017). In the zebrafish midbrain-hindbrain boundary (MHB), the neuroepithelium folds basally via basal constriction (Gutzman et al., 2008). The initiating cells shorten in length which causes apical expansion and basal shortening. Basal shortening is further supported by interactions between integrins in the basal membrane and laminin networks in the basement membrane of the neuroepithelium. This is supported by studies using laminin mutants that fail to undergo basal constriction. Further, integrin adhesion to the basement membrane causes actin filaments to align with the ECM in the basement membrane. The aligned actin-myosin networks cause oscillatory contractions in the basal surface leading to basal constriction (Fig. 1.1D) (He et al., 2010). Other studies have shown that Wnt5b-JNK signaling is required for microtubule stabilization which mediates basal constriction and apical expansion of neuroepithelial cells (Visetsouk et al., 2018). Wnt5b is required for microtubule polymerization in the basal domain of cells to regulate basal anisotropic cell shape change.

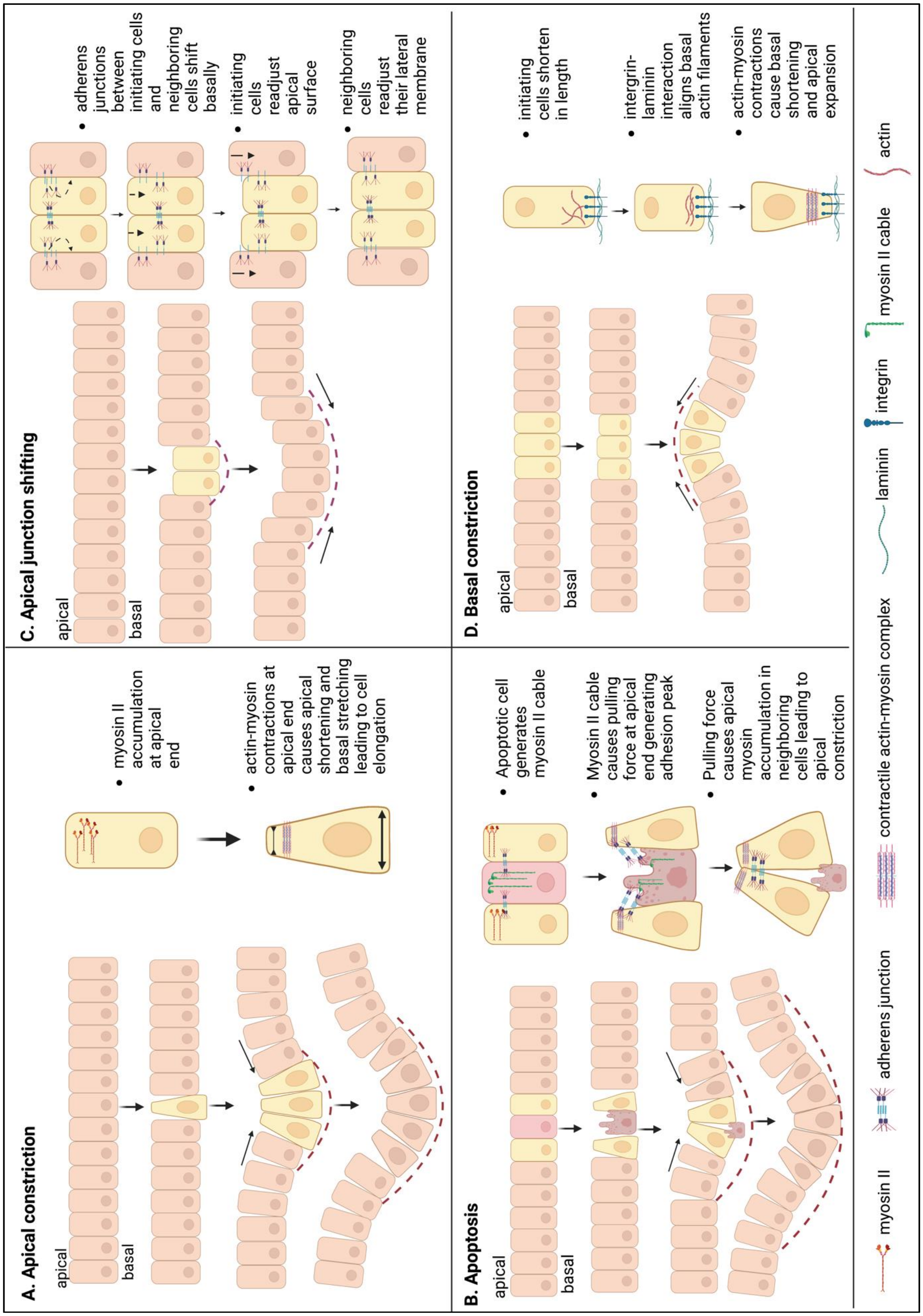

Figure 1.1: Diagrammatic representation of apical-basal polarity mediated mechanisms of epithelial folding.

Figure 1.1 (cont'd)
(A) Apical constriction - Myosin II accumulation at apical end causes actin-myosin contractions followed by apical shortening and basal stretching leading to cell elongation. (B) Apoptosis - Apoptotic cell generates myosin II cable which causes pulling force at apical end generating an adhesion peak. The pulling force causes apical myosin accumulation in neighboring cells leading to apical constriction. (C) Apical junction shifting - The adherens junctions between initiating cells and neighboring cells shift basally which forces the initiating cells readjust apical surface. The neighboring cells then readjust their lateral membrane leading to the formation of a fold. (D) Basal constriction -The initiating cells shorten in length causing basal shortening. This is followed by integrin-laminin interactions which cause alignment of basal actin filaments and the resulting actin-myosin contractions cause further basal shortening and apical expansion.

1.3.2 Forces generated from surrounding cells – buckling effect

Buckling is the bending of an elastic tissue caused due to compressive force or stress. The force is usually in-plane stress which causes out-of-plane buckling. Epithelial tissue are usually thin layers and hence are easily malleable to external forces. The compressive forces can either arise from the epithelial layer and/or from surrounding layers such as the mesenchyme and muscle. In addition, differential growth rate of the different layers can also cause epithelial buckling.

a. PCP mediated folding

PCP is established in epithelial cells due to differential localization of proteins along the plane of the epithelial sheet perpendicular to the apical-basal axis (Zallen, 2007). The asymmetry in the expression of PCP components in a cell also affects the polarity of neighboring cells. Hence, while apical-basal polarity is a local property of an epithelial cell, PCP is a global property of a sheet of epithelial cells. PCP plays an important role in neural tube folding during neurulation in several species including drosophila, mouse, chick, xenopus and zebrafish. Deletion of PCP components such as Vangl2, Frizzled, Celsr, Dishevelled and Prickle leads to defective neural tube folding and closure. During Xenopus neural tube closure, polarization of Rab11 along the planar axis is mediated by PCP pathway and is required for neural tube folding by apical constriction (Ossipova et al., 2014). In the mouse oviduct, well aligned longitudinal epithelial folds are crucial for the transport of embryos into the uterus. Interestingly, knockout of *Celsr1,* a gene involved in the PCP pathway, causes defective epithelial folds with ectopic branches. Using mathematical modeling, it was shown that the ratio of epithelium length to smooth muscle length, along with PCP is necessary for aligned fold formation. Defective cell polarization in the *Celsr1* mutants leads to decreased epithelial tension along the longitudinal direction and increase in epithelium to smooth muscle length ratio, leading to defective folding. Thus differential increase in epithelial length compared to smooth muscle length leads to a buckling effect along the longitudinal direction leading to formation of folds with ectopic branches (Koyama et al., 2016).

b. Smooth muscle compression

In many tissues including the lung, uterus, intestine, ureter, etc., epithelial layers are usually surrounded by mesenchyme and/or muscle. In the developing lung, airway. epithelial branching is achieved by budding followed by bifurcations to form branches. The buds are essentially folds formed on the airway epithelial tube. The epithelium is surrounded by a thick layer of mesenchyme which sequentially differentiates into smooth muscle cells. In the mouse embryonic lung, it was shown that the pattern of smooth muscle layer differentiation is essential for shaping the epithelial buds (Kim et al., 2015). Moreover, disruption of smooth muscle differentiation leads to deformed epithelial buds. Thus, the constriction of the growing airway epithelium by the smooth muscle layer is essential for bud formation and patterned branching.

In structures such as the intestine, fallopian tube and uterus, the epithelium is surrounded by mesenchyme and two different layers of smooth muscle – circular smooth muscle and longitudinal smooth muscle. In the developing chick gut, patterned smooth muscle differentiation dictates the shape of the epithelial folds which eventually transform into crypts or villi (Shyer et al., 2013). The initial formation of the circular smooth muscle layer causes the formation of longitudinal folds or ridges in the epithelium. Later, the formation of the first longitudinal smooth muscle layer transforms the ridges into a zigzag pattern.

The zigzag pattern is then transformed into a villus like structure with the formation of the second longitudinal layer. Moreover, physical separation of the muscle from the epithelium and mesenchyme causes the epithelial folds to collapse further showing that the muscle layer is crucial for epithelial buckling in the gut. Similarly, the airway mucosal epithelium forms folds that protrude into the lumen due to smooth muscle constriction (Wiggs et al., 1997). Using mathematical modeling, buckling of airway epithelium has been shown to arise due to changes in airway wall dimensions and stiffness of wall materials. These studies point to the role of smooth muscle layers in sculpting the 3D shape of epithelial tubes though compressive stress mediated buckling (Fig. 1.2A).

c. Extracellular matrix compression

Elasticity and stiffness of ECM also dictates fold formation. Extracellular matrix (ECM) remodeling plays a key role in Drosophila wing elongation and fold formation. Wing elongation is mediated by epithelial cell shape change from columnar to cuboidal which expands the apical surface area of each cell. The wing epithelium is surrounded by ECM on both the apical and basal sides. In order to achieve the columnar to cuboidal transition, the ECM on either side is degraded. Using ex vivo culture experiments, wings grown in the presence of inhibitors of matrix remodeling fail to initiate columnar to cuboidal transition and hence fail to undergo elongation (Ray et al., 2018). Further, using computational modeling, it was shown that the three folds in the wing imaginal disc of drosophila are formed as a result of differential growth of the wing epithelium under compression of the ECM in the basement membrane. The increase in the stiffness of the actomyosin complex at the apical end combined with constriction from the basement membranes on either ends drive the formation of folds from the apical end (Tozluoğlu et al., 2019). Mesenchymal condensation at the epithelial-mesenchymal interface facilitates fold formation in the mouse gut villi and chick skin (Hughes et al., 2018). Condensation of mesenchymal cells at the region of fold initiation leads to compaction and alignment of the extracellular matrix fibers along the curvature of fold formation. The resulting change in the elasticity of the underlying mesenchyme due to compaction of the ECM leads to bending of the epithelium (Fig. 1.2B). Trushko et al., used in vitro culture of epithelial monolayers enveloped by spherical alginate gel to show that folds can be induced by buckling due to confinement. Here, the alginate gel resembles a stiff basement membrane and the differential growth of epithelial cells due to proliferation in a confined space leads to folding of the epithelial layer (Trushko et al., 2020).

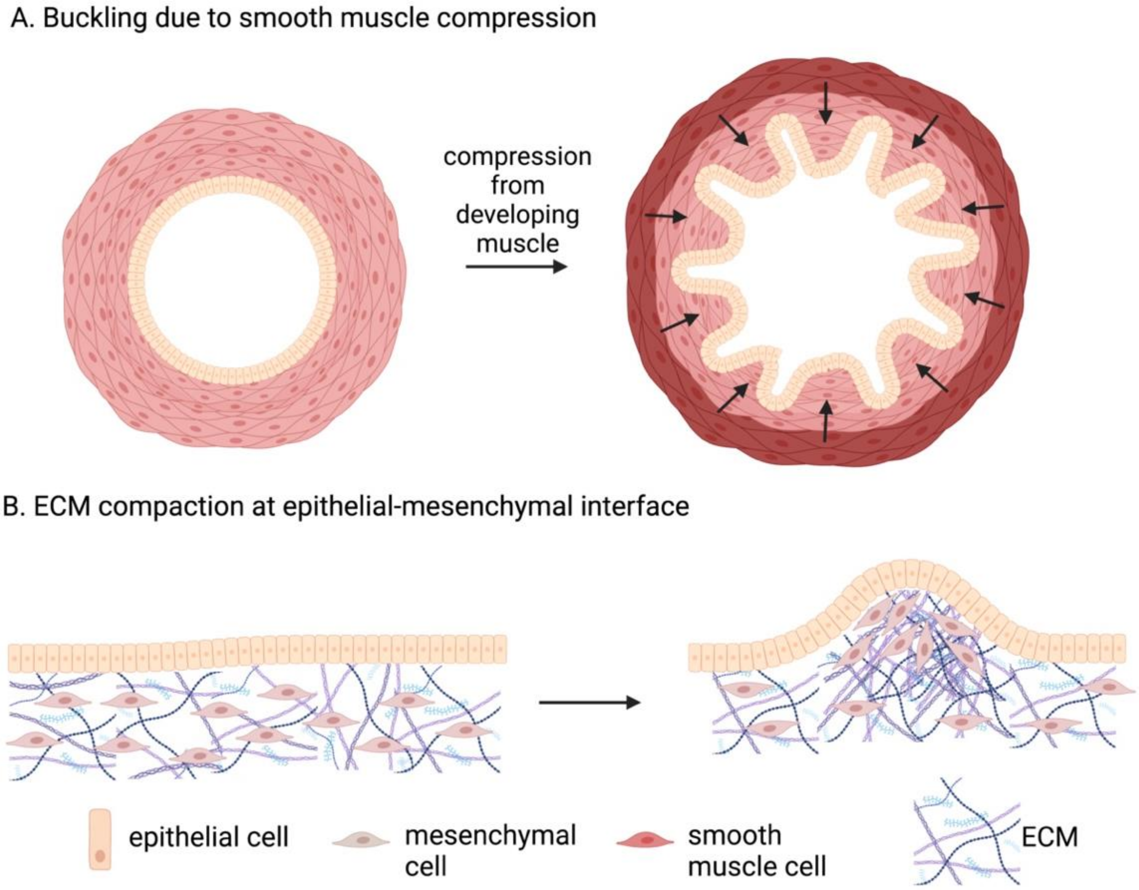

Figure 1.2: Diagrammatic representation of epithelial folding mediated by compression from surrounding cell layers. (A) Smooth muscle compression. In the developing chick gut, sequential differentiation of mesenchyme into smooth muscle layers around the epithelial layer facilitates fold formation. The compressive stress from constriction forces the epithelial layer to bend. (B) ECM compaction. Mesenchymal cells populate at the epithelial-mesenchymal interface leading to alignment of the ECM fibers. This generates a compressive force along the direction of ECM alignment causing the epithelium to evaginate away from the mesenchyme.

1.3.3 Recreating epithelial folds using tissue engineering approaches

Epithelial folding is a complex process requiring multiple biochemical and mechanical cues from multiple layers of cells and tissues. Understanding folding dynamics in vivo can aid in reproducing epithelial folds in vitro or in engineered tissue to better recapitulate the native structure.

Spatio-temporal activation of epithelial folding can be achieved using optogenetic tools. During Drosophila gastrulation, localized apical constriction and myosin accumulation can be induced using photoactivation of Rho1 at the apical surface with a 2-photon system (Izquierdo et al., 2018). The cryptochrome 2/cryptochrome-interacting basic helix-loop-helix 1 (CRY2/CIB1) protein heterodimerization system is employed to activate Rho1 using light. In addition to capturing endogenous tissue folding dynamics, epithelial folding can be induced without modifying the gene regulatory networks. Similarly, using OptoShroom3, an optogenetic tool, Shroom3 activation and deactivation in a layer of MDCK epithelial layer induces epithelial folding (Martínez-Ara et al., 2022). Hence optogenetics serves as an important tool to manipulate the 3D shape of tissues. Cell-ECM interactions can be used to generate 3D folded tissue in vitro using the traction forces generated by mesenchymal cells on ECM. Mesenchymal condensation aligns the ECM fibers along the path of tissue folding by contracting the ECM surface. When mesenchymal cells are deposited on free-floating ECM gels, the compressive forces arising from mesenchymal compaction cause folding along the direction of ECM fiber alignment (Hughes et al., 2018). Interestingly, when mesenchymal cells are deposited on either side of ECM gels in defined patterns, folding occurs along the direction of the predetermined patterns. Further, mesenchymal cells have a greater potential to contract

ECM gels compared to endothelial cells and epithelial cells. This suggests that structures that fold by mesenchymal compaction would have little to no directional cues from other cell types. Hence mesenchymal compaction is a great strategy that can be used to fold engineered epithelial tissue.

The mucosal layer of hollow tubular organs, such as the intestine and stomach, has folds to increase the surface area for nutrient absorption and luminal expansion during transport. In vivo, mucosal folding occurs due to compressive stress arising due to the differential growth of epithelium compared to surrounding mesenchyme and smooth muscle. Mucosal folding can be recapitulated in vitro using compressive strain and mechanical instability of pre-stretched hydrogels (Chan et al., 2018). Epithelial cells cultured on a hydrogel are placed on another pre-stretched tough hydrogel following which the pre-stretched hydrogel is relaxed. The resulting compressive strain on the hydrogel-carrying epithelial cells causes folding along various patterns depending on the pre-stretch conditions and elasticity of the hydrogel.

1.4 Conclusion

Epithelial folds play an important role in shaping body and organ structure during development and morphogenesis. Aberration in epithelial folds can lead to developmental defects and pathological conditions. Uterine epithelial folds have been observed and described in several species including humans. However, the mechanisms governing their formation and function remain largely unknown due to lack of significant studies and technological limitations. Hence, the information on epithelial folds from studies in other organ systems along with recent developments in new tools and techniques can be leveraged to study uterine folds. Advancements in understanding uterine folding can impact the field of women’s reproductive health by providing new ways of diagnosis and treatment of infertility and pathological conditions.

Chapter 2: Materials and Methods

Animals: CD1 mice and *Wnt5a*$^{\text{loxP/loxP}}$ (Stock No. 026626) (Ryu et al., 2013) mice were purchased from Charles River Laboratories and Jackson Labs respectively. *Rbpj*^{cKO} *(Pgr*^{Cre} *Rbpj*$^{loxP/loxP}$) mice were generated as described previously (Strug et al., 2018) using the *Pgr*^{Cre} mice (Soyal et al., 2005). *Wnt5a*^{cKO} mice were generated by mating *Pgr*^{Cre} mice with *Wnt5a*$^{loxP/loxP}$ mice. For pregnancy studies, adult females aged 6 to 8 weeks were mated with fertile males and appearance of vaginal plug was identified as gestational day (GD) 0.5. For time course analysis, CD1 females were dissected between GD2 1200 h and GD4 1200 h. *Wnt5a*^{cKO} and *Rbpj*^{cKO} mice were dissected at GD3 1200 h, GD4 1200 h and/or 1800 h, and GD5 1200 h. All mouse studies were approved by the Michigan State University Institutional Animal Care and Use Committee.

Hormone and Inhibitor treatments: 17β-Estradiol (E8875, Sigma-Aldrich) and Progesterone (P0130, Sigma-Aldrich) were dissolved in sesame oil (Acros Organics, AC241002500). For E2 treatment, C57BL/6 mice were injected subcutaneously with 200ng of 17β-Estradiol on GD0 1200 h or GD1 1200h. For P4 treatment, C57BL/6 mice or CD1 mice were injected subcutaneously with one dose of 4mg Progesterone on GD2 1800 h or with three doses of 4mg Progesterone on GD0, GD1 and GD2 at 1200 h. Vehicle control groups were treated with sesame oil only. RU486 (Mifepristone, M8046, Sigma-Aldrich) was dissolved in 5% DMSO in sesame oil. C57BL/6 or CD1 mice were treated with one dose of 8mg/kg RU486 on GD2 1800 h. Vehicle control mice were treated with 5% DMSO in sesame oil. Mice from all treatment groups were dissected at GD3 1200 h.

Hyperstimulation: Hyperstimulation was induced by injecting C57BL/6 mice with 5IU Pregnant Mare Serum Gonadotropin (PMSG) and 48 hours later with 5IU Human Chorionic Gonadotropin (hCG). Following hCG treatment, the female mice were set up for mating with fertile males. Appearance of vaginal plug the next morning confirmed mating (GD0) and the mice were considered to be pregnant. Control C57BL/6 mice did not receive any treatment and were set up for mating to induce pregnancy. Both hyperstimulated and control mice were dissected at GD0 1200 h, GD1 1200 h, GD3 1200 h, GD4 1800 h and GD13 1200 h.

Whole-mount immunofluorescence: Whole-mount immunofluorescence was performed as previously described (Arora et al., 2016). Uteri were dissected from mice and fixed in DMSO:Methanol (1:4). For immunostaining, uteri were rehydrated in Methanol:PBT (1% Triton X-100 in PBS) (1:1) for 15 min, washed in PBT for 15 min and incubated in blocking solution (2% powdered milk in PBT) for 2 hours, at room temperature. Uteri were incubated with 1:500 concentration of primary antibodies diluted in blocking solution for 5 to 7 nights at 4°C following which they were washed with 1% PBT 4 to 6 times for 30 min each at room temperature. Uteri were then incubated with secondary antibodies at 4°C for 2 to 3 nights, followed by 4 to 6 washes of 30 min each with 1% PBT and dehydration in methanol for 30 min. Uteri were then bleached in a solution of 3% H_2O_2 prepared in methanol overnight at 4°C. Finally, the samples were washed in 100% methanol for 30 min and cleared in BABB (1:2, benzyl alcohol:benzyl benzoate) (Sigma-Aldrich, 108006, B6630). Primary antibodies used include CDH1 (M108, Takara Biosciences), FOXA2 (Abcam, ab108422), PTGS2 (Abcam, ab16701). Alexa Flour conjugated Secondary antibodies, Donkey anti-Rabbit 555 (A31572) and

Goat anti-Rat 647 (A21247) were obtained from Invitrogen, and Hoechst (Sigma Aldrich, B2261) was used to stain the nucleus.

Cryosection immunofluorescence staining: Following dissection, uterine tissue samples were fixed in 4% PFA overnight at 4C. Samples were then washed in PBS for 5min at room temperature following which they were serially placed in 10%, 20% and 30% sucrose solutions at 4 ^{o}C. The samples were then placed in cryomolds, embedded in OCT solution and frozen at -80 ^{o}C. The frozen blocks were sectioned using a cryostat at 7μm thickness and fixed to glass slides.

Slides were thawed at room temperature following which the tissue sections were surrounded with a hydrophobic barrier. Sections were washed in PBS for 5 min and incubated in in blocking solution (0.1% powdered milk in PBT) for 30 min at room temperature. Sections were then incubated in primary antibodies diluted in blocking solution overnight at 4 ^{o}C followed by secondary antibodies diluted in PBT for 1 hour at room temperature. Sections were covered with mounting solution and imaged using a confocal microscope.

RNAScope In Situ Hybridization (RNAscope ISH)

ISH was performed as per the ACD Bio RNAScope 2.5 HD Detection Kit – RED (Cat. No. 322360) instructions. Briefly, cryosection slides were taken from -80 ^{o}C and thawed at room temperature for 15 min. Slides were washed with 1XPBS and baked baked in an oven at 60^{o}C for 45-60 mins. The slides were then post-fixed in 4% PFA for 5 mins and following which they were serially immersed in 50%, 70% and 100% ethanol for 5 min each at room temperature. The slides were then covered with 2-4 drops of hydrogen peroxide for 10 mins after which they were then placed in slide holders containing 1X

Target Retrieval solution and boiled for 5 min at 100°C. The sections were surrounded with a hydrophobic barrier and incubated with Protease III for 30 min at 40°C. The sections were then incubated with Wnt5a probe for 2 hr at 40°C following which they were sequentially incubated with AMP 1-6 at 40C for 15-30 min. The sections were covered with Fast RED-B – Fast RED-A (1:60) for 10 min at room temperature. Finally, the sections were incubated with Hoechst (1:500 dilution) for counter-staining and baked at 60°C for 10-15 min. The slides were covered with a Prolong Gold before imaging.

Confocal microscopy: For whole tissue imaging, samples were imaged using Leica TCS SP8 X Confocal Laser Scanning Microscope System with white-light laser and 10X air objective. The entire length and thickness of the uterine horn was imaged using the tile scan function with z stacks 5-7μm apart. Images were merged using Leica software LASX version 3.5.5.

For tissue section imaging, slides were imaged using Leica TCS SP8 X Confocal Laser Scanning Microscope System with white-light laser and 20X water immersion objective or 63X oil immersion objective.

3D reconstruction and image analysis: Image analysis was performed using commercial software Imaris v9.2.1 (Bitplane). The confocal image (.LIF) files were imported into the Surpass mode of Imaris. Using the channel arithmetics function the FOXA2 signal of glands was subtracted from the epithelial CDH1 signal to get the lumen-only signal. The Surface module of Imaris was then used to reconstruct the 3D surface of the lumen from the lumen-only channel. Similarly, for gland surfaces, the Surface module was used to reconstruct the 3D surfaces from the FOXA2 channel. Embryo surfaces were reconstructed using the Manual mode of the Surface module from the Hoechst signal.

Quantification of luminal folding angle, distance between folds, distance of embryo from the middle of PIR, embryo-uterine orientation, and space between embryo and the decidua was performed using the Measurement Points module in Imaris. For more details see supplementary methods.

Statistics: Statistical analysis was performed using GraphPad Prism and Microsoft Excel. Student's unpaired t test or Mann-Whitney U test was used to compare two groups. One-way ANOVA or Kruskal Wallis test was used to compare three or more groups. Dunn's multiple comparison test was used along with Kruskal Wallis test when necessary. P values were adjusted for multiple comparisons. Pearson's correlation coefficient was used to test the correlation between angle of embryo alignment with uterine axis and ratio of space between embryo and decidua. $P<0.05$ was considered statistically significant.

Quantification of luminal folding angle: Each uterine horn was divided into 3 equal regions and a lumen surface of approximately 1000μm in length was reconstructed in each region. A MATLAB script for surface curvature (as previously described, (Arora et al., 2016)) was run on the lumen surfaces to determine the regions that are highly folded. A value of $C_{mean}>0.15$ was used as a threshold to define a uterine fold. Images of the 3D surfaces with curvature analysis, oriented along the M-AM axis, were captured using the snapshots module. The 2D images were reimported into Imaris and visualized using the XY plane. Two orthogonal planes (XZ and YZ) were placed to define the M-AM and the anterior-posterior (A-P) axes respectively. The intersection of the M-AM and A-P planes was placed on the end of a fold. Using the Measurement Points module, the first point was placed at one end of the fold, followed by the second point at the other end of the fold where it meets the intersection of the M-AM and A-P planes, and finally the third point at the intersection of the M-AM plane and the plane of the 2D image (Fig. S1). The value of the angle was obtained using the statistics function and this angle was called the fold angle.

Quantification of distance between folds and gland numbers: The folds were visualized using an optical slicer using CDH1 or using a 3D Surface. A measurement point was placed on the surface of one fold and a second Measurement Point was placed on the adjacent fold. The distance between the points was obtained using the statistics function. All distances were normalized to the length of the uterine horn. To determine the number of glands between two folds, 3D surfaces of glands were reconstructed using the Surface module. The statistics function was applied on the gland surfaces to obtain the absolute number of glands. The number of glands between two folds per unit length was obtained by normalizing to the distance between the folds in the region of interest.

Quantification of distance of embryo from middle of PIR: The PIRs, folds and embryos were visualized using an optical slicer using CDH1, FOXA2 and Hoechst. The region between the first complete transverse fold running from M to AM pole at the anterior end of the PIR and the next complete transverse fold at the posterior end of the PIR was considered as the boundary of the PIR (Fig.3.5). Partially resolved folds in the PIR that do not run all the way from the M pole to AM pole were not considered as a complete transverse fold. Using the Measurement Points module in Imaris, the first point (A) was placed on the base of a transverse fold on the anterior end of a PIR and second point (B) was placed on the base of the next transverse fold on the posterior end of the PIR. A third point (C) was placed on the embryo at the PIR or nearest to the PIR. Using the statistics function of Imaris, the Cartesian coordinates of the three points were obtained and imported into Excel. The distance of C from the midpoint of line A-B was calculated to obtain the distance of embryo from the center of the PIR. The distances were normalized by dividing with the length of A-B.

Quantification of embryo-uterine orientation: The embryo at an implantation site on GD4 1800 h was visualized using an optical XY Orthogonal Slicer or Oblique Slicer (Fig. S10). An XZ Orthogonal Slicer was used to define the M-AM axis and was placed at the abembryonic pole of the embryo. Using the Measurement Points module, the first point was placed on the ICM on the M-AM plane. The second point was placed on the intersection of the M-AM plane and the abembryonic pole on the XY plane. The third point was placed on the intersection of the M-AM and XY planes. The value of the angle was obtained using the statistics function of Imaris.

Quantification of space between epiblast and maternal decidua: The embryo in a decidua was visualized along the dorsal-ventral plane using an XY Orthogonal Slicer or an Oblique Slicer. A YZ slicer indicating the A-P axis was placed on the embryo perpendicular to the M-AM plane. Using the Measurement Points module, the first length (x) on the anterior end of the embryo was measured by placing one point on intersection of the YZ plane and the maternal decidua, and the other point on the intersection of the epiblast and the YZ plane. Similarly, the second length (y) on the posterior end of the embryo was measured. The ratio of the lengths, z = maximum(x,y)/minimum(x,y).

Quantification of angle between embryonic-abembryonic axis and embryonic-PTGS2 axis: The surface module in Imaris was used to make a surface of the PTGS2 expression pattern around the implantation chamber and the center point (a) of the PTGS2 surface was obtained. The embryo at an implantation site was visualized using an optical XY Orthogonal Slicer or Oblique Slicer. Using the Measurement Points module, the first point was placed on point a. The second point was placed on the ICM (embryonic pole) (point b) and the third point was placed on the abembryonic pole (point c). The value of the angle between line ab and bc was obtained using the statistics function of Imaris.

Chapter 3: Uterine folding dynamics around implantation and its relationship to embryo location

3.1 Introduction

During early pregnancy, the uterus in mammals undergoes dynamic remodeling, guided by cellular and molecular events, to prepare for embryo implantation (Arora et al., 2016; Yuan et al., 2018). Changes in luminal epithelium (LE) morphology during pregnancy are critical for embryo implantation and pregnancy outcomes (Cha et al., 2014; Daikoku et al., 2011; Tu et al., 2016; Zhang et al., 2014). In several mammals, including monotocous species such as humans, horses, and cows and polytocous species such as mice, rats, pigs and rabbits, the LE undergoes architectural changes to form structures called uterine folds (hereafter referred to as 'luminal folds') (Abd-Elkareem, 2017; Arora et al., 2016; Enders, 1975; Fissore et al., 1986; Jokubkiene et al., 2015). In mice, based on 2D histological sections, luminal folds are also referred to as crypts or regularly spaced luminal epithelial evaginations that extend from the primary lumen towards the anti-mesometrial (AM) pole on gestational day (GD) 3 of pregnancy (Cha et al., 2014; Daikoku et al., 2011). More recently, using confocal imaging and 3D reconstruction of the mouse uterus, we showed that 2D crypts coincide with 3D luminal folds, suggesting that they are the same structure (Arora et al., 2016). The 3D luminal folding pattern changes significantly from a non-pregnant state to pregnant state, with folds running along the mesometrial-antimesometrial (M-AM) axis of the mouse uterus on GD3 (Arora et al., 2016). In humans, the earliest evidence of uterine (endometrial) folds dates back to 1973, when longitudinal folds were discovered in the uterine cavity using hysterography in both the proliferative and secretory phase of the menstrual cycle (Slezak and Tillinger, 1973).

In 1994, Goldstein discovered folds in the endometrium using ultrasonohysterography, and called them ‘endometrial moguls’ (Goldstein, 1994). Recently, using saline contrast sonohysterography ~50% women displayed endometrial folds in the secretory phase irrespective of uterine pathology (Jokubkiene et al., 2015). Due to limitations of current technologies and ethical concerns associated with research in pregnant women, how endometrial folds form during the window of implantation, and their function in pregnancy remains unknown.

A second structure formed by the LE in conjunction with the embryo is the implantation chamber (hereafter referred to as ‘chamber’). In several species including mice, rats, dogs and horses, the LE forms a chamber that holds the implanting embryo (Barrau et al., 1975; Enders and Liu, 1991; Enders, 1975). The structure of the chamber was first described in rats as a parabolic depression of the LE at the site of implantation (Enders, 1975). In mice, this chamber is a V-shaped structure containing the embryo (Arora et al., 2016; Enders, 1975; Yuan et al., 2018). Although, the terms ‘uterine crypts’ and ‘implantation chambers’ are often used interchangeably (Cha et al., 2014; Yuan et al., 2016; Yuan et al., 2018), there is lack of a clear distinction between a crypt (fold) and a chamber. Thus, structurally whether folds during pre-implantation transform into chambers post implantation is not known.

Recently, using embryo location analysis, we showed that embryo movement in the mouse uterus along the ovary-cervix (O-Cx) axis has three distinct phases: embryo entry (GD3 0000 h onwards); unidirectional clustered phase (GD3 0600 h onwards); and bidirectional spacing or scattering phase (GD3 1200 h onwards) (Flores et al., 2020). How the luminal folding pattern changes with embryo location is not known. We also showed that the number of implantation sites in the mouse uterus is not predetermined but rather depends on the number of embryos in the uterus and embryos implant at equidistant positions along the O-Cx axis (Flores et al., 2020). Whether potential implantation sites are established prior to or after the arrival of the embryo at the implantation site and whether the structure of the uterine lumen helps in equal spacing of implantation sites is not known.

Using a detailed time course of folding in the mouse uterus, we show how dynamic changes in uterine luminal folding pattern facilitate implantation region formation, and chamber formation. Furthermore, we clarify the relationship between pre-implantation folds and post-implantation chambers.

3.2 Results

3.2.1 Uterine luminal folding dynamically changes along with uterine embryo location

To understand the relationship between luminal folding and embryo location, we evaluated uterine structure during GD2 1200 h - GD4 1200 h (Fig. 3.1A-G) and quantified the angle of the luminal fold with the uterine M-AM axis (Fig. 3.2). On GD2 1200 h, when the embryos are in the oviduct (Flores et al., 2020), the luminal folds are present along both the M-AM axis (*transverse folds*) and O-Cx axis (*longitudinal folds*) (median=61.4°) (Fig. 3.1A,H). At GD3 0000 h, when clusters of embryos are present near the oviductal-uterine junction (Flores et al., 2020), the luminal folding pattern changes significantly and majority of folds are longitudinal (median=79.25°, $P<0.0001$, GD2 1200 h vs GD3 0000 h) (Figs 3.1B,H, 3.3A). During clustered embryo movement, GD3 0600 h (Flores et al., 2020), majority of the folds continue to be longitudinal, and embryos can be found in these folds (median=77.65°, P=0.96, GD3 0000 h vs GD4 0600 h) (Fig. 3.1C,H). Strikingly, at GD3 1200 h, prior to bidirectional scattering of embryos, the entire length of the lumen has only transverse folds along the M-AM axis (median=15.1°, P<0.0001, GD3 0600 h vs GD3 1200 h) (Fig. 3.1D,H). Notably, only ~35% of embryos (11/31 embryos, n=4 mice) are found in these transverse folds, while the remaining ~65% embryos are present in flat regions present in between two folds (Fig. 3.3 B). At GD3 1800 h, post embryo scattering, long stretches of flat luminal regions called *peri-implantation regions* (PIRs) begin to form. The regions between two PIRs called *inter-implantation regions* (IIRs) retain the transverse folds (median=26.1°) (Fig. 3.1E,H). At GD4 0000 h, at the initiation of embryo implantation, the embryos are now present within the flat PIRs at the presumptive implantation sites (Figs 3.1F, 3.3C and 3.4). At GD4 1200 h, post embryo attachment, a 'V' shaped chamber forms at the implantation site in the middle of the PIR (Fig. 3.1G). Markedly, at this time, the folds in the IIRs, continue to be aligned along the M-AM axis (median=23.1°) and there is no significant difference compared to GD4 0000 h (P>0.99) (Fig. 3.1H).

3.2.2 Peri-implantation region is formed by resolution of transverse folds and stretching of lumen along the O-Cx axis

To discern the relationship between folds at GD3 and GD4, we first evaluated the distance between two consecutive transverse folds along the M-AM axis in three groups: GD3 1200 h (GD3), GD4 0000 h IIRs (GD4 IIRs) and GD4 0000 h PIRs (GD4 PIRs) (Figs 3.5A,B and 3.6). The distances are normalized to the length of the uterine horn to account for the variation amongst mice and are represented as normalized units (nu). We found a significant difference between the three groups (P<0.001, Kruskal-Wallis test, Dunn's multiple comparison). The mean distance between two folds at GD4 PIRs (mean=0.079nu) is significantly higher compared to both GD3 (mean=0.026nu, P=0.03) and GD4 IIRs (mean=0.017nu, P<0.001) (Fig. 3.5C). We also observe that the mean distance between folds at GD4 IIRs is significantly lower than GD3 (P<0.001). Since there is no epithelial proliferation beyond GD3 (Haraguchi et al., 2014; Hiraoka et al., 2020), increased length of the PIR at GD4 could be due to a stretching mechanism or resolution (flattening) of transverse folds formed at GD3. To distinguish between these two possibilities, we quantified the number of glands between two folds in the three groups. We predicted that if the primary mechanism of PIR formation is resolution of folds, then the number of glands between two folds at GD4 PIRs should be higher than the number of glands between two folds at GD4 IIRs and two folds at GD3. Indeed, the average number of glands between two folds at GD4 PIRs (mean=48.6 glands) is ~2 fold compared to both GD3 (mean=22 glands, P<0.001) and GD4 IIRs (mean=19.5 glands, P<0.001) (Fig. 3.5D). In addition, there is no significant difference between the total number of glands per unit length of horn on GD3 1200 h and GD4 0000h (PIRs and IIRs combined) (P=0.38, Mann-Whitney U test) (Fig. 3.7). Taken together, these data support resolution of folds to form PIRs. Further, when normalized for horn length, we observed that the average number of glands per millimeter (mm) of horn length at GD4 PIRs (mean=16.8 glands/mm) is lower compared to both GD3 (mean=21.74 glands/mm, P<0.001) and GD4 IIRs (mean=27.45 glands/mm, P=0.03) (P<0.001, Kruskal-Wallis test, Dunn’s multiple comparison) (Fig. 3.5E). The decrease in the number of glands per mm at PIRs can be due to some stretching of the lumen to resolve folds or due to the added length from the resolved folds. However, we also observed an increase in the average number of glands per mm at GD4 IIRs compared to GD3 (P=0.04), although the number of glands between two consecutive folds in these two groups is the same (Fig. 3.5E). These data suggest that the lumen in the IIRs is likely compressed which would support a stretching mechanism for the lumen to form PIRs. Overall, our results suggest that PIRs primarily form as a result of resolution of transverse folds, however, lumen stretching along the O-Cx axis also contributes to PIR formation.

3.2.3 Luminal patterning to form flat peri-implantation regions precedes fine embryo spacing

Whether the resolution of transverse folds to form PIRs occurs prior to or after the arrival of the embryo at the implantation site is not known. At GD3 1800 h, when PIRs are first observed, embryos are commonly present at the margins of the flat PIRs, closer to the IIR fold on either end (Fig. 3.8A). Post-implantation, the embryo is always present closer to the middle of the PIR (Fig. 3.8B). We quantified this by measuring the distance of an embryo from the middle of the PIR on GD3 1800 h and post-implantation between GD4 1200 h - 1800 h. The distances are normalized to the length of the PIR. We observe that the mean distance of the embryos from the middle of the PIRs on GD3 1800 h (mean=0.23nu) is significantly higher than the post implantation time points (mean=0.05nu) ($P<0.001$, Mann-Whitney U test) (Fig. 3.8C).

Previously we have shown that the glands in the inter-implantation region reorient towards the implantation site on GD4 1200 h (Arora et al., 2016). The site of embryo implantation always coincides with the center of the gland reorientation site. Here, we show additional evidence that gland orientation occurs as early as GD3 1800 h when PIRs are first observed (Fig. 3.9A,A’). Interestingly, the center of gland reorientation site coincides with the center of PIRs at GD3 1800 h (Fig. 3.9A,A'). However, the embryos on GD3 1800 h are away from the gland reorientation sites, whereas at GD4 1200 h, implantation sites and the center of gland reorientation site and PIR coincides (Fig. 3.9 B,B'). Hence, glands reorient towards the center of the PIRs even before embryos arrive at the potential implantation site. These data support that the PIR and gland reoriented sites are formed prior to embryo arrival at the implantation site.

3.3 Discussion

3.3.1 Uterine folds: Differences and similarities between mice and other species

Knowledge pertaining to size and orientation of folds with respect to the uterine axis varies depending on the species and stage of estrous cycle and is heavily dependent on the plane of examination (Abd-Elkareem, 2017; Enders and Liu, 1991; Fissore et al., 1986; Kähn et al., 1989; Slezak and Tillinger, 1973). This is because longitudinal folds can only be visualized when the tissue is sliced along a transverse plane and transverse folds can only be visualized when the tissue is examined along the longitudinal plane. Most of the conventional visualization methods such as ultrasound and histology are performed in the transverse plane and can easily detect longitudinal folds but often miss the transverse folds. Consequently, longitudinal folds along the long axis of the uterus have been observed in multiple species including the human, rabbit, horse, donkey and bushbaby uterus (Ginther, 1983; Njogu et al., 2013; Renner-Martin et al., 2009). In humans, longitudinal folds have been observed during both the secretory and proliferative phases of the menstrual cycle but the orientation of folds during pregnancy is not known and requires future investigation (Jokubkiene et al., 2015; Slezak and Tillinger, 1973).

Ultrasound examination of the bovine uterus in the transverse plane, revealed distinct longitudinal folds at the time of estrous, and these folds disappear at the time of diestrus or pregnancy (Fissore et al., 1986). However, in a different study, 3D examination using nuclear magnetic resonance imaging in the pregnant bovine uterus revealed crescent-shaped transverse folds that are perpendicular to the long axis of the uterine horn (Kähn et al., 1989). Thus, it is important to assess folding in different planes to fully understand the structural changes associated with the uterine lumen in preparation for pregnancy. In our study using mice, we observed both longitudinal folds (along O-Cx axis) and transverse folds (along M-AM axis) prior to embryo entry into the uterus and only transverse folds during pre-implantation phase of pregnancy. Our observations during mouse pregnancy are similar to those made in the bovine where longitudinal folds disappear while transverse folds remain during pregnancy. In rabbits, six longitudinal folds are observed after induction of ovulation during pseudopregnancy, and the complexity of the folding pattern changes with the stage of pseudopregnancy (Abd-Elkareem, 2017). We observe a similar change in the complexity of folding pattern in the mouse uterus, depending on the timing of pregnancy and embryo location.

3.3.2 Peri-implantation region formation predefines implantation sites

In this study, we provide novel evidence that the implantation regions are formed by luminal patterning, post uterine sensing of embryos but prior to embryo spacing and arrival of embryos at implantation sites. Since the embryo always attaches at the center of the flat PIR, in future, it will be important to identify chemotactic proteins that are specifically expressed in the central region of the flat PIR that attract the embryo to the potential implantation site.

While it is well known that implantation in mice occurs at the AM-pole, in women implantation preferentially occurs in the fundus region of the uterus, near the posterior wall (Kim and Kim, 2017). PIR formation prior to embryo arrival at implantation site, could be key to successful implantation even in monotocous species, independent of embryo spacing. Such knowledge can be useful in enhancing assisted reproductive technologies where the optimal stage and timing for embryo transfer during the window of implantation is still not understood (Enciso et al., 2021; Mackens et al., 2017).

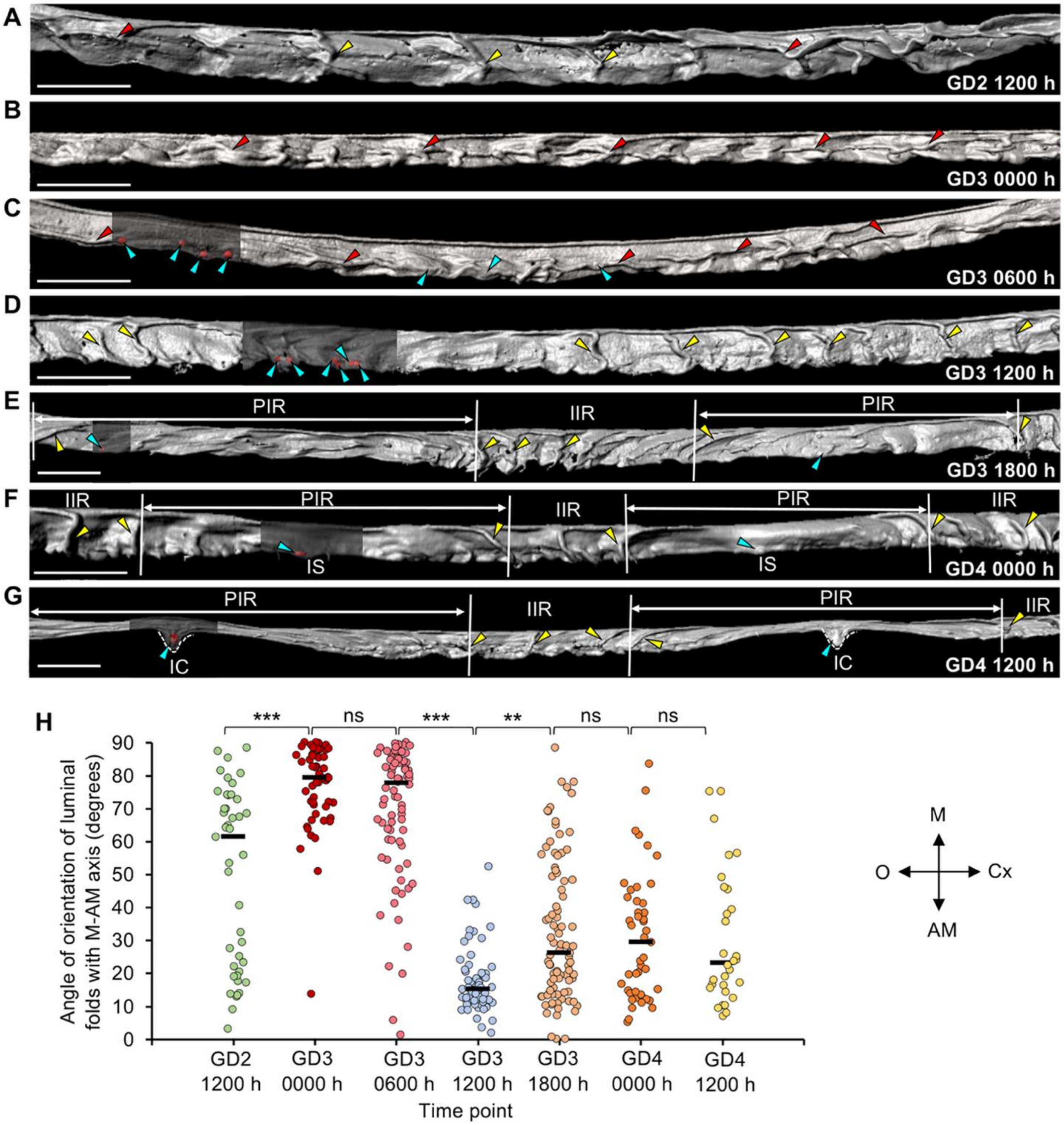

Figure 3.1: Time course of luminal folding pattern from GD2 to GD4.
(A-G) 3D reconstruction of uterine lumen (gray) on (A) GD2 1200 h, (B) GD3 0000 h, (C) GD3 0600 h, (D) GD3 1200 h, (E) GD3 1800 h, (F) GD4 0000 h and (G) GD4 1200 h. Longitudinal folds disappear and the entire lumen has transverse folds along the M-AM axis at GD3 1200 h. Segments of lumen surfaces in C-G are made transparent to show embryos (red surfaces, blue arrowheads). Yellow arrowheads, transverse folds; red arrowheads, longitudinal folds.

Figure 3.1 (cont’d)

White dotted lines indicate implantation chamber. PIR, peri-implantation region; IIR, inter-implantation region; IC, implantation chamber; IS, implantation site; M, mesometrial pole; AM, anti-mesometrial pole; O, ovary; Cx, cervix. Scale bars: 1000 µm. (H) Quantification of fold orientation with respect to the M-AM axis in A-G. Black lines indicate the median angle. n=3 or 4 mice per time point. ($P<0.001$, Kruskal–Wallis test, Dunn's multiple comparison). **$P<0.01$, ***$P<0.001$; ns, non-significant.

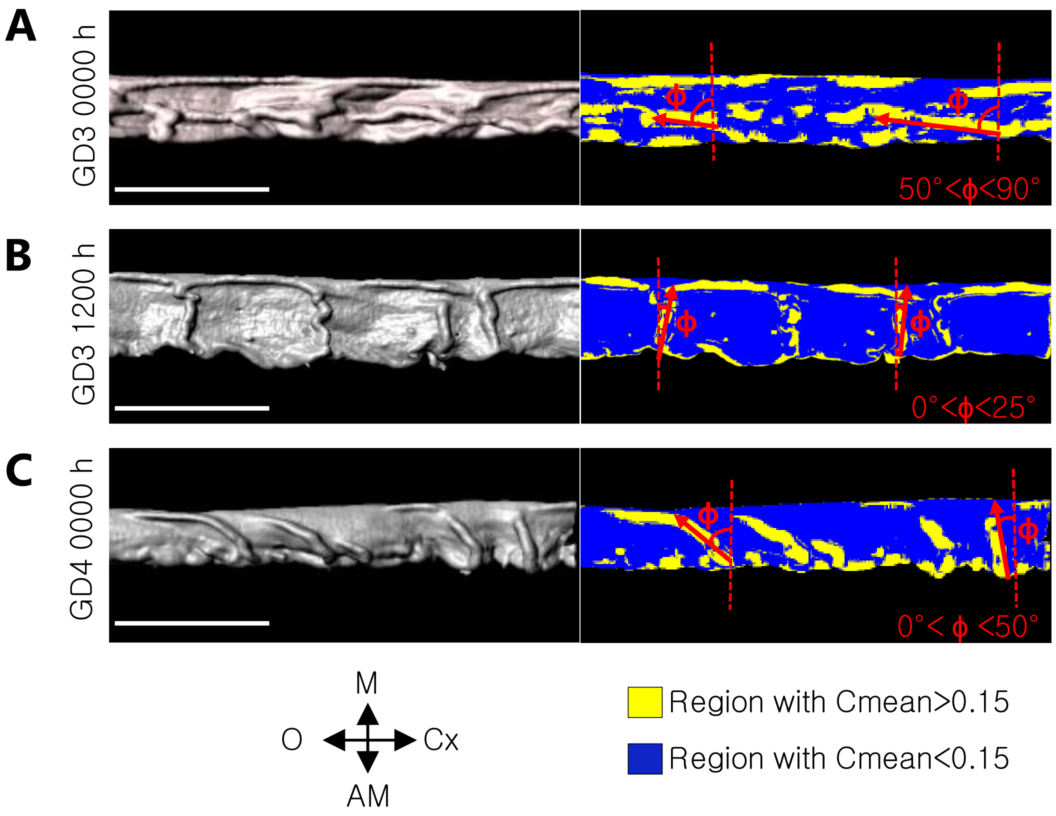

Figure 3.2: Quantification of luminal fold angle with respect to M-AM axis.
3D surface view and corresponding view with surface curvature analysis on GD3 0000 h (A), GD3 1200 h (B) and GD4 0000 h (C). Yellow arrows: transverse folds. Red arrows: longitudinal folds. Cmean – Curvature mean. ϕ - angle made by fold with respect to M-AM axis. (Scale bars: 1000μm).

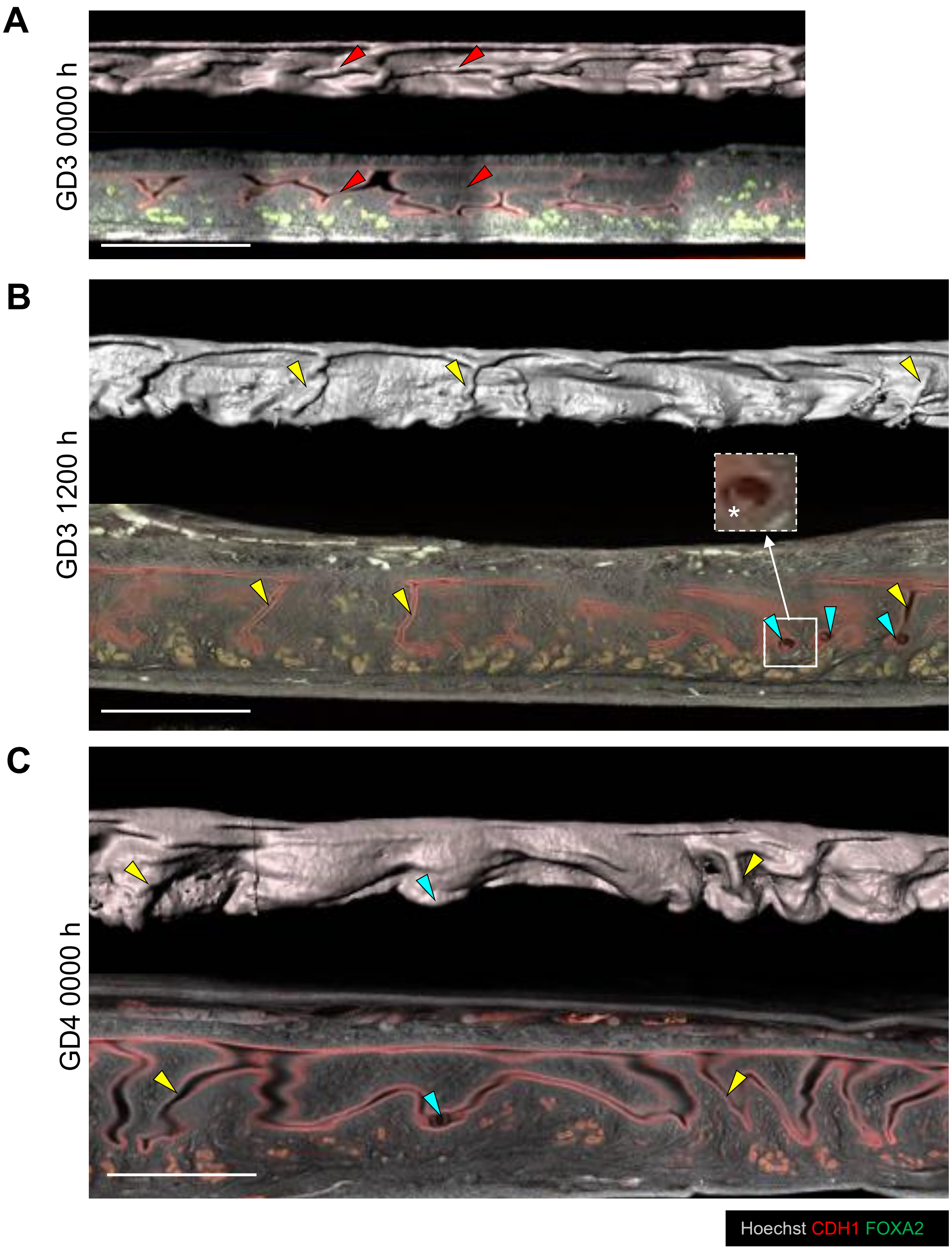

Figure 3.3: 3D uterine folds (2D crypts) do not transform into implantation chambers.

3D surface view and corresponding optical slice view of uterine lumen on GD3 0000 h (A), GD3 1200 h (B) and GD4 0000 h (C). Yellow arrows: transverse folds. Red arrows: longitudinal folds. Blue arrows: embryos. Asterisk: inner cell mass. Dotted square shows optical slice view of intact embryo in the lumen. (Scale bars: 1000μm).

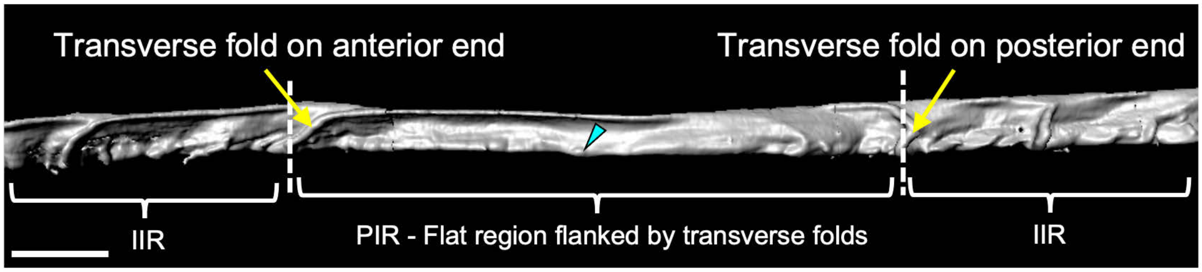

Figure 3.4: Peri-implantation region boundary estimation.
3D surface view of lumen containing PIR on GD4 0000 h. Yellow arrows: transverse folds. PIR - peri-implantation region; IIR - inter-implantation region. (Scale bars: 500µm).

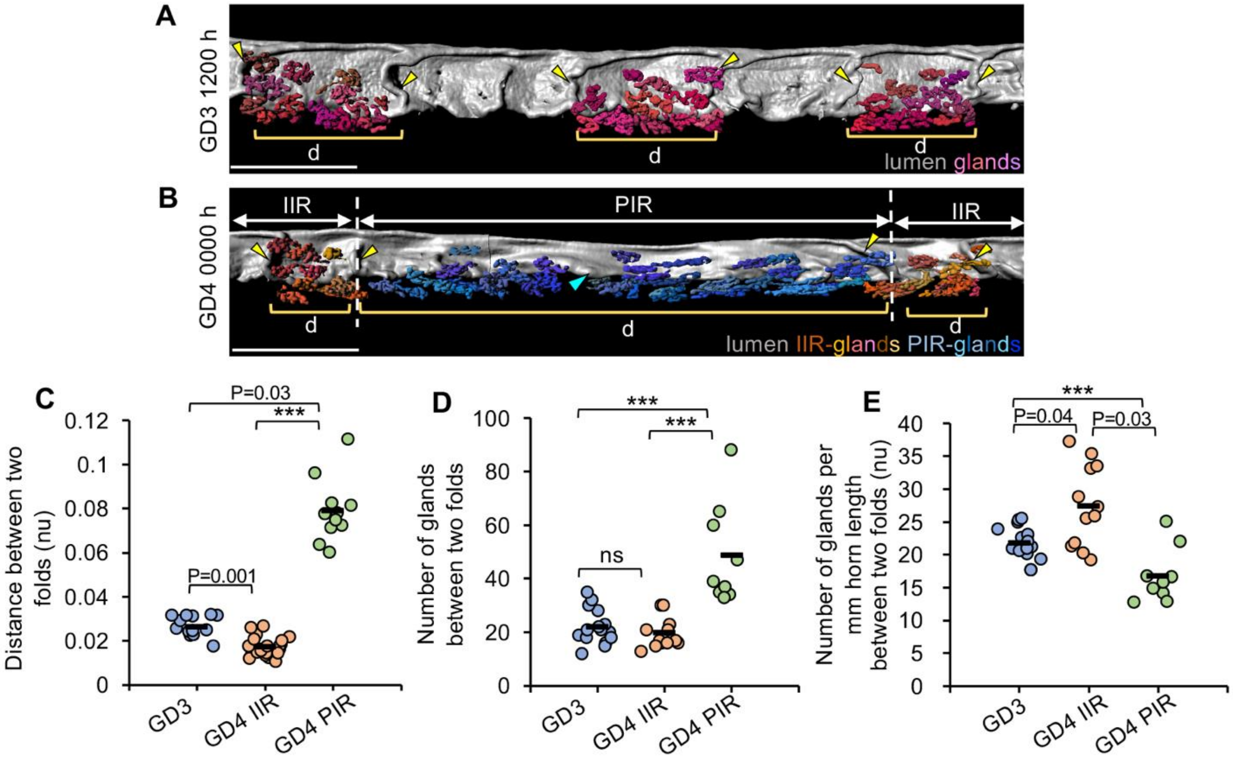

Figure 3.5: Transverse folds along the M-AM axis resolve to form peri-implantation regions.

(A,B) 3D surfaces of uterine lumen and glands at GD3 1200 h (A) and GD4 0000 h (B). In A, gland surfaces are displayed for alternate regions for easy visualization. PIR, peri-implantation region; IIR, inter-implantation region; d, region between two folds. Scale bars: 1000 µm. Yellow arrowheads indicate transverse folds; blue arrowheads indicate embryos; orange indicates pseudocolored glands in IIR; blue indicates pseudocolored glands in PIR. (C-E) At GD3 1200 h, GD4 0000 h IIRs and GD4 0000 h PIR, quantification of the distance between two consecutive transverse luminal folds (C), quantification of the number of glands between two luminal folds (D) and quantification of the number of glands between two folds per mm of PIR horn length (E). n=3 mice per group. (***P<0.001, Kruskal–Wallis test, Dunn's multiple comparison). nu, normalized units. Black horizontal lines indicate the mean value.

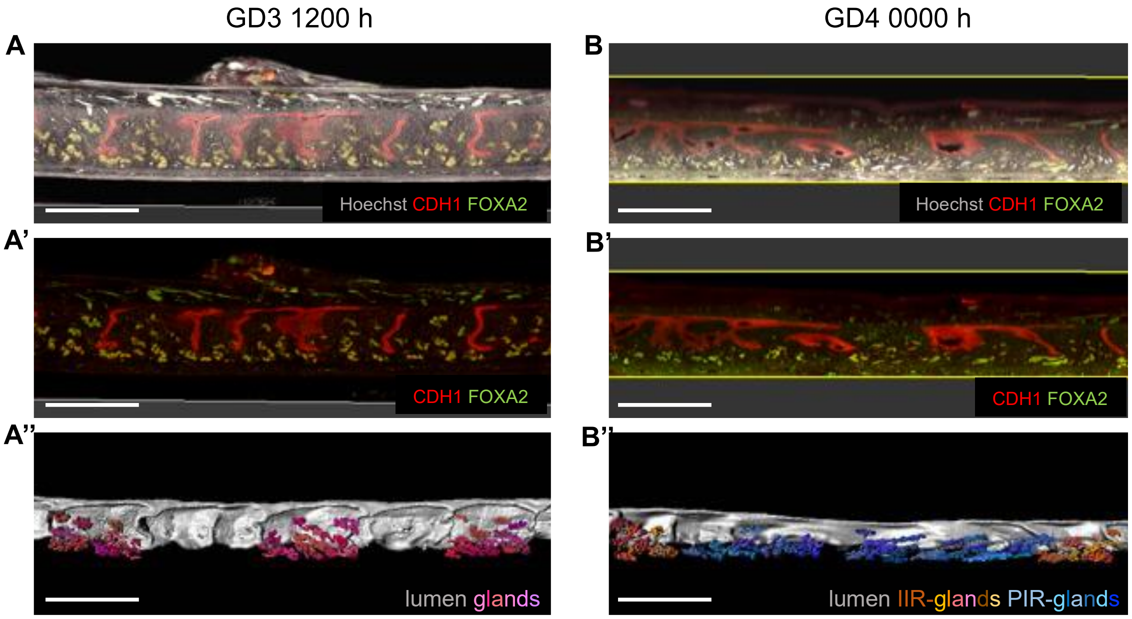

Figure 3.6: Optical slice view and corresponding 3D view of surfaces in Fig.2A-B. Optical slice view (A,A') and 3D surface view (A'') at GD3 1200 h. Optical slice view (B,B') and 3D surface view (B'') at GD4 0000h. Gland surfaces are pseudo-colored to distinguish glands in IIR (orange) and PIR (blue). (Scale bars: 1000μm).

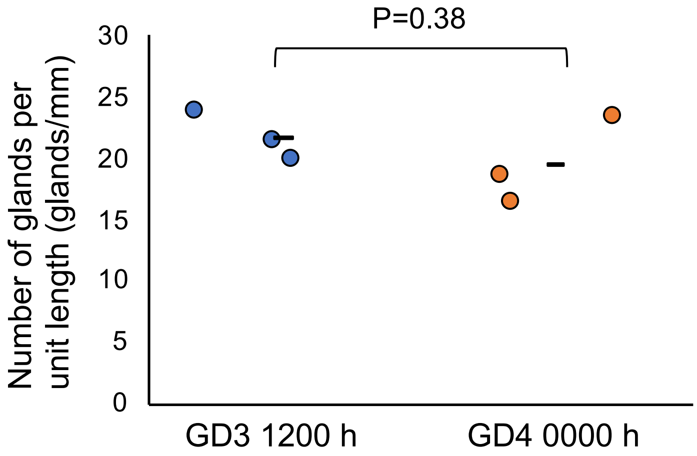

Figure 3.7: Number of glands remain unchanged between GD3 and GD4. Quantification of number of glands per mm of horn length at GD3 1200 h (n=3) and GD4 0000 h (n=3). (P=0.38, Mann-Whitney U test). n - number of mice.

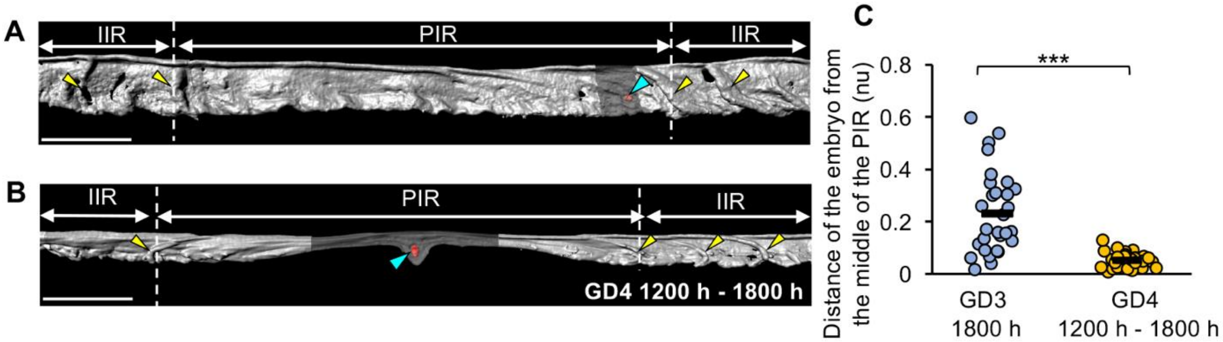

Figure 3.8: The peri-implantation region is formed prior to arrival of the embryo at the implantation site.

(A,B) 3D surface of uterine lumen and embryo at GD3 1800 h (A) and GD4 1200 h (B). Yellow arrowheads indicate transverse folds. Blue arrowheads indicate embryos (red surfaces). Scale bars: 1000 µm. At GD3 1800 h, the embryo is present near the PIR margin closer to the transverse folds in the IIR. At GD4, the embryo is present near the PIR center. (C) Quantification of the distance of embryos from the center of PIR at GD3 1800 h (n=7 mice, number of PIRs=29) and GD4 1200 h to 1800 h (n=6 mice, number of PIRs=29). Distances are normalized to PIR length. Black lines indicate the mean distance. ***P<0.001, Mann–Whitney U-test. PIR, peri-implantation region; IIR, inter-implantation region. nu, normalized units.

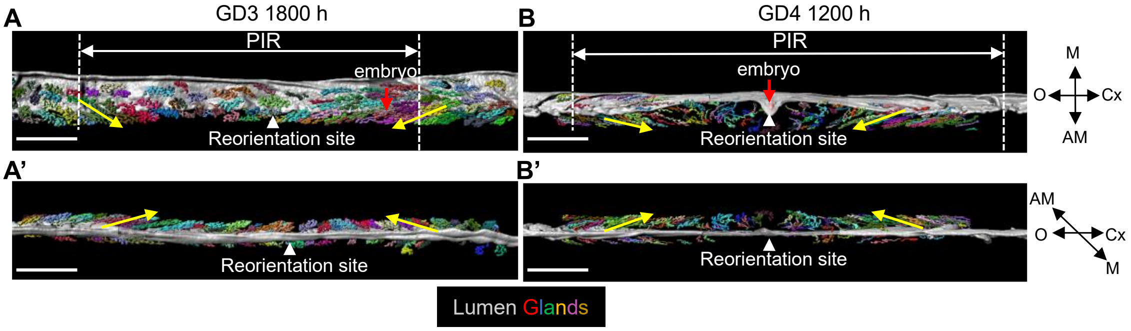

Figure 3.9: Gland Reorientation precedes embryo arrival at implantation site. 3D surface view of lumen (gray) and glands (rainbow) around peri-implantation regions on GD3 1800 h (A,A') and GD4 1200 h (B,B'). (A,B) View from ventral side; (A'B') View from mesometrial side. White arrowhead indicates gland reorientation site. Yellow arrow indicates direction of gland reorientation. Red arrow indicates location of embryo. PIR - peri-implantation region. (Scale bars: 1000μm).

Chapter 4: Effect of aberrant longitudinal folds on implantation and pregnancy outcomes using *Wnt5a*^{cKO} and *Rbpj*^{cKO} mouse models

4.1 Introduction

In mice, based on 2D histological sections, abnormal LE histology during implantation has been linked to mid-gestation lethality and poor pregnancy outcomes (Cha et al., 2014; Tu et al., 2016; Zhang et al., 2014). Particularly, WNT5A, a ligand in the non-canonical Wnt signaling pathway, and RBPJ, a mediator of the Notch signaling pathway, are both critical for LE morphology and E-U alignment in the mouse uterus (Cha et al., 2014; Zhang et al., 2014). Moreover, embryo loss in WNT5A- and RBPJ-deficient mice has been attributed to abnormal LE morphology at the time of implantation. We recently reported that WNT5A-deficient mice also display an abnormal 3D luminal folding pattern (Arora et al., 2016). While both WNT5A- and RBPJ-deficient mice display aberrations in LE, it is unclear how 3D luminal folding affects implantation and pregnancy outcomes. The region of the embryo that initiates attachment to the uterine lumen can differ between mammals. In women and horses, the embryo's polar trophectoderm (embryonic pole) initiates attachment to the uterine LE (Ginther, 1983; Kirby et al., 1967). On the other hand, in rodents, the embryo aligns with the inner cell mass (ICM) and its polar trophectoderm towards the uterine M-pole and attachment initiates at the mural trophectoderm (abembryonic pole) that faces the uterine AM-pole. Embryo-Uterine axes (E-U) alignment is crucial for mammalian pregnancy. In horses, factors including uterine contractions and differential thickening of the uterine walls, enable embryo orientation to place its embryonic pole at the uterine AM-pole (Ginther, 1983; Silva and Ginther, 2006). However, the morphological features of the uterine lumen that enable E-U alignment during implantation remain to be discovered. Interestingly, both WNT5A- and RBPJ-deficient mice have defective E-U alignment post implantation. Although the defective E-U alignment has been correlated with aberrant luminal morphology, how the 3D luminal folding pattern and chamber formation affect E-U alignment remains obscure. Using WNT5A- and RBPJ-deficient mouse models, we show that aberrant folding pattern causes embryo trapping in folds leading to disrupted E-U alignment, abnormal chamber formation and defective embryo morphogenesis ultimately leading to embryo demise.

4.2 Results

4.2.1 Embryos localize in aberrant longitudinal folds instead of flat peri-implantation regions in *Wnt5a*^{cKO} uteri

WNT5A-deficient mice display abnormal 2D luminal histology leading to defective implantation, decidualization, embryo orientation and placentation, with around 67% of the embryos dying mid-gestation (Cha et al., 2014). Further, these mice display longitudinal (and not transverse folds) during peri-implantation stages of pregnancy (Arora et al., 2016). To examine how aberrant folding disrupts implantation, we combined uterine-specific *Pgr-Cre* with a *Wnt5a* conditional allele to generate *Pgr*$^{Cre/+}$;*Wnt5a*$^{flox/flox}$ (*Wnt5a*^{cKO}) mice. Notably our studies in Figure 1 were performed with CD1 (mixed-background) mice whereas the *Wnt5a*^{cKO} mice were on C57BL/6 background. First, we observed that at GD3 1200 h, control uteri (*Wnt5a*$^{flox/flox}$) displayed only transverse folds (mean=22.56°) (Fig. 4.1A,C). These data suggest that uterine folding occurs independent of mouse genetic background. The *Wnt5a*^{cKO} uteri have aberrant longitudinal folds aligned along the O-Cx axis (mean=79.08°) and are significantly different compared to controls ($P<0.001$, Mann-Whitney U test) (Figs 4.1B,C and 4.2). In addition, we noted that the width of the lumen along M-AM axis in the *Wnt5a*^{cKO} was significantly higher compared to controls (P=0.01, Mann-Whitney U test) (Fig. 4.3). During implantation at GD4 1200 h, in the control uteri, 100% of embryos (14 embryos, n=3 mice) implant in the flat PIR (Fig. 4.1D). However, in *Wnt5a*^{cKO} uteri on GD4 1200 h, aberrant longitudinal folds persist in PIRs and ~37% of embryos (6/16 embryos, n=3 mice) are trapped in these longitudinal folds away from the AM-pole (Fig. 4.1E).

4.2.2 Embryos in longitudinal folds display defective embryo-uterine axes alignment and chamber formation

At GD4 1200 h in the control uteri embryos attach with their mural trophectoderm facing the AM-pole (Fig. 4.1D). Additionally, PTGS2 (COX2), a marker for decidualization, is expressed in the subepithelial stroma under the mural trophectoderm at the chamber AM-pole. Embryos trapped in folds in the *Wnt5a*^{cKO} uteri do express PTGS2 at the mural trophectoderm side of the embryo but this expression is not at the AM-pole. This suggests a misalignment of the embryo axis along the uterine axis. Moreover, implantation sites with embryos trapped in longitudinal folds fail to initiate chamber formation, on GD4 1200 h (Fig. 4.1E). Embryos in *Wnt5a*^{cKO} uteri that escape the longitudinal folds attach in flat regions at the AM-pole and form V-shaped chambers (Fig. 4.1F).

Wnt5a^{cKO} mice display delayed implantation (Cha et al., 2014), and thus, at GD4 1200 h embryos could display delayed chamber formation and E-U alignment even if they are not trapped in longitudinal folds. Thus, we performed implantation site analysis and embryo-uterine axes angle quantification, at GD4 1800 h (Figs 4.4A and 4.5A,A’). In the control uteri, 100% of the embryos are located in a V-shaped chamber at the AM-pole and over 96% of the embryos have their embryonic-abembryonic (Em-AbEm) axis aligned with the uterine M-AM axis (mean=17.8°) (Fig. 4.1G,J and Table 1). On the other hand, in *Wnt5a*^{cKO} uteri at GD4 1800 h, we observe two groups of embryos. Around 42% of the embryos are trapped in aberrant longitudinal folds and over 95% of those (40.38% of total) have disrupted E-U alignment. Instead of the Em-AbEm axis being parallel to the M-AM axis, 95% of the embryos trapped in folds have their axis almost perpendicular to the M-AM axis (mean=82.22°, $P<0.001$) (Fig. 4.1H,J and Table 1). Moreover, embryos trapped in folds have smaller chambers growing away from the AM-pole, along the left-right axis of the uterus. The remaining 58% of embryos in the *Wnt5a*^{cKO} uteri that have escaped the aberrant longitudinal folds, appear similar to the control uteri with a V-shaped chamber at the AM-pole and over 90% of those have their Em-AbEm axis aligned along the M-AM axis (mean=25.48°, $P>0.05$) (Fig. 4.1I,J and Table 1).

4.2.3 Implantation chamber formation mediates embryo-uterine axes alignment

While we observe that in the *Wnt5a*^{cKO} uteri, 95% of embryos trapped in longitudinal folds have disrupted E-U alignment, the mechanism by which the embryos align with the uterine M-AM axis remains unclear. To understand how the lumen structure and the folding pattern facilitate embryo-uterine axes alignment, we examined embryo orientation relative to the luminal structure in control mice from GD3 1200 h to GD4 1200 h. At GD3 1200 h during the clustered phase of embryo movement (Flores et al., 2020), the Em-AbEm axis of the embryos is randomly oriented with respect to the M-AM axis (mean=77.57°, Standard Deviation (SD)=39.17°) (Figs 4.6A,E and 4.7A). At the onset of implantation, on GD4 0000 h, the Em-AbEm axis of the embryos is almost perpendicular to the M-AM axis (mean=89.58°, SD=9.87°) (Fig. 4.6B,E). The initiation of implantation is evident from the expression of PTGS2 in the LE, near the mural trophectoderm at the abembryonic pole of the embryo (Figs 4.6B and 4.7B) (Scherle et al., 2000). A few hours later, on GD4 0600 h, a small chamber is formed at the AM-pole and expression of PTGS2 shifts from the LE to the stroma under the chamber. Concurrent with chamber formation, embryo rotation is also initiated with the embryos oriented at an acute angle with respect to the M-AM axis (mean=60.7°, SD=17.54°, $P<0.001$, GD4 0000 h vs GD4 0600 h) (Figs 4.6C,E and 4.7C). Notably, one side of the embryo is in contact with the wall of the chamber in 86% of embryos (n=12/14 embryos from 3 mice). This suggests that the embryo may depend on the chamber for rotation. At GD4 1200 h, consistent with the increase in the size of the chamber at the AM-pole, embryo rotation is complete with its axis almost parallel to the uterine M-AM axis (mean= 13.10°, SD=9.07°, $P<0.001$, GD4 0600 h vs GD4 1200 h) (Figs 4.6D,E and 4.7D).

We postulated that if embryo rotation is dependent on the implantation chamber then during the period when rotation is observed (between GD4 0600h and GD4 1200h), the position of the embryo with respect to the chamber should stay constant. To this end we used the ICM (for embryo position) and assessed its location with respect to the expression of stromal PTGS2 under the chamber (for chamber position). We measured the angle between the embryonic-abembryonic axis and the embryonic (ICM)-PTGS2 axis on GD4 0600 h and GD4 1200 h (Fig. 4.8A,B). We observe that there is no significance difference in the mean angle between these two axes at GD4 0600 h (mean=8.2°) and at GD4 1200 h (mean=9.8°). This suggests that the relative position of the embryo and stromal PTGS2 under the chamber is maintained during embryo rotation ($P=0.88$, Mann-Whitney U test) (Fig. 4.8C). These data suggest that embryo-uterine orientation during implantation is facilitated by formation of a chamber at the AM-pole in flat PIRs.

Based on these data, we hypothesized that for axis alignment, embryos in the *Wnt5a*^{cKO} uteri should behave similar to embryos in control uteri until chamber formation initiates. Consequently at GD4 0000h, we observed that similar to controls (Fig. 4.9A), all embryos in the *Wnt5a*^{cKO} (including 33% of embryos trapped in longitudinal folds) are aligned with their Em-AbEm axis almost perpendicular to the M-AM axis irrespective of their localization (Fig. 4.9B,C). Thus, in *Wnt5a*^{cKO}, embryos in longitudinal folds stay perpendicular to the M-AM axis from GD4 0000h until GD4 1800 h (Fig. 4.1H) while embryos that escape longitudinal folds are able to align along the M-AM axis at GD4 1800 h concomitant with chamber formation (Fig. 4.1I).

4.2.4 Misalignment of embryo-uterine axis in *Wnt5a*^{cKO} uteri leads to defective post-implantation embryo morphogenesis

To determine the effect of embryo-uterine misalignment on embryo morphogenesis, we analyzed implantation sites within decidua in *Wnt5a*^{cKO} uteri and control uteri on GD5 1200 h. We observe that in the *Wnt5a*^{cKO} uteri, embryos continue to be misaligned. We also observe that the space between the embryo and the maternal decidua is abnormal in the embryos that are misaligned. We measured the ratio of spaces between the maternal tissue and the epiblast of the embryo on the anterior and posterior ends (z), and the angle of the embryo axis with the M-AM axis (ϕ) (Hiramatsu et al., 2013). In control uteri, 100% of the embryos are oriented along the M-AM axis or proximal-distal axis (mean ϕ=14.26°, Table 1) and the value of z is closer to 1 (mean z=1.31) (Fig. 4.10A,C). However, in the *Wnt5a*^{cKO} uteri, the mean ϕ is higher compared to the control uteri (mean

ϕ=31.49°, $P<0.001$, Mann-Whitney U test) (Fig. 4.10B,C). 35% of the embryos appear to be severely misaligned ($\phi > 40^o$). Further the embryos have highly uneven buffer spaces (mean $z=2.35$, $P<0.001$, Mann-Whitney U test) with ~42% of the embryos displaying $z>2$. Strikingly, 81% of embryos (29% of total) that are misaligned along the uterine axis have $z>2$ (Table 1). Correlation analysis shows a significant correlation between E-U alignment angle and ratio of spaces between embryo and maternal tissue in *Wnt5a*^{cKO} uteri (Pearson's correlation coefficient $R=0.65$, $P<0.001$). These data suggest that E-U misalignment leads to defective embryo morphogenesis.

4.2.5 Defective embryo-uterine axes alignment in *Rbpj*^{cKO} uteri is due to aberrant longitudinal folds

E-U misalignment in *Wnt5a*^{cKO} mice could be due to the effect of WNT5A signaling on uterine folding or due to a different process regulated by WNT5A. We hypothesized that mutants with aberrant folding pattern must show defective E-U alignment irrespective of the signaling pathway involved. Thus, we searched the literature for genetic mutants with known defects in E-U misalignment without a known effect on uterine folding. We examined RBPJ-deficient mice with known defects in E-U alignment and predicted that the E-U misalignment in these mice would be a result of aberrant pre-implantation folds. We generated RBPJ-deficient mice (*Rbpj*^{cKO}*, Pgr*$^{Cre/+}$*;Rbpj*$^{flox/flox}$) by combining a *Rbpj* conditional allele (*Rbpj*$^{flox/flox}$) with the *Pgr-Cre.* At GD3 1200 h, control uteri (*Rbpj*$^{flox/flox}$) have transverse folds (mean=16.18°) (Fig. 4.11A,C). In contrast, as predicted, the folding pattern in *Rbpj*^{cKO} uteri is aberrant, with longitudinal folds running along O-Cx axis instead of transverse folds along M-AM axis (mean=71.79°, $P<0.001$, Mann-Whitney U test) (Fig. 4.11B,C). Post implantation, at GD4 1800h, embryos in control uteri are located in V-shaped chambers at the AM-pole in flat PIRs, with their Em-AbEm axis aligned along the M-AM axis (mean=15.96°) (Fig. 4.11D,G). However, in *Rbpj*^{cKO} uteri, similar to *Wnt5a*^{cKO} uteri, we observe two groups of embryos. About 46% of embryos in *Rbpj*^{cKO} uteri are trapped in aberrant longitudinal folds retained at PIRs, with abnormal expression pattern of PTGS2 and defective chamber formation. Furthermore, 100% of embryos trapped in folds have disrupted E-U alignment as compared to control uteri (mean=72.32°, $P<0.001$, Kruskal-Wallis test, Dunn's multiple comparison) (Fig. 4.11E,G). The remaining 54% of the embryos in the *Rbpj*^{cKO} uteri that have escaped aberrant folds have a V-shaped chamber, normal PTGS2 expression pattern and normal E-U alignment, similar to control uteri (mean=14.35°, $P>0.05$, Kruskal-Wallis test, Dunn's multiple comparison) (Fig. 4.11F,G). Taken together, these results suggest that longitudinal folds in the pre-implantation uterus are detrimental for E-U alignment and proper chamber formation irrespective of the signaling pathway affected.

4.3 Discussion

4.3.1 Transverse folding pattern may be necessary for embryo movement and localization to the AM-pole but is dispensable for embryo spacing

Before embryo entry, both longitudinal and transverse folds are present in the mouse uterus but only longitudinal folds remain during and right after embryo entry. Thus, we propose that longitudinal folds aid in the transport of embryos from the oviductal end towards the center of the horn during unidirectional clustered embryo movement. These observations are similar to those in horses where longitudinal endometrial folds are believed to enable the movement of the embryo through the entire length of the uterus before the embryo implants (Ginther, 1985). Embryos in both *Wnt5a*^{cKO} and *Rbpj*^{cKO} uteri are trapped in longitudinal folds along O-Cx axis, away from the AM-pole, thus transverse folds along M-AM axis, serve as conduits for localizing embryos to the AM-pole. It is tempting to postulate that transverse folds could aid in spacing of embryos along the O-Cx axis in the scattering phase of embryo movement. However, although we did observe aberrant longitudinal folds in *Wnt5a*^{cKO} or *Rbpj*^{cKO} mice pre-implantation, we did not observe embryo crowding. This suggests that longitudinal folds do not cause embryo crowding and conversely transverse folds do not aid in fine embryo spacing.

4.3.2 Transverse folds are naturally selected to avoid trapping of embryos in folds

Our data show that transverse folds resolve to form flat PIRs and the embryos eventually attach in the middle of a PIR. If the embryo requires a flat space to attach then why the lumen forms transverse folds in the peri-implantation phase, instead of completely losing all its folds is puzzling. An explanation can be inferred from the *Wnt5a*^{cKO} and *Rbpj*^{cKO} uteri, where the aberrant pre-implantation longitudinal folds do not completely resolve in the PIRs causing embryo trapping at implantation sites. Hence, it is possible that luminal stretching in opposing directions can only be induced along the O-Cx axis. This would imply that luminal stretching can only effectively flatten transverse folds and fails to flatten longitudinal folds. We did not observe a direct correlation between transverse folds and E-U alignment or chamber formation. Thus, we propose that formation of transverse folds prior to implantation, is an evolutionary selection to abolish longitudinal folds that serve as potential traps for embryos preventing them from localizing to the AM-pole thus disrupting implantation outcomes. This idea is further supported by the fact that even though majority of pre-implantation folds in both *Wnt5a*^{cKO} and *Rbpj*^{cKO} uteri are predominantly longitudinal, less than half of the embryos are trapped in these aberrant folds and the remaining half escape the longitudinal folds and occupy flat regions at the AM-pole. We conclude that although the significance of transverse folds is still unclear, longitudinal folds are detrimental to embryo implantation and pregnancy success. A mouse model that lacks any folds will help clarify the role of transverse folds during implantation and will be a scope for future investigation.

4.3.3 Chamber formation enables embryo rotation to orient ICM towards mesometrial pole

E-U alignment is crucial for a successful pregnancy. Since the maternal uterine arteries enter the mouse uterus at the M-pole, it is essential for the embryo to be oriented with the ICM facing the M-pole. Although embryonic factors such as FGFR2 have been shown to be crucial for blastocyst alignment within the chamber, the role of the uterine environment in E-U alignment is not yet known (Arman et al., 1998). While it has been postulated that the ICM within the embryo is mobile and may migrate within the blastocoel to orient itself towards the M-pole, there is no evidence to support this theory (Kirby et al., 1967). Embryo rotation as a whole, on the hand has been suggested to facilitate E-U alignment in several species including horses and bats (Ginther, 1983; Rasweiler IV and Badwaik, 1999). In bats, the embryo rotates 90^{o} after initiation of implantation such that the ICM is oriented towards the maternal vasculature entering the uterus (Rasweiler IV and Badwaik, 1999). In horses, uterine contractions help in orienting the embryonic vesicle to ensure that the umbilical cord attaches to the allantoic sac. Embryo orientation in horses is further aided by cross ridging of endometrial folds (Ginther, 1998). In the mouse, several factors including myometrial contractions, physical shape of chamber, anchorage of trophoblast to the epithelium and movement of uterine epithelial cells independent of the stroma have been proposed to aid with embryo rotation (Kirby et al., 1967). While it has been suggested that the surface of the embryo has a uniform potential to initiate implantation and hence can attach at any random spot, our study shows that implantation always initiates at the mural trophectoderm opposite to the ICM. Further, our data shows that although embryo orientation is concurrent with chamber formation, embryos are incapable of self-rotation, suggesting that chamber formation and elongation are required for embryo rotation to ensure E-U alignment. The fact that beads that lack any kind of internal axes form V-shaped chambers at the AM-pole when coated with HBEGF (Yuan et al., 2018), suggests that that chamber formation occurs irrespective of the orientation of the embryo but embryo orientation along the M-AM axis is reliant on appropriate chamber formation.

Placentation is a crucial event in mammalian pregnancy. In mice, bats and horses, the placenta always develops dorsal to the ICM and orientation of the ICM towards the maternal vasculature is associated with normal development (Ginther, 1983; Kirby et al., 1967; Rasweiler IV and Badwaik, 1999). While normal placenta formation in women occurs in the upper wall of the uterus away from the cervix, in pathological conditions such as low-lying placenta or placenta previa the placenta is formed in the lower wall blocking the cervix, leading to pregnancy complications (Jansen et al., 2020). Our study connects abnormal uterine folding to E-U misalignment and this provides new uterine 3D-structure based avenues for identifying the cause of placental abnormalities.

4.3.4 Aberrant folding and resulting phenotypes in ***Wnt5a***^{cKO} and ***Rbpj***^{cKO} mice: Comparison with published studies

It is well known that changes in luminal epithelial morphology during pregnancy are critical for embryo implantation and pregnancy outcomes (Aplin and Ruane, 2017). By using the *Wnt5a*^{cKO} mice as a model system for aberrant folds, we delineated the sequence of events that correlate how aberrant structure could cause embryo lethality (Table 1). While Cha *et al*. (Cha et al., 2014) showed that M-AM orientation of implantation sites in *Wnt5a*^{cKO} uteri is abnormal on GD7, we show that embryo orientation defects arise due to unresolved longitudinal folds as early as GD4. Further, Cha *et al*. (Cha et al., 2014) showed 67% resorption rate at mid gestation and ~50% reduction in litter size at birth in the *Wnt5a*^{cKO} mice, our data shows ~25% resorption at mid gestation (Fig. 4.4B) and ~35% reduction in litter size at birth. The difference in penetrance of the embryo survival phenotypes could be due to the difference in background of mice used for these studies. Most importantly, our data support that the proportion of embryos trapped in longitudinal folds at implantation (~40%) correlate with the reduction in litter size (35%).

For the *Rbpj*^{cKO} mice, Zhang et al. (Zhang et al., 2014) attributed E-U misalignment to abnormal luminal closure. However, we show that longitudinal folding pattern in the *Rbpj*^{cKO} uteri, is the more likely cause of E-U misalignment. This is supported by the timing of luminal closure that happens around GD3 1600 h (Yoshinaga, 2013) whereas aberrations in pre-implantation fold formation are observed as early as GD3 1200 h in the *Rbpj*^{cKO} uteri. Zhang *et al.* (Zhang et al., 2014) also concluded that defective luminal closure causes extra luminal folds in the *Rbpj*^{cKO} uteri at implantation. Our data supports that luminal folds continue to be present in both control and *Rbpj*^{cKO} uteri post-implantation but it is the aberrant longitudinal folds in the *Rbpj*^{cKO} mice that disrupt embryo implantation.

4.3.5 Transverse folding ensures E-U alignment for post-implantation embryo morphogenesis

The mechanical and structural aspects of the maternal environment that affect embryo morphogenesis are not fully understood (Matsuo and Hiramatsu, 2017). Mechanical forces exerted from the maternal tissue is required for egg cylinder morphogenesis, elongation of the embryo along the M-AM axis, correct specification of the distal visceral endoderm and anterior-posterior axis specification (Hiramatsu et al., 2013; Ueda et al., 2020). Our data shows that aberrant luminal folding pattern in mice affects embryo orientation, which in turn affects buffer space between embryo and maternal decidua during morphogenesis. Future investigation is required to delineate how the abnormal space surrounding the embryo affects embryo morphogenesis during development potentially leading to embryo mortality.

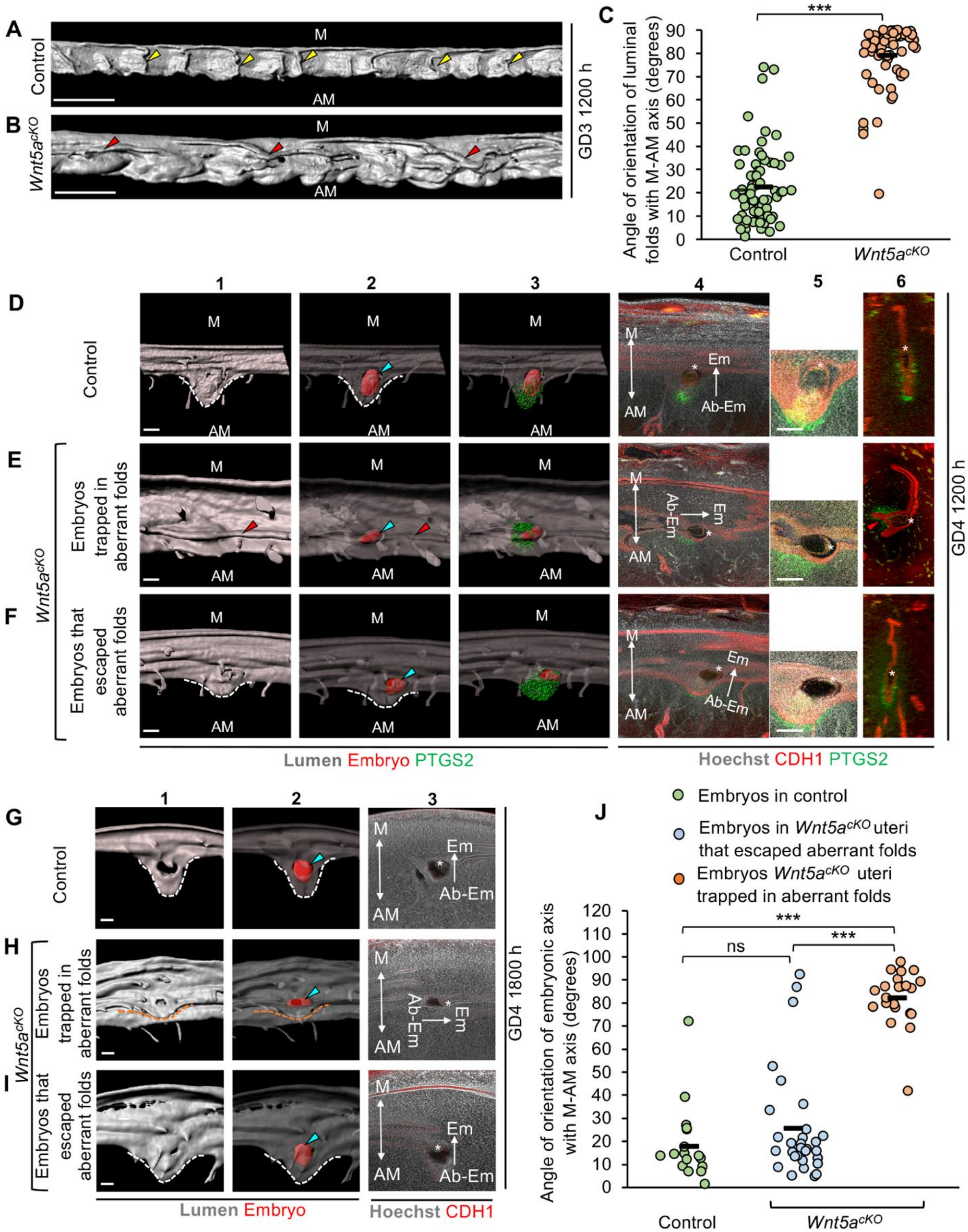

Figure 4.1: Aberrant pre-implantation folding in *Wnt5a*^{cKO} leads to disrupted embryo-uterine axes alignment and abnormal chamber formation.

Figure 4.1 (cont'd)

(A,B) 3D reconstruction of lumen in control (A) and *Wnt5a*^{cKO} (B) uteri at GD3 1200 h. Yellow arrowheads indicate transverse folds. Red arrowheads indicate longitudinal folds. Blue arrowheads indicate embryos (red surface). Scale bars: 1000 µm. (C) Quantification of fold angle with M-AM axis in control and *Wnt5a*^{cKO} (*n*=3 mice/group) uteri on GD3 1200 h (****P*<0.001, Mann–Whitney *U*-test). (D-F) 3D surface view and optical slice view of implantation sites at GD4 1200 h in control (D) and *Wnt5a*^{cKO} (E,F) uteri. Implantation sites in *Wnt5a*^{cKO} uteri where embryos are trapped in folds (E) or where embryos have escaped folds (F). Panel 1: 3D lumen surface (gray). Panel 2: transparent 3D lumen and embryo (red) surface. Panel 3: transparent 3D lumen, embryo and PTGS2 (green) surface. Panel 4: optical slice with frontal view. Panel 5: high-magnification image of embryos in panel 4. Panel 6: optical slice with transverse view. Scale bars: 100 µm. (G-I) 3D surface view and optical slice view of implantation sites on GD4 1800 h in control (G) and *Wnt5a*^{cKO} (H,I) uteri. Implantation sites in *Wnt5a*^{cKO} uteri where embryos are trapped in folds (H) or where embryos have escaped folds (I). Panel 1: 3D lumen surface (gray). Panel 2: transparent 3D lumen and embryo (red) surface. Panel 3: optical slice with frontal view. Scale bars: 100 µm. (J) Quantification of embryo orientation with respect to M-AM axis in control (*n*=3 mice, n_e=26 embryos) and *Wnt5a*^{cKO} (*n*=6 mice, n_e=52 embryos) uteri at GD4 1800 h. (****P*<0.001, Kruskal–Wallis test, Dunn's multiple comparison). ns, non-significant. M, mesometrial pole; AM, anti-mesometrial pole; Em, embryonic pole; Ab-Em, abembryonic pole. Black dashes indicate the mean angle. Asterisks in D-I indicate inner cell mass.

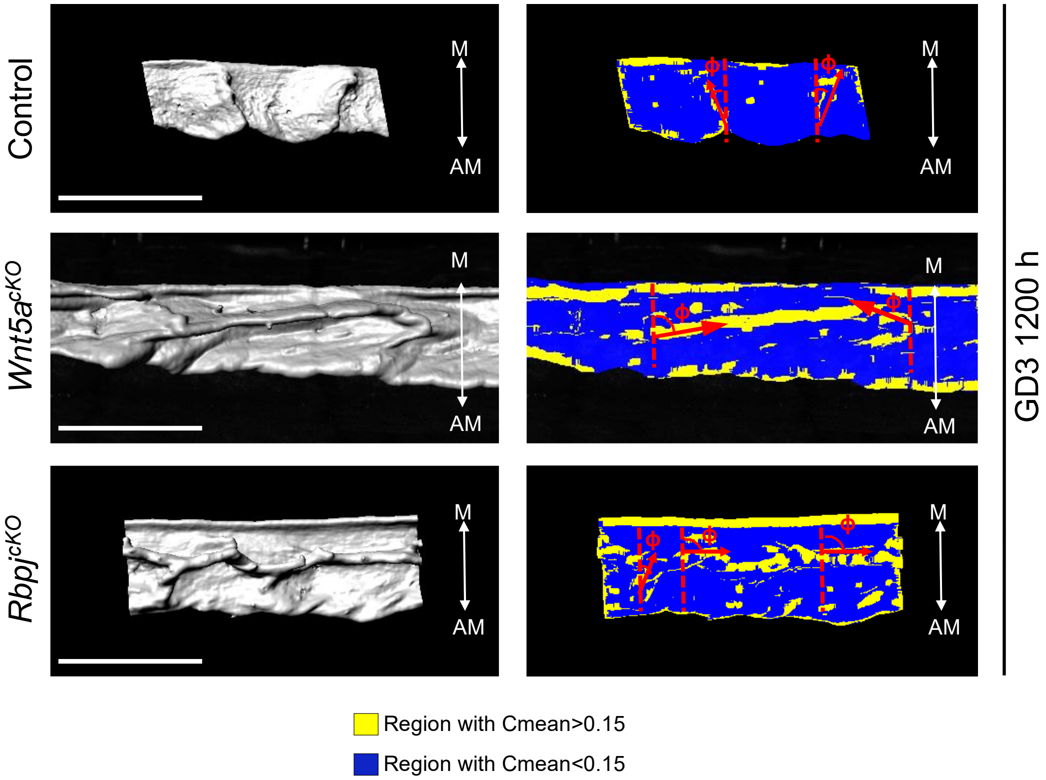

Figure 4.2: Quantification of luminal fold angle in *Wnt5a*^{cKO} and *Rbpj*^{cKO}.
3D surface view and corresponding view with surface curvature analysis in control, *Wnt5a*^{cKO} and *Rbpj*^{cKO} at GD3 1200 h. Cmean - Curvature mean. ϕ - angle made by fold with respect to M-AM axis. (Scale bars: 1000µm).

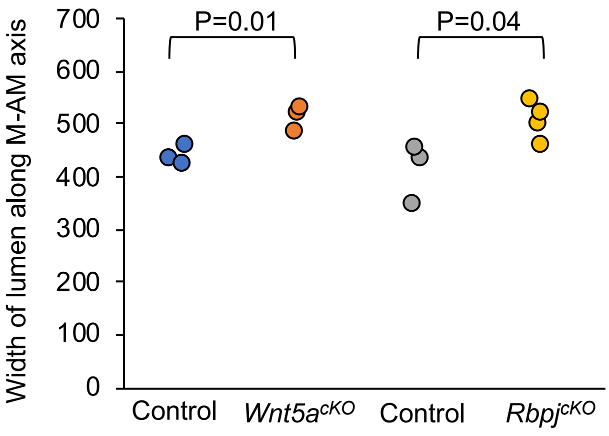

Figure 4.3: Comparison of lumen widths in *Wnt5a*^{cKO} and *Rbpj*^{cKO} compared to controls.

Quantification of width of lumen along M-AM axis in *Wnt5a*^{cKO} (n=3) and *Rbpj*^{cKO} (n=4) at GD3 1200 h along with respective controls (n=3 for each group). P, Student’s unpaired t test.

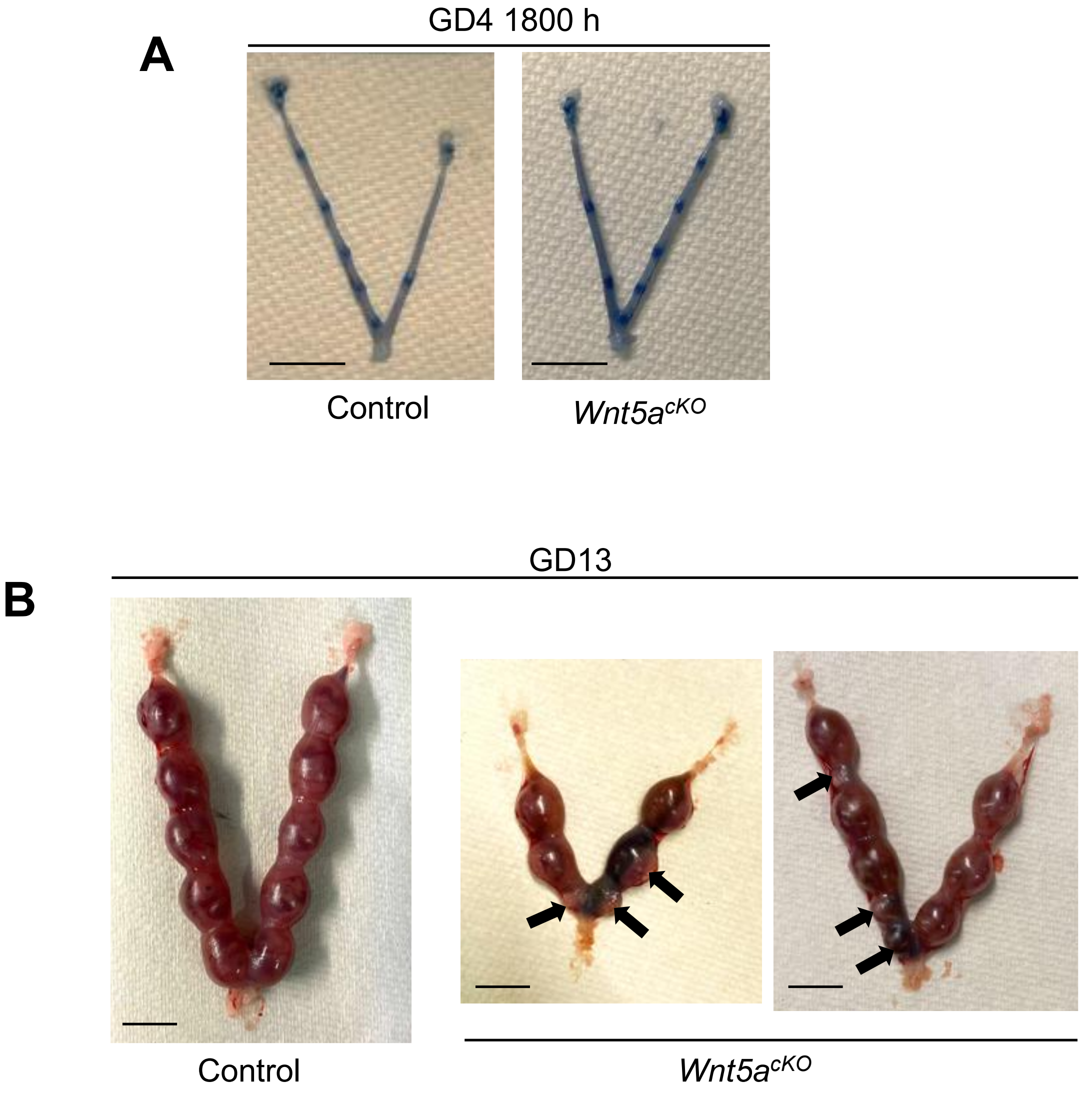

Figure 4.4: Post-implantation embryo development in *Wnt5a*^{cKO} and control uteri. (A) Implantation sites in control and *Wnt5a*^{cKO} uteri on GD4 1800 h visualized using Evan's blue dye method. (B) GD13 implantation sites in control and *Wnt5a*^{cKO} uteri. Black arrows: resorption sites. (Scale bars: 1cm).

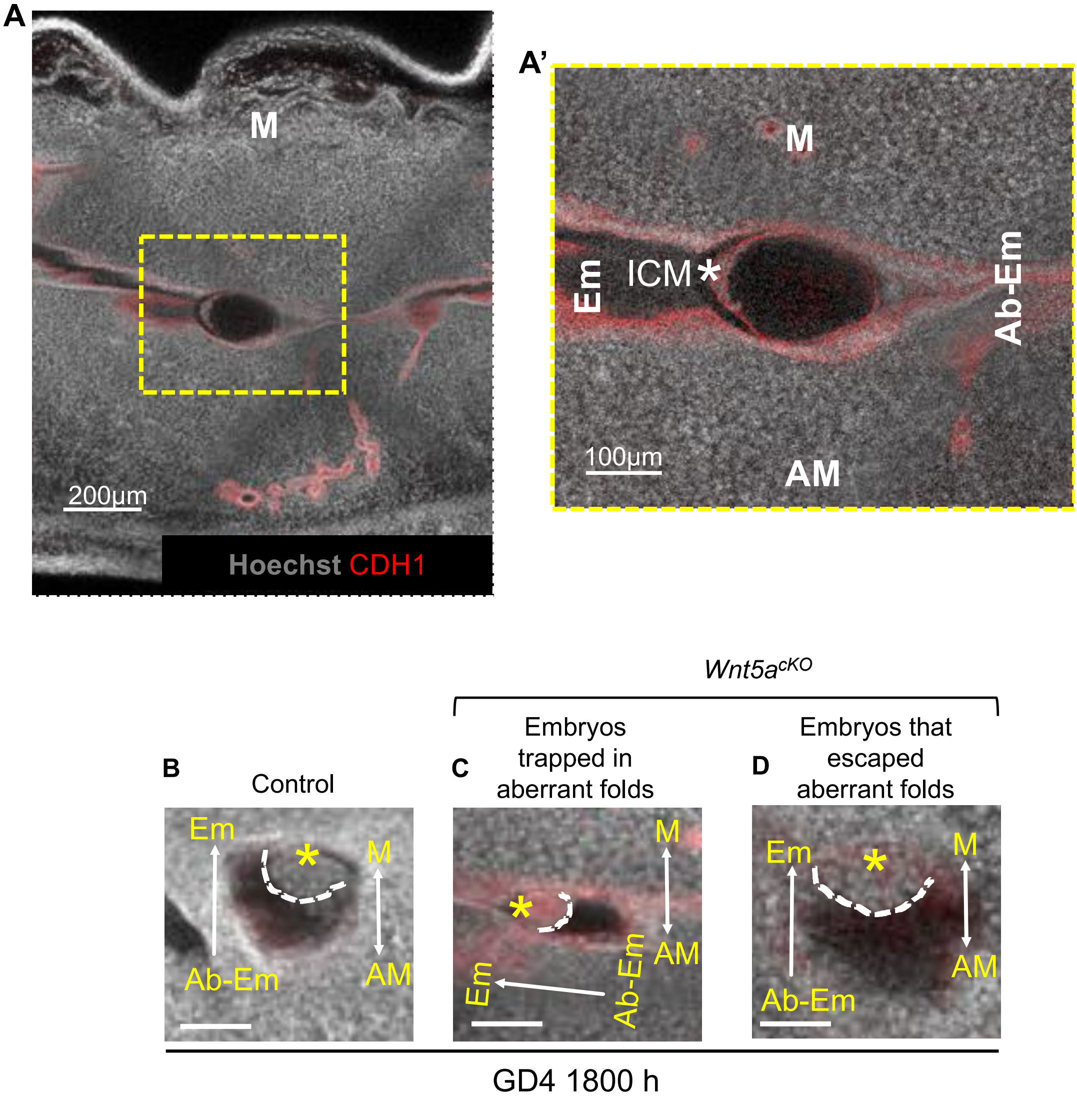

Figure 4.5: High magnification images of embryo within the uterine lumen and determination of embryo axis.

(A,A') Optical slice of embryo within the uterine lumen showing inner cell mass (ICM), embryonic pole (Em) and abembryonic pole (AbEm). (B-D) High magnification images of embryos in Fig. 4 G-I. Asterisk indicates inner cell mass. (Scale bars: 100μm).

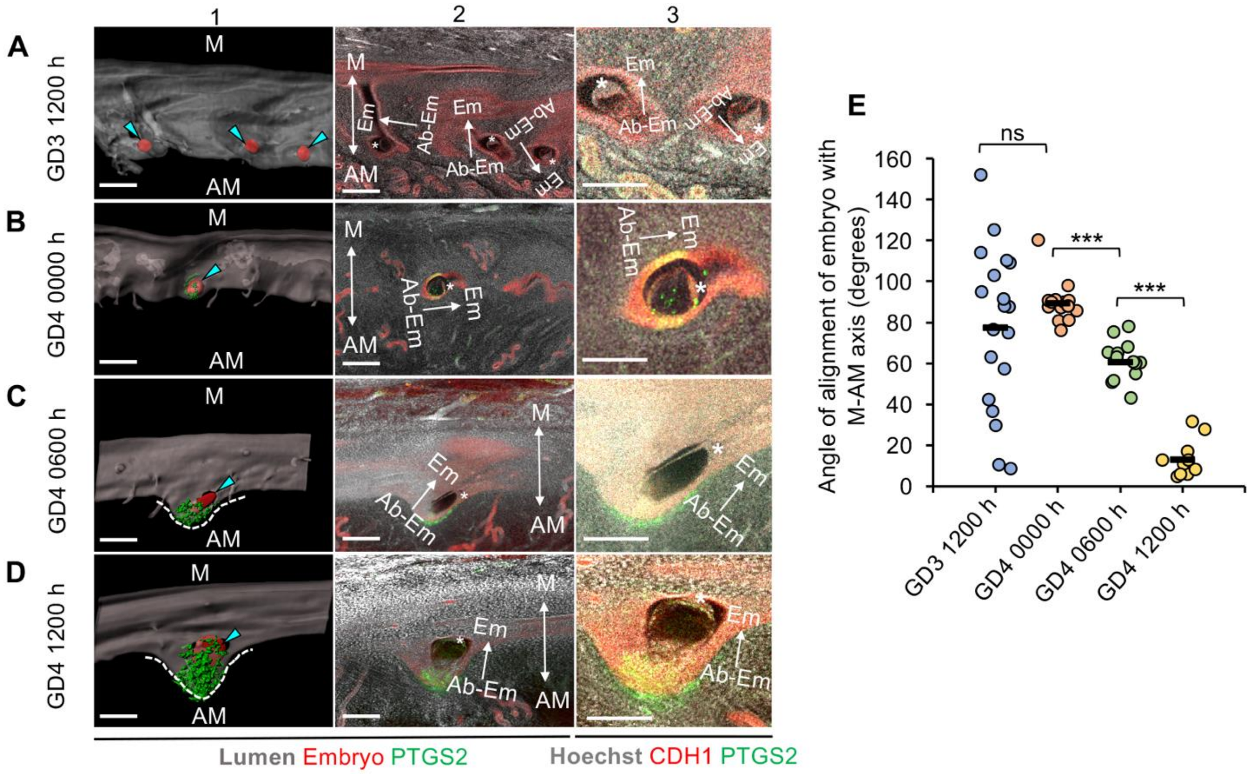

Figure 4.6: Alignment of embryo-uterine axes is facilitated by the formation and elongation of the chamber.

(A-D) The relationship between chamber formation and embryo orientation with respect to M-AM axis in control mice at GD3 1200 h (A), GD4 0000 h (B), GD4 0600 h (C) and GD4 1200 h (D). Panel 1: transparent lumen with PTGS2 (green) and embryo (red). Panel 2: optical slices with CDH1 (red), PTGS2 (green) and Hoechst (gray). Panel 3: high-magnification images of embryos in panel 2. At GD4 0600 h, the embryo appears to be orienting its ICM towards the M pole but is still in contact with one wall of the chamber. Blue arrowheads indicate embryos (red surfaces), White dotted lines indicate the implantation chamber. Asterisks indicate the ICM. M, mesometrial pole; AM, anti-mesometrial pole. Scale bars: 100 µm. (E) Quantification of embryo orientation with respect to the M-AM axis at GD3 1200 h (*n*=3, n_e=19), GD4 0000 h (*n*=3, n_e=15), GD4 0600 h (*n*=4, n_e=14) and GD4 1200 h (*n*=4, n_e=11). *n*, number of mice; n_e, number of embryos. Black lines indicate the mean angle. ***P<0.001; ns, non-significant; Mann–Whitney *U* test.

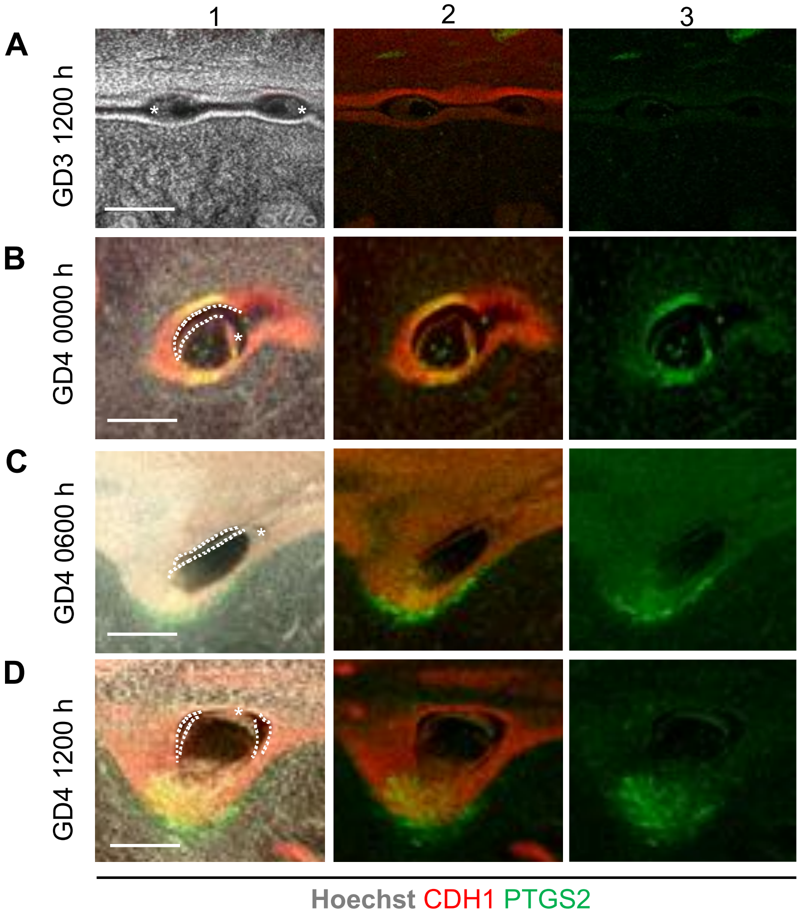

Figure 4.7: High magnification images of PTGS2 expression during embryo alignment.

Optical slice view of PTGS2 expression around embryos on GD3 1200 h (A), GD4 0000 h (B), GD4 0600 h (C) and GD4 1200 h (D). Panel 1: 2D optical slice with Hoechst, CDH1 and PTGS2. Panel 2: 2D optical slice with CDH1 and PTGS2. Panel 3: 2D optical slice with PTGS2 only. Asterisk indicates inner cell mass. (Scale bars: 200µm).

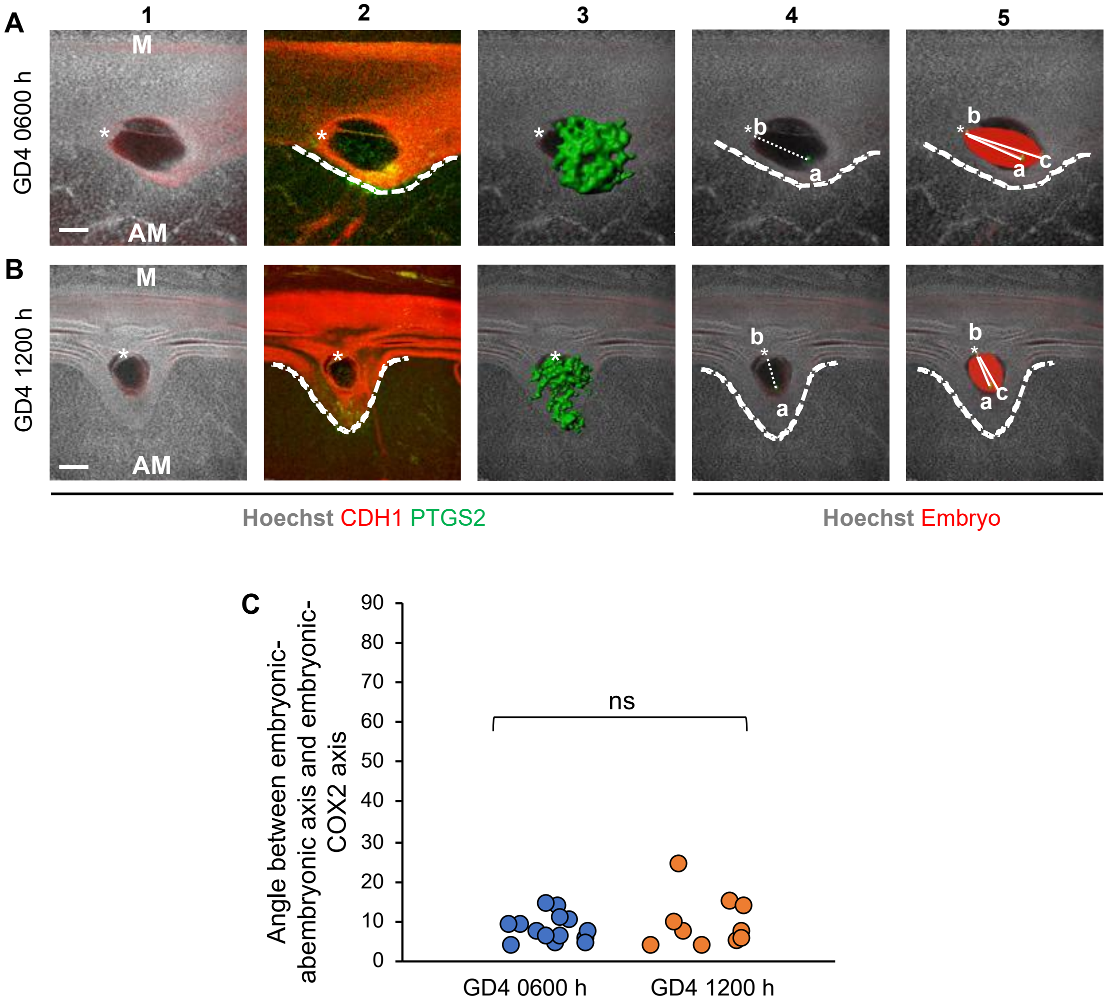

Figure 4.8: Orientation of embryo relative to PTGS2 is maintained during chamber formation and elongation.

(A,B) Relationship between chamber formation, embryo orientation and PTGS2 expression in control mice on GD4 0600 h (A) and GD4 1200 h (B). Panel 1: 2D optical slice view of implantation site with Hoechst and CDH1. Panel 2: 2D optical slice view with PTGS2 (green) and CDH1 (red). Panel 3: optical slice with 3D surface of PTGS2 (green) around chamber. Panel 4: optical slice with embryonic-PTGS2 axis (line ab). Panel 5: optical slice with embryonic-PTGS2 axis and embryonic-abembryonic axis (line bc). White dotted line: implantation chamber. Asterisk: inner cell mass. (Scale bars: 100μm). (C) Quantification of angle between embryonic-PTGS2 axis and embryonic-abembryonic axis on GD4 0600 h (n=3, n_e=19) and GD4 1200 h (n=3, n_e=15). n – number of mice; n_e – number of embryos. (P=0.88, Mann-Whitney U test). ns - non-significant.

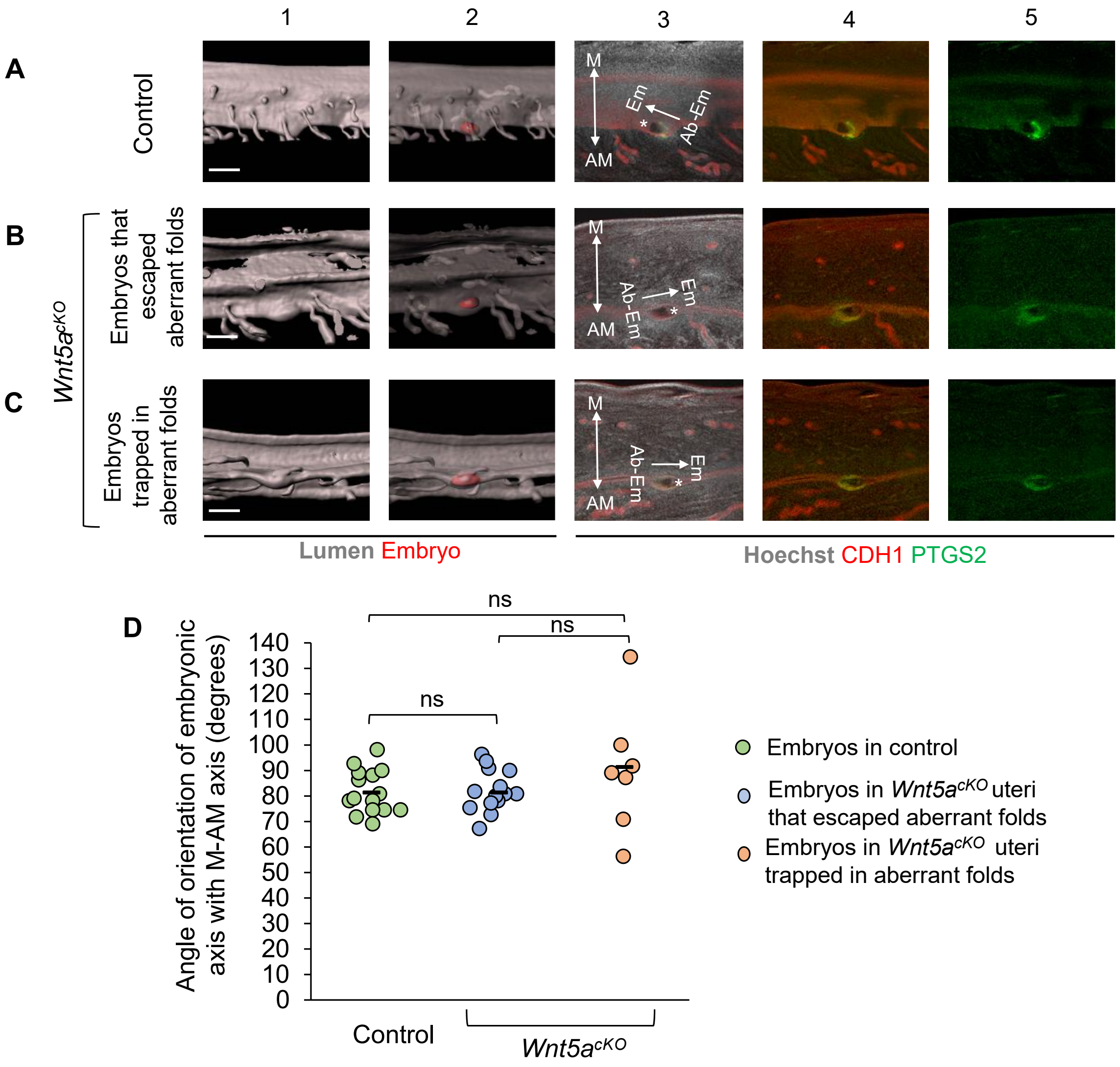

Figure 4.9: Embryo-uterine alignment in *Wnt5a*^{cKO} at GD4 0000h.
(A-C) 3D surface view and optical slice view of implantation sites on GD4 1200 h in control (A) and *Wnt5a*^{cKO} (B,C) uteri. Implantation sites in *Wnt5a*^{cKO} uteri where embryos have escaped folds (B) or where embryos are trapped in folds (C). Panel 1: 3D lumen surface (gray). Panel 2: transparent 3D lumen and embryo (red) surface. Panel 3-5: optical slice view with Hoechst, CDH1 and PTGS2. (Scale bars: 200µm). Asterisk indicates inner cell mass. (D) Quantification of embryo orientation with respect to M-AM axis in control (n=3, n$_e$=21) and *Wnt5a*^{cKO} (n=6, n$_e$=15) uteri on GD4 1800 h. (P=0.54, Kruskal-Wallis test, Dunn's multiple comparison). ns - non-significant. n – number of mice; n$_e$ – number of embryos.

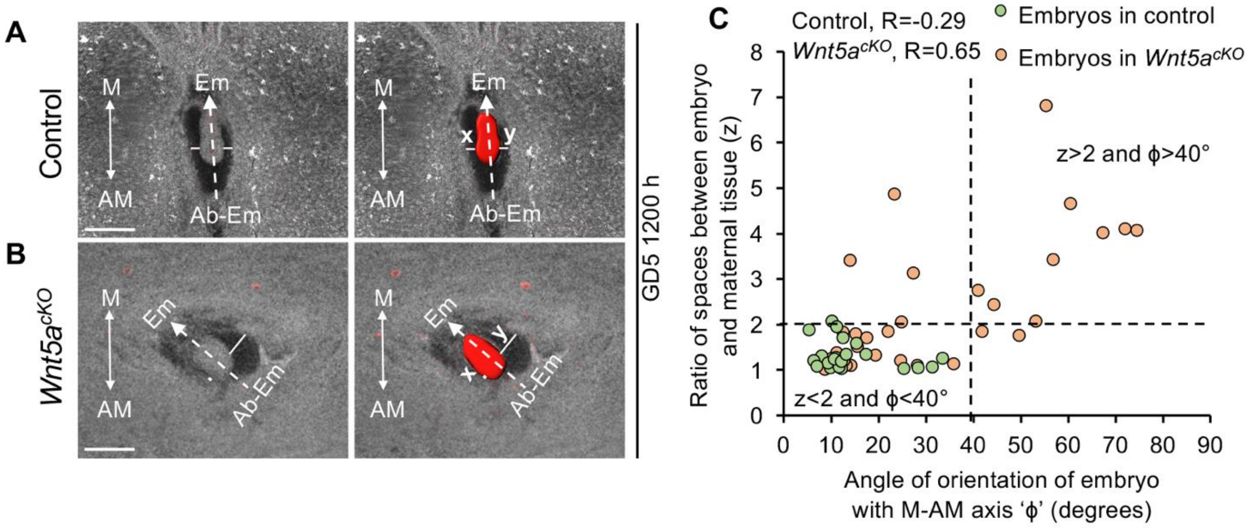

Figure 4.10: Embryo-uterine misalignment leads to defective buffer space between epiblast and maternal decidua.

(A,B) 2D optical slices of implantation sites in control (A) and *Wnt5a*^{cKO} (B) uteri at GD5 1200 h. 3D surface of the embryo (red, right panel). There is uneven buffer space between epiblast and maternal decidua in *Wnt5a*^{cKO} uteri. Scale bars: 1000 µm. (C) Quantification of embryo orientation with respect to the M-AM axis, and ratio of buffer spaces between epiblast and maternal decidua at GD5 1200 h in controls (n=3, n_e=25) and *Wnt5a*^{cKO} (n=3, n_e=33) uteri. n, number of mice; n_e, number of embryos. (Pearson's correlation coefficient, R for control= −0.29, ns, P>0.05; R for *Wnt5a*^{cKO}=0.65, ***P<0.001). z, maximum(x,y)/minimum(x,y). M, mesometrial pole; AM, anti-mesometrial pole; Em, embryonic pole; Ab-Em, abembryonic pole.

Table 1. Correlation between the percentage of abnormal embryos at different stages of development and corresponding embryo loss in litter size

	Control				*Wnt5a*^{cKO}			
GD	*n*	Average[‡]	Phenotype	Phenotype percentage	*n*	Average[‡]	Phenotype	Phenotype percentage
4	3 mice, 26 embryos	8.66	Embryos trapped in aberrant folds	0	6 mice, 52 embryos	8.66	Embryos trapped in aberrant folds	42.3**
5	3 mice, 25 embryos	8.33	Embryos misaligned (Ø>40°)	0	4 mice, 31 embryos	8.85	Embryos misaligned (Ø>40°)	35.48
			Embryos with x/y>2	4			Embryos with x/y>2	41.9
			Misaligned embryos (Ø>40) with x/y>2	0			Misaligned embryos (Ø>40) with x/y>2	29.03
6	3 mice, 27 embryos	8.33	Empty decidua/dying embryos	0	4 mice, 36 embryos	9	Empty decidua/dying embryos	13.88*
13	7 mice, 61 embryos	8.71	Resorption	1.63	8 mice, 55 embryos	6.77	Resorption	24.59**
Litter	7 mice, 63 embryos	10	-	-	8 mice, 47 embryos	5.87***	Embryo loss (compared with controls)	34.77

[‡] Average number of embryos/pups per mouse.

Ø, angle made by Em-AbEm axis with respect to M-AM axis; x and y, space between embryo and maternal tissue on the anterior and posterior ends, respectively; z, ratio of buffer spaces between epiblast and maternal tissue on the anterior and posterior ends; GD, gestational day.

**P*=0.008, ***P*=0.01, ****P*=0.002 (Mann–Whitney *U* test).

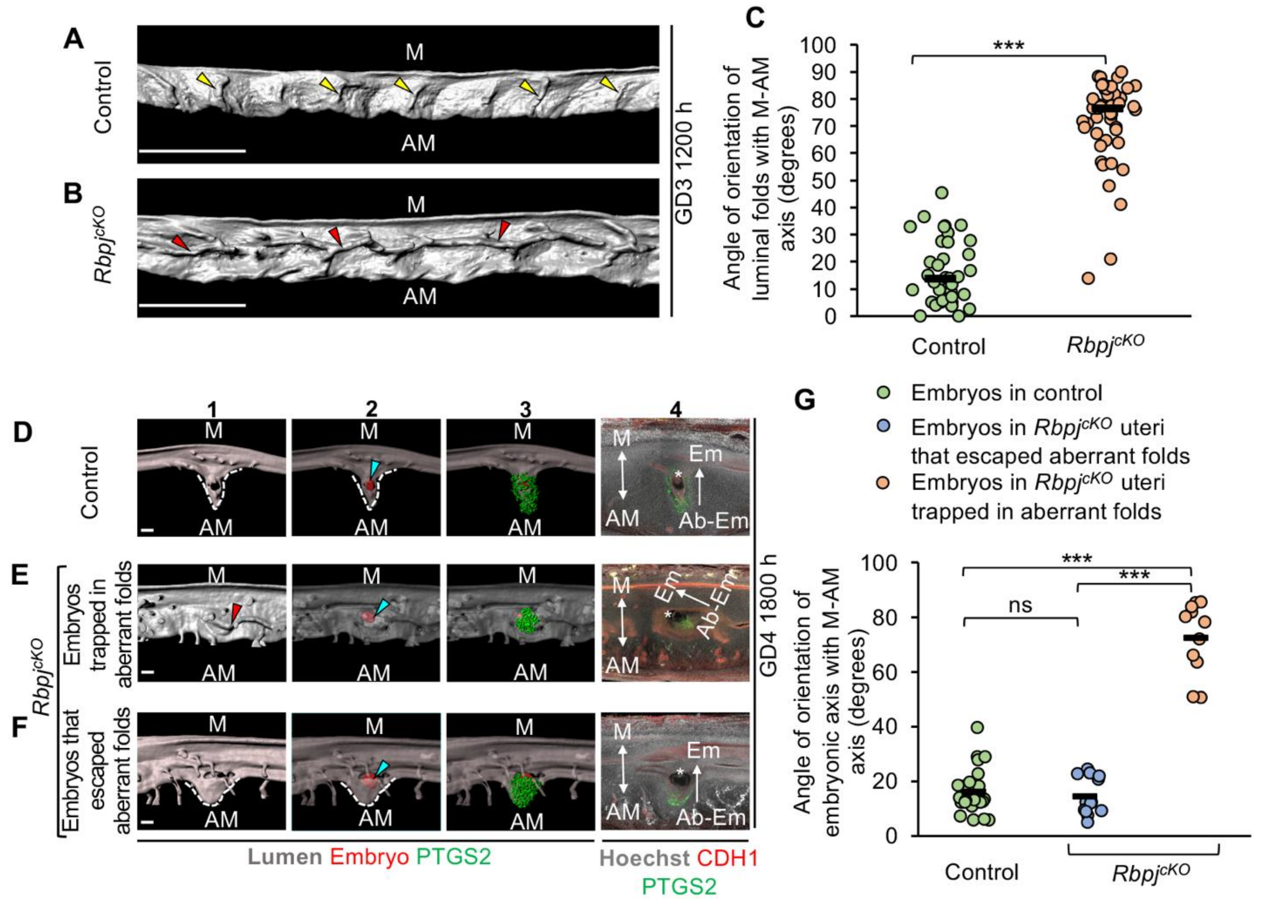

Figure 4.11: Longitudinal folds in *Rbpj*^{cKO} disrupt embryo-uterine axes alignment and chamber formation.

(A,B) 3D reconstruction of lumen in control (A) and *Rbpj*^{cKO} (B) uteri on GD3 1200 h. Yellow arrowheads indicate transverse folds. Red arrowheads indicate longitudinal folds. Scale bars: 1000 µm. (C) Quantification of fold orientation with respect to the M-AM axis in control and *Rbpj*^{cKO} (*n*=3 or 4 mice/group) uteri at GD3 1200 h (****P*<0.001, Mann–Whitney *U* test). (D-F) 3D surface view and optical slice view of implantation sites at GD4 1800 h in control (D) and *Rbpj*^{cKO} (E,F) uteri. Implantation sites in *Rbpj*^{cKO} uteri where embryos are trapped in folds (E) or where embryos have escaped folds (F). Panel 1: 3D lumen surface (gray). Panel 2: transparent 3D lumen surface with embryo surface (red). Panel 3: transparent 3D lumen surface with embryo and PTGS2 (green) surface. Panel 4: optical slice with frontal view. Scale bars: 100 µm. Blue arrowheads indicate embryos (red surfaces). Asterisks indicate inner cell mass. (G) Quantification of embryo orientation with respect to the M-AM axis in control (n=3, n_e=24) and *Rbpj*^{cKO} (n=3, n_e=24) uteri at GD4 1800 h. *n*, number of mice; n_e, number of embryos. (****P*<0.001, Kruskal–Wallis test, Dunn's multiple comparison). ns, non-significant. M, mesometrial pole; AM, anti-mesometrial pole; Em, embryonic pole; Ab-Em, abembryonic pole. Black lines in C,G indicate the mean angle.

Chapter 5: Hormonal regulation of folding – role of estrogen and progesterone signaling

5.1 Introduction

Estrogen (E2) and Progesterone (P4) are the key hormones required for normal uterine function and, initiation and maintenance of pregnancy. E2 and P4 act through their nuclear receptors - estrogen receptor (ESR) and progesterone receptor (PGR) respectively to mediate downstream signaling pathways. In mice, during GD0 and GD1 of early pregnancy, pre-ovulatory E2-ESR signaling via IGF1 stimulates proliferation of the luminal and glandular epithelium (Marquardt et al., 2019). By GD2, P4 levels start to rise and stimulate stromal proliferation. On GD3 and GD4, P4-PGR signaling regulates several genes including *Hand2*, *Ihh* and *Wnt4* to prepare the uterus for implantation (Franco et al., 2012). In addition, an interaction between E2 and P4 signaling mediated various events in different compartments of the uterus including the epithelium, stroma and muscle. The role of E2 and P4 signaling in modulating uterine folding is yet to be studied. Dysregulation of both E2 and P4 signaling in the mouse uterus leads to implantation failure and infertility (Curtis Hewitt et al., 2002; Large and DeMayo, 2012; Lydon et al., 1995; Pawar et al., 2015; Winuthayanon et al., 2010). Whole body knockout of *Esr* and *Pgr* in mice leads to severe infertility due to ovulation and implantation defects (Curtis Hewitt et al., 2002; Lydon et al., 1995). Similarly, epithelial deletion of both *Esr* and *Pgr* also leads to implantation failure (Pawar et al., 2015). However, whether folding is dependent on epithelial E2 and P4 signaling remains unknown.

P4-PGR signaling activates the transcription of several genes such as Indian hedgehog and amphiregulin, required for epithelial structure and function during implantation

(Franco et al., 2012). In humans, Wnt5a is upregulated by P4 signaling in the uterus during the luteal phase (Chi et al., 2019; Rider et al., 2016). In mice, *Wnt5a* is expressed in a spatiotemporal manner along M-AM axis during the receptivity phase, coinciding with *Pgr* expression on GD2 and GD3 when P4 levels are high. Moreover, both PGR and WNT5A deficient mice have abnormal 2D luminal epithelial morphology (Cha et al., 2014; Franco et al., 2012; Lydon et al., 1995; Tan et al., 1999). Our data has also shown that 3D folding pattern is aberrant in the WNT5A deficient mice. Whether P4 regulates Wnt5a expression to modulate folding is unknown. In this chapter, we investigated the role of E2 and P4 in different uterine compartments in regulating the uterine folding pattern. We also examined how P4 interacts with Wnt5a to facilitate transverse folding.

5.2 Results

5.2.1 E2 and P4 signaling in the uterine epithelium are dispensable for transverse folding

Firstly, we wanted to examine if E2 and P4 signaling in the epithelial compartment are necessary for transverse folding. We generated *Esr*^{cKO} (*Ltf*$^{cre/+}$ *Esr*$^{flox/flox}$) and *Pgr*^{cKO} (*Ltf*$^{cre/+}$ *Pgr*$^{flox/flox}$) to delete *Esr* and *Pgr* respectively in the epithelial cells. Since *Ltf* is only expressed in the adult uterine epithelial cells, deletion of *Esr* and *Pgr* occurs only at adulthood (Daikoku et al., 2014). We examined the folding pattern in the IIR of these mice on GD4 1200 h. Note that IIRs in control mice have transverse folds as previously described in chapter 2 (Fig. 5.1A). Surprisingly both *Esr*^{cKO} and *Pgr*^{cKO} have transverse folds comparable to controls (Fig. 5.1B,C). This suggests that E2 and P4 signaling in the epithelial cells are dispensable for transverse folding.

5.2.2 Exogenous treatment with E2 but not P4 leads to disrupted folding

While depletion of E2 and P4 signaling in the epithelium does not affect folding, we wanted to test if increasing E2 and P4 signaling affects folding (Liang et al., 2018). Hence, we treated pregnant mice supraphysiological doses of E2 (200ng/mouse) and P4 (4mg/mouse). Mice treated with vehicle (sesame oil) have normal transverse folds (Fig. 5.2A). Since P4 levels start to increase from GD2, we treated mice with one dose of 4mg P4 on GD2 1800 h and examined folding on GD3 1200 h. We observed that one dose of P4 is not sufficient to affect folding as uteri continue to have normal transverse folds (Fig. 5.2B). However, even when we treated mice with 3 doses of P4 from GD0 to GD2, we did not observe any disruption in the transverse folding pattern (Fig. 5.2C). This suggests that increased P4 signaling is not detrimental to folding. Similarly, since E2 levels are high during GD0 and GD1 in normal pregnancy, we treated mice with a single dose of 200ng E2 on GD0 1200 h or GD1 1200 h. Interestingly, 200ng E2 treatment on either day leads to longitudinal folds on GD3 1200 h, suggesting that high levels of E2 are detrimental to folding (Fig. 5.2D,E).

5.2.3 Reduced P4 signaling in all uterine compartments leads to disrupted folding

While we have shown that P4 signaling in the epithelium is not required for transverse folding, it is possible that P4 signaling in the other uterine compartments such as the stroma and muscle is necessary for transverse folding. To test this hypothesis, we treated mice with RU486 (8mg/kg), a pharmacological inhibitor of P4 signaling on GD2 1800h and examined folding on GD3 1200 h. Interestingly, we observed that the RU486 treated mice have longitudinal folds while the vehicle treated mice have normal transverse folds (Fig. 5.2F). This suggests that while P4 signaling is not required in epithelial cells, it is absolutely essential in non-epithelial uterine compartments for pre-implantation transverse uterine folding. Moreover, while high levels of P4 do not have a negative effect on folding, low levels of P4 is detrimental to folding.

5.2.4 P4 signaling regulates expression of *Wnt5a* in the stroma

Previously we have shown that *Wnt5a* is necessary for transverse folding. Based on interactions between P4 and *Wnt5a* from other studies, we wondered if P4 regulates *Wnt5a* for transverse folding. Previous studies have shown that *Wnt5a* is expressed in the sub-epithelial stroma (Cha et al., 2014). We used RNAscope ISH to determine if the expression of *Wnt5a* mRNA is altered in the uteri of mice treated with 4mg P4 or RU486. In control mice that were treated with vehicle, on GD3 1200 h, *Wnt5a* is expressed in the stroma in a gradient with strong expression in sub-epithelial stroma and no expression in stroma near the muscle (n=5) (Fig. 5.3A). Interestingly we observe that RU486 treatment in the CD1 background leads to complete loss of *Wnt5a* expression in the stroma (n=3) (Fig, 5.3B). Surprisingly, RU486 treatment in the C57BL/6 background leads to increased expression of Wnt5a in 50% of the mice (n=4) as compared to controls (Fig, 5.3B). We observe that the gradient of Wnt5a is disrupted and it is expressed in the entire stroma. On the other hand, high dose P4 treatment leads to a modest expansion of the domain of Wnt5a expression compared to vehicle treated mice (Fig 5.3C).

5.2.5 Interaction between P4 signaling and *Wnt5a* in the stroma for transverse folding

Our studies using *Wnt5a*^{cKO} revealed that depletion of *Wnt5a* signaling leads to aberrant longitudinal folds instead of transverse folds as in controls (Fig. 5.4A,E) . However, in the *Wnt5a*^{cKO}, the *Cre* used to delete the floxed alleles of *Wnt5a* is knocked into the *Pgr* promoter. Hence in addition to deletion of both copies of *Wnt5a*, one copy of *Pgr* is also lost making it heterozygous for *Pgr*. We predicted if there is an interaction between WNT5A and Pgr for transverse folding, deletion of just one copy each of *Wnt5a* and *Pgr* will lead to disrupted folding. Moreover, mice heterozygous for either *Wnt5a* or *Pgr* have normal transverse folds (Fig. 5.4B,C). As predicted, we observed that in the *Wnt5a* and *Pgr* double heterozygous mice, folding was aberrant with the presence of longitudinal folds (Fig. 5.4D). This suggests that an interaction between P4 and *Wnt5a* signaling regulates transverse folding pattern.

5.3 Discussion

5.3.1 Role of E2 signaling in uterine folding

Our data shows that E2 signaling in the uterine epithelium is dispensable for folding. It is possible that E2 signaling is required in other uterine compartments, specifically the stroma and muscle, for transverse folding. Deletion of Esr in the stroma using *Amhr2* $^{Cre/+}$ leads to defective implantation and severe infertility (Winuthayanon et al., 2017). Whether the folding pattern is disrupted in these mice requires future investigation. The role of E2 signaling in non-epithelial cell types for folding can also be examined by blocking E2 signaling using ICI 182,780, a pharmacological inhibitor. This will be a subject of future investigations.

On the contrary, excess E2 signaling disrupts uterine folding causing longitudinal folds. In cows and horses, longitudinal folds are observed during estrous stage when E2 levels are high (Fissore et al., 1986; Hayes et al., 1985). Our data can have important implications for the harmful effects of excess E2 on pregnancy in women. During IVF procedures, hyperstimulation leads to high levels of E2 which are detrimental to implantation and pregnancy success (Simon et al., 1995). The effect of hyperstimulation on uterine folding has been described in Chapter 6. It is possible that excess E2 signaling leads hyperproliferation which in turn disrupts the folding. However, the mechanism by which high E2 signaling disrupts folding is unclear and requires future investigation.

5.3.2 Role of P4 signaling in uterine folding

Abnormal levels of P4 during pregnancy leads to infertility (Robertshaw et al., 2016). In women undergoing ART due to ovarian insufficiency, it has been shown that duration of P4 exposure during window of implantation is critical for successful implantation (Prapas et al., 1998). Endometrial folds have been shown to exist in humans during the luteal phase of menstrual cycle (Jokubkiene et al., 2015). Interestingly, the luteal phase in humans is characterized by high levels of P4 which prepares the endometrium for embryo implantation during pregnancy, providing clues for the possible role of P4 in modulating endometrial folds (Mesen and Young, 2015). Based on our data using the *Pgr*^{cKO} where *Pgr* is deleted in the epithelium, P4 signaling is not required in the uterine epithelium for transverse folding. However, blocking P4 signaling in the entire uterus using RU486 leads to longitudinal folds, suggesting that P4 is required in non-epithelial uterine compartments for transverse folding. Our also suggests that P4-*Pgr* signaling non-cell autonomously regulate epithelial folding through signaling in surrounding tissue layers. It is possible that

P4 signaling in the stroma regulates transverse folding, since *Pgr* is strongly expressed in the sub-epithelial stroma on GD2 and GD3 (Tan et al., 1999). A conditional deletion model of *Pgr* in the stroma would

5.3.3 *Wnt5a* gradient regulated by P4 is essential for folding

Our data shows that both high and low levels of P4 signaling alters *Wnt5a* expression pattern. While high dose P4 leads to an increase in levels as well an expansion in *Wnt5a* gradient, folding pattern remains unaffected as the uteri continue to form transverse folds. On the other hand, why blocking P4 signaling using RU486 has two contrasting effects on *Wnt5a* expression in the two different backgrounds of mice is puzzling. One possible explanation is that RU486 may be acting as an agonist instead of an antagonist. It has been shown that RU486 acquires agonist properties in the presence of c-AMP (Beck et al., 1993). Although it is uncertain how P4 upregulates or downregulates *Wnt5a* levels, it is certain that altering levels of P4 signaling affect the gradient of Wnt5a expression.

In summary, we show that both E2 and P4 signaling regulate uterine folding. Low levels of P4 signaling lead to longitudinal folds by disrupting Wnt5a expression gradient. On the other high levels of E2 signaling also lead to longitudinal folds.

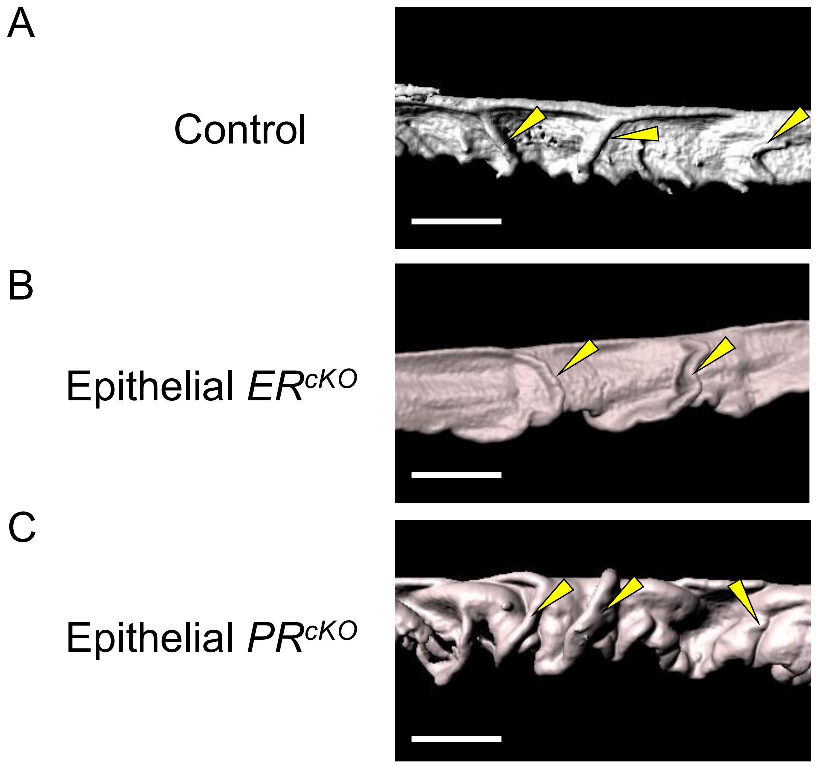

Figure 5.1: E2 and P4 signaling in the uterine epithelium are dispensable for transverse folding.

(A-C) 3D reconstruction of uterine lumen in control (*Pgr*$^{flox/flox}$) (n=5 mice) (A), *Esr*^{cKO} (*Ltf*$^{cre/+}$ *Esr*$^{flox/flox}$) (n=4 mice) (B), and *PR*^{cKO} (*Ltf*$^{cre/+}$ *Pgr*$^{flox/flox}$) (n=3 mice) (C) at IIRs on GD4 1200 h. Yellow arrowheads indicate transverse folds. Red arrowheads indicate longitudinal folds. Scale bars: 500 µm.

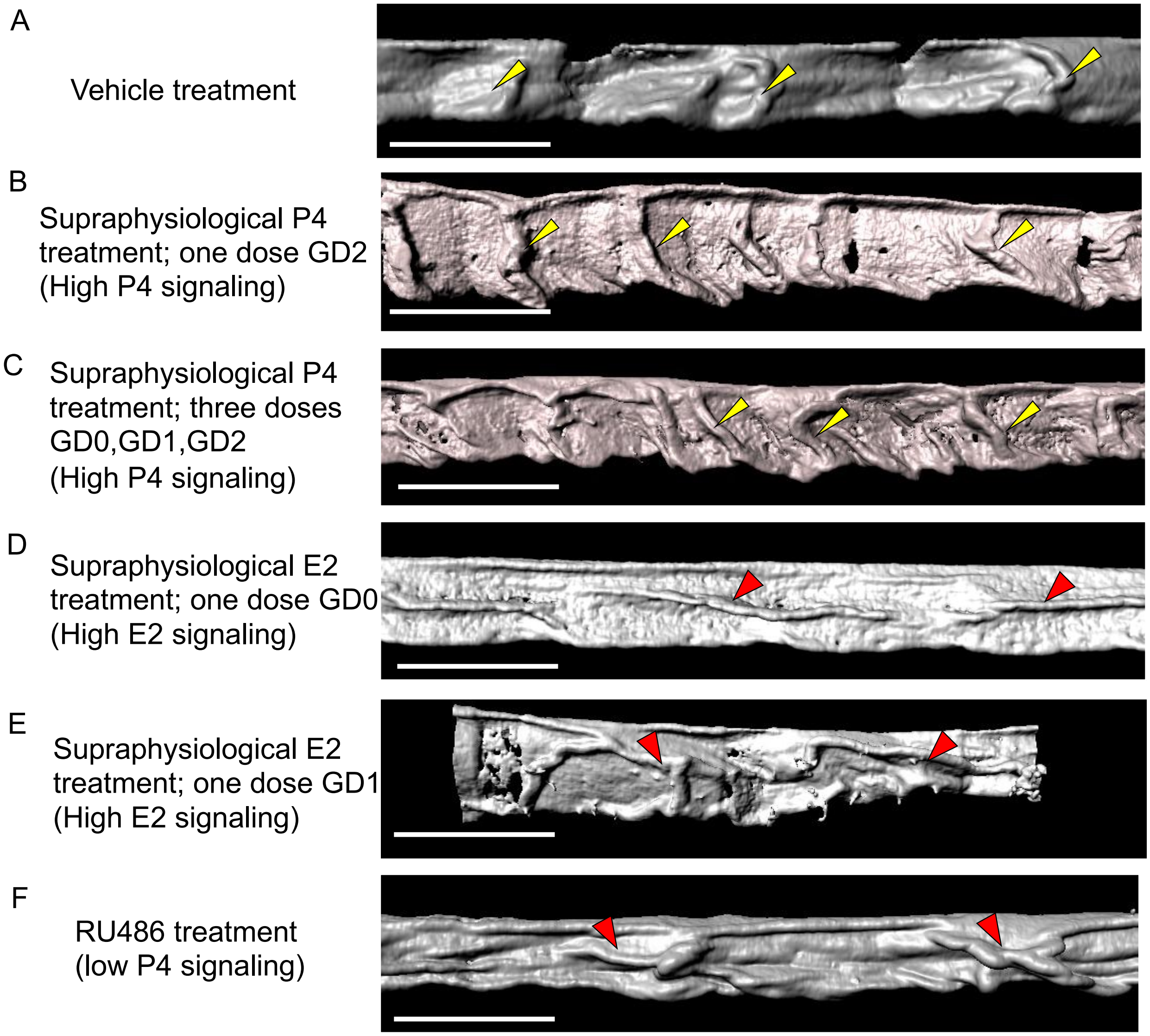

Figure 5.2: Increased E2 and reduced P4 signaling in all uterine compartments leads to disrupted folding.

(A-D) 3D reconstruction of uterine lumen at GD3 1200 h in mice treated with vehicle (one dose on GD2 1800 h; n=4 mice) (A), high P4 (one dose on GD2 1800 h; 4mg/mouse; n=3 mice) (B), high P4 (three doses, one each on GD0, GD1 and GD2 1200 h; 4mg/mouse; n=3 mice) (C), high E2 (one dose on GD0 1200 h; 200ng/mouse; n=3 mice) (D), high E2 (one dose on GD1 1200 h; 200ng/mouse; n=4 mice) (E) and RU486 (one dose on GD2 1800 h; 8mg/kg; n=4 mice) (F). Yellow arrowheads indicate transverse folds. Red arrowheads indicate longitudinal folds. Scale bars: 800 μm.

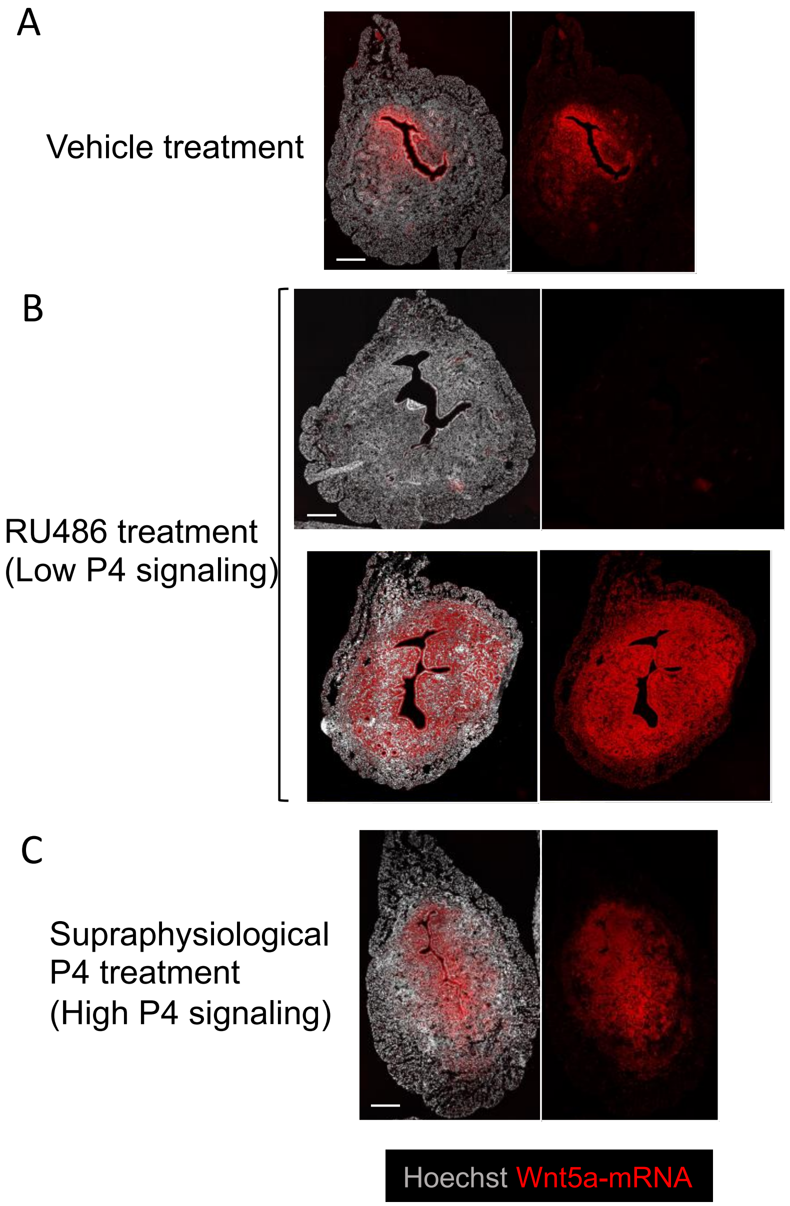

Figure 5.3: *Wnt5a* levels in the stroma are regulated by P4 signaling.
(A-C) Fluorescence in situ hybridization images showing expression of *Wnt5a* in vehicle treated mice (A), RU486 treated mice (8mg/kg) (n=3 mice for CD1; n=4 mice for C57BL/6) (B), and high P4 treated mice (4mg/mouse) (n=3 mice) (C). Scale bars: 200 µm.

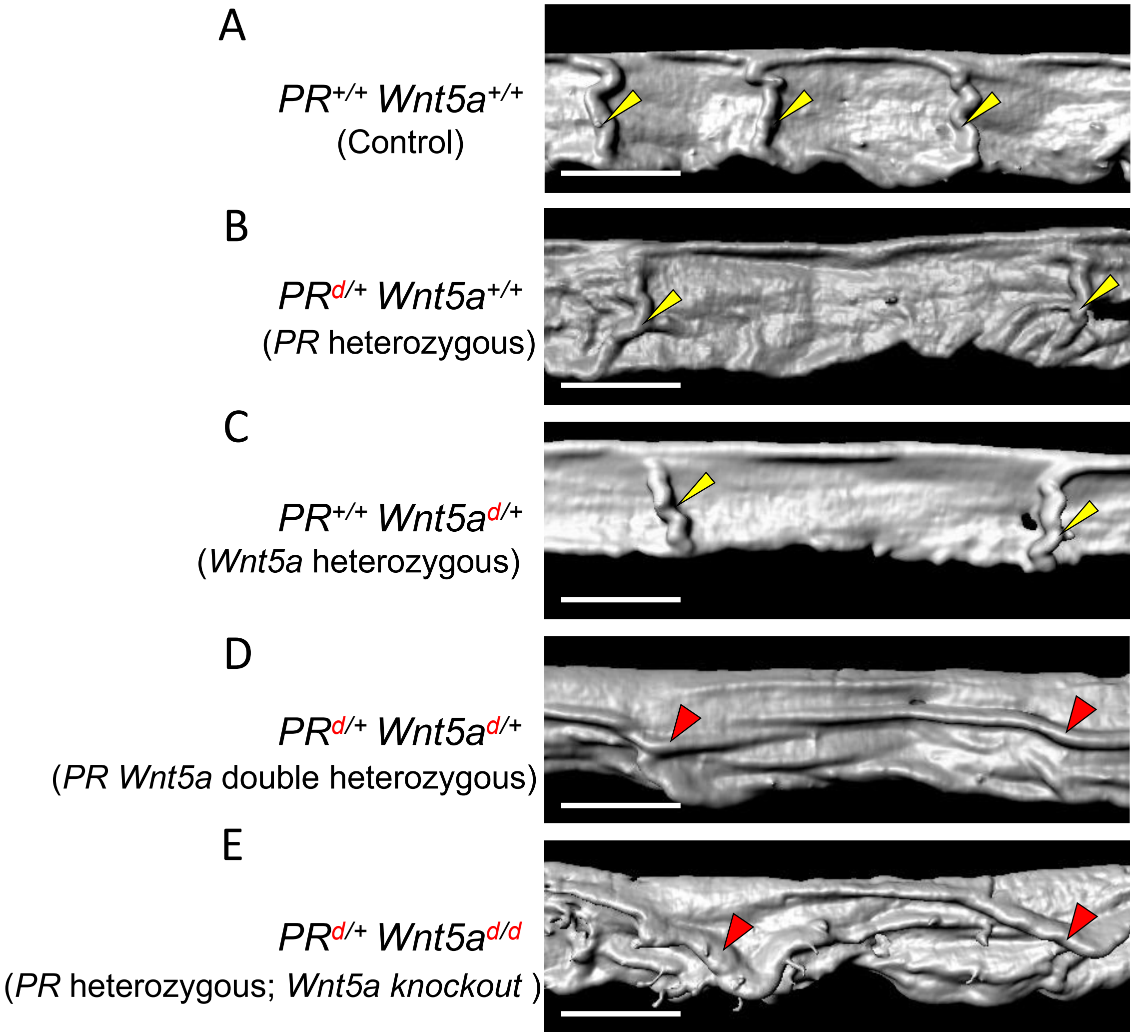

Figure 5.4: Interaction between P4 signaling and *Wnt5a* in the stroma for transverse folding.

(A-E) 3D reconstruction of uterine lumen in control (*Pgr*$^{+/+}$*Wnt5a*$^{+/+}$) (n=5 mice) (A), *Pgr* heterozygous mice (*Pgr*$^{d/+}$*Wnt5a*$^{+/+}$) (n=3 mice) (B), *Wnt5a* heterozygous mice (*Pgr*$^{+/+}$*Wnt5a*$^{d/+}$) (n=3 mice) (C), *Pgr*; *Wnt5a* double heterozygous mice (*Pgr*$^{d/+}$*Wnt5a*$^{d/+}$) (n=4 mice) (D) and *Pgr* heterozygous; *Wnt5a* knockout mice (*Pgr*$^{d/+}$*Wnt5a*$^{d/d}$). Yellow arrowheads indicate transverse folds. Red arrowheads indicate longitudinal folds. Scale bars: 800 µm.

Chapter 6: Clinical significance of uterine folds - effect of hyperstimulation on folding

6.1 Introduction

Defects in embryo implantation during early pregnancy is one of the leading causes of infertility around the world (Wilcox et al., 1988). As of 2020, around 8 million babies around the world have been conceived using assisted reproductive technologies (ARTs) (Evans et al., 2014; Fauser, 2019). In vitro fertilization (IVF) is being widely used in ARTs to improve the success of implantation and pregnancy. However, pregnancies following IVF are often associated with recurrent implantation failure (RIF), perinatal mortality, preterm delivery, preeclampsia and other complications (Bashiri et al., 2018; Hansen et al., 2002; Pandey et al., 2012). Hyperstimulation is an exogenous hormonal treatment done during IVF to increase the number of eggs retrieved, in order to increase the success rate of implantation. In addition, oocyte retrieval for IVF is a painful procedure and hence hyperstimulation ensures that multiple oocytes are obtained during a single retrieval procedure (Frederiksen et al., 2017). However, hyperstimulation is often associated with poor pregnancy rate and miscarriage (Check et al., 1999).

Menstrual cycle in humans consists of two phases: follicular or proliferative phase and luteal or secretory phase (Thiyagarajan et al., 2021). During follicular phase, Follicle stimulating hormone (FSH) causes maturation of ovarian follicles. Estrogen is the dominant hormone secreted by the maturing follicle and causes proliferation of the endometrium. At the end of the follicular phase, a surge in Luteinizing hormone (LH), triggers ovulation which leads to the release of an oocyte. This is followed by the luteal phase during which the corpus luteum formed from the mature follicle secretes progesterone which prepares the endometrium for implantation. Hyperstimulation is achieved using gonadotropins, typically gonadotropin-releasing hormone (GnRH) to mimic FSH and human chorionic gonadotropin (hCG) to mimic LH. Gonadotropins are administered in women to stimulate the ovarian follicles to produce multiple oocytes. However, hyperstimulation also results in supraphysiological levels of estradiol and progesterone. While estrogen levels are higher during the follicular phase, progesterone levels are 2-5 times higher as early as 1-2 days after hCG administration (Mirkin et al., 2004). High levels of serum estradiol on the day of hCG administration leads to reduced implantation rates and impaired receptivity (Simon et al., 1995).

Successful implantation in a natural cycle requires synchrony between embryo development and preparation of uterus for implantation. The window of receptivity (WOR) is defined as the time frame during which the uterus is receptive to embryo implantation. In women, the WOR is usually between 6-10 days after ovulation (Richter et al., 2006). However, the window of receptivity (WOR) in hyperstimulated patients is advanced by 1-2 days due to excess levels of hormones as evidenced by advancement of stromal proliferation and premature expression of estrogen receptor, progesterone receptor and pinopodes on the surface of luminal epithelium (Develioglu et al., 1999; Nikas et al., 1999).

The quality of the embryo obtained after hyperstimulation leads to low pregnancy rates and has been studied extensively. However, the effects of abnormal uterine environment on IVF success rates remains understudied. In IVF, there are two types of embryo transfers based on the timing of transfer: fresh embryo transfer and frozen embryo transfer (Evans et al., 2014). In fresh embryo transfer, embryos are transferred into the patient in the hyperstimulation cycle, usually 5 days after egg retrieval. The uterine environment in fresh embryo transfers is susceptible to the supraphysiological levels of hormones. In contrast, in frozen embryo transfer, the embryos are frozen after fertilization and are transferred 6-8 weeks later into the patient whose uterus is primed with controlled levels of hormones to mimic the natural cycle. Moreover, there is no difference in the quality and viability between frozen and fresh embryos (Pelkonen et al., 2010; Petracco et al., 2006). However, frozen embryo transfers are more successful than fresh embryo transfers suggesting that the lower pregnancy rate in the fresh embryo transfer is due to an abnormal uterine environment caused due to hyperstimulation (Chen et al., 2016; Maheshwari et al., 2012; Pelkonen et al., 2010; Roque et al., 2015).

In mice, hyperstimulation leads to delayed pre- and post-implantation embryonic development, increased resorption and fetal growth retardation (McLAREN and Michie, 1959; Van der Auwera and D'Hooghe, 2001). Evidence that hyperstimulation affects the uterine environment in mice comes from studies that show that transfer of healthy embryos into a hyperstimulated uterus leads to a higher mortality rate compared to transfer of healthy embryos into a control uterus (Ertzeid and Storeng, 1992; Ertzeid and Storeng, 2001; Van der Auwera and D'Hooghe, 2001). Several studies have shown that the uterine milieu in the hyperstimulated mice is abnormal due to supraphysiological levels of ovarian hormones. High levels of estrogen during hyperstimulation in mice leads to downregulation of genes involved in uterine fluid regulation such as *Aqp3*, *Aqp8* and *Scnn1b* leading to impaired receptivity (Xia et al., 2023). Hyperstimulation in mice affects gland volume and blood vessel remodeling during implantation (Qu et al., 2022). However, the effect of hyperstimulation on uterine folding has not been studied. In this chapter, we show that hyperstimulation causes longitudinal folds which in turn leads to disrupted embryo-uterine axes alignment and pregnancy loss. We also show that hyperstimulation leads to hyper-proliferation of the smooth muscle cells leading to increased muscle thickness.

6.2 Results

6.2.1 Hyperstimulation leads to subfertility

Firstly, we examined if hyperstimulation affects implantation and number of implantation sites using the traditional blue dye method. On GD4 1800 h, while controls have an average of 8 ± 2.16 (n=4, mean ± SD) blue dye implantation sites, hyperstimulated mice have a higher number of implantation sites averaging 13.8 ± 5.26 (n=5, mean ± SD) (Fig. 6.1A,C). Due to the high variation in the hyperstimulated mice, the average number of implantation sites are not statistically significant. To further asses the effect of hyperstimulation on embryo survival, we examined embryos during mid-gestation. On GD13, the average number of embryos (including resorption sites) is comparable in both controls (6.71 ± 3.4, n=5) and hyperstimulated mice (7.4 ± 1.9, n=7) (Fig. 6.1B,C). Surprisingly, the average number of embryos in hyperstimulated mice at GD13 is significantly lower compared to GD4 ($p<0.05$). This suggests that in hyperstimulated mice, some embryos that initiate implantation are lost post implantation and do not make it to placentation. Furthermore, when we examined embryo survival based on formation of healthy placenta, hyperstimulated mice have a significantly higher number of resorption sites (3 ± 1.73) compared to controls (0.14 ± 0.37) ($p<0.01$) (Fig. 6.1B,D). This suggests that hyperstimulation leads to mid-gestation embryo mortality and subfertility.

6.2.2 Hyperstimulation leads to aberrant pre-implantation longitudinal folds

To determine the effects of hyperstimulation on uterine folding, we examined uteri from controls and hyperstimulated mice during the per-implantation period. We induced hyperstimulation in C57BL/6 mice using 5IU PMSG and 5IU hCG. On GD3 1200 h, control uteri have transverse folds as previously shown (median=28.3°) (Fig. 6.2A). However, hyperstimulated mice have longitudinal folds (median=75.3°) (Fig. 6.2B) and are significantly different compared to controls (P<0.001, Mann-Whitney U test) (Fig. 6.2C). Further on GD4 1800 h, post implantation, 100% embryos in control uteri attach in flat peri-implantation regions (Fig. 6.1D). Moreover, control uteri have normal 'V' shaped chamber formation with embryos aligned along the M-AM axis (median angle=12.8°) (Fig. 6.2G). In contrast, 38% of embryos in hyperstimulated uteri are trapped in longitudinal folds retained at peri-implantation regions with abnormal chamber formation and disrupted E-U alignment (median angle=86.3°) (P<0.001) (Fig. 6.2E,G). The remaining 68% of the embryos in the hyperstimulated uteri that have escaped the longitudinal folds have normal chamber formation and E-U alignment comparable to controls (median angle=19.7°) (Fig. 6.2F,G).

6.2.3 Hyperstimulation causes increased proliferation in the smooth muscle layer

Epithelial proliferation is a crucial event that occurs during early pregnancy to prepare the uterus for implantation. Hence, we sought to examine whether hyperstimulation affects proliferation in the epithelium. Using EdU proliferation assay, we quantified the number of proliferating cells in the epithelium per volume of the uterine horn. Due to technical limitations, we combined the proliferating cells in the epithelium and stroma. On GD1

1200 h revealed that there is no significant difference in the number of proliferating cells in the epithelium between controls (median=1169.15 cells/mm^3) and hyperstimulated mice (median=1316.23 cells/mm^3) (Fig. 6.3A-C). Interestingly, the number of proliferating cells in the smooth muscle compartment of the hyperstimulated uteri (median=4416.06 cells/mm^3) is much higher compared to controls (median=2183.74cells/mm^3) ($p<0.05$) (Fig. 6.3A-C).

Further, we predicted that the increased proliferation in the smooth muscle compartment could lead to increased thickness of the smooth muscle layer. Hence, we examined the expression of Alpha Smooth Muscle Actin (ACTA2) in the two different muscle layers - longitudinal muscle (LM) and circular muscle (CM). We quantified and compared the volume of ACTA2 (normalized to volume of Hoechst) between the hyperstimulated uteri and controls in three different groups – LM, CSM and LM+CSM. On GD1 1200 h, there is no significant difference in the volume of ACTA2 in any of the three groups between the hyperstimulated uteri (LM^{median}=0.64, CM^{median}=0.46, LM+CM^{median}=1.10) and controls (LM^{median}=0.45, CM^{median}=0.43, LM+CM^{median}=0.89) (Fig. 6.4A,B). However, on GD3 1200 h, there is a significant difference in the volume of ACTA2 in all three groups between the hyperstimulated uteri (LM^{median}=0.62, CM^{median}=0.38, LM+CM^{median}=0.94) and controls (LM^{median}=0.34, CM^{median}=0.21, LM+CM^{median}=0.56) ($P<0.05$ for all groups) (Fig. 6.4C,D). These data show that excess proliferation due to hyperstimulation leads to increased thickness of the smooth muscle layer.

6.3 Discussion

Hyperstimulation has been shown to have detrimental effects on the uterus leading to impaired implantation and pregnancy complications. In this study, we examined the deleterious effects of hyperstimulation on uterine folding and its downstream effects on pregnancy outcomes. We observe that hyperstimulation causes aberrant longitudinal folds instead of transverse folds during implantation on GD3. Aberrant folding leads to trapping of embryos causing defective embryo-uterine axis alignment and chamber formation on GD4. Moreover, we see a correlation between the percentage of trapped embryos on GD4 and percentage of embryos that are resorbed mid-gestation on GD13. Furthermore, we show that hyperstimulated uteri have increased proliferation in the smooth muscle layer on GD1 leading to increased thickness of muscle layer on GD3 pointing to a close relationship between the smooth muscle layer and epithelial folding in the uterus.

6.3.1 Embryo mortality at mid-gestation in hyperstimulation condition is due to aberrant longitudinal folds

It is well known that hyperstimulation affects both the quality of the embryos and the uterine environment. The subfertility phenotype in hyperstimulated mice is partly due to poor embryo quality and partly due to defective uterine environment. Several studies have shown that, during hyperstimulation, both pre-implantation and post-implantation embryo quality is affected due to the elevated levels of E2 and P4. Inferior quality of oocytes/embryos obtained via hyperstimulation has been attributed to delayed maturation, slow metabolism and chromosomal abnormalities (Elbling and Colot, 1985; Ertzeid and Storeng, 1992; Lee et al., 2017). Previous studies have shown that in hyperstimulated mice, embryos die at different stages ranging from pre-implantation development until birth (BEAUMONT and SMITH, 1975; McLAREN and Michie, 1959). Beaumont and Smith showed that around 13%-18% of embryos die shortly after implantation while another 40% die at mid-gestation (BEAUMONT and SMITH, 1975). We also observe 2 kinds of embryo losses in hyperstimulated mice. In addition to the 38% embryo death at GD13, there is a 46% reduction in average number of embryos from GD4 to GD13. We speculate that the 40% embryo loss post implantation is due to poor quality of embryos while the 38% embryo death at mid-gestation is due defective uterine environment. Previously, when embryos obtained from both control and hyperstimulated mice were transferred into a control recipient, there was no difference in embryo mortality at mid-gestation or birth (Ertzeid and Storeng, 2001). This suggests that hyperstimulated embryos that make it to mid-gestation are comparable to control embryos in terms of viability. Hence embryo mortality at mid-gestation in hyperstimulated mice is likely due to impaired uterine environment. In the future, embryo transfer experiments are needed to verify our speculation.

6.3.2 Impact of hyper-proliferated smooth muscle layer on epithelial folding

As mentioned in chapter 1.3, smooth muscle compression in several structures including the airway and intestine regulate epithelial folding (Shyer et al., 2013; Veerati et al., 2020). In the chick gut, as the longitudinal muscle layer gets thicker, the folding pattern of the epithelium changes from zig-zag to villi (Shyer et al., 2013). In the mouse oviduct, differential increase in the length of the epithelium along the circumferential axis relative to the smooth muscle layer causes longitudinal folds (Koyama et al., 2016). On the other hand, as in the case of *Celsr1* mutants, differential increase in longitudinal length of the epithelium relative to the smooth muscle causes randomized folds with ectopic branches. Similar to the intestine and oviduct, the uterus is also a tubular organ consisting of a thick muscle layer surrounding the epithelium. Hence, it is likely that the smooth muscle layer in the uterus affects the folding dynamics of the epithelium. Our data show that muscle layer proliferates at a higher rate compared to hyperstimulated uteri have thicker muscle layer compared to controls. Hence, it is highly possible that the differential increase in thickness of muscle layer compared to the epithelium in the hyperstimulated uteri causes longitudinal folds. Future research is required to the delineate the intricate relationship between the muscle and epithelium for folding in the uterus. Gene expression analysis between hyperstimulated and control mice at single cell level can determine genes in the muscle and stroma that may contribute to aberrant folding.

6.3.3 Elevated levels of E2 during hyperstimulation disrupt folding pattern

It is well known that during hyperstimulation, both E2 and P4 levels are elevated due to exogenous hormone treatment (Qu et al., 2022; Simon et al., 1995). However, in chapter 5, we show that high levels of E2 signaling disrupts the uterine folding pattern while high levels of P4 do not affect folding. Hence, our data suggests that the aberrant folding pattern in the hyperstimulated mice is most likely due to the supraphysiological levels of E2 and not P4. In addition, we also show that the muscle layer in the hyperstimulated mice is hyper-proliferated on GD1, at a time when E2 levels are usually high. While our data provides leads for possible pathways that are dysregulated in the hyperstimulated mice, future investigation is required to delineate the detailed genetic pathways that contribute to aberrant folding. A comparison of the gene expression analysis between high dose E2 treated mice and hyperstimulated mice would reveal the differentially regulated genes that are common in both the treatment groups. Further, it would be interesting to see if treating the hyperstimulated mice with a pharmacological inhibitor of E2 signaling can rescue the aberrant folding phenotype.

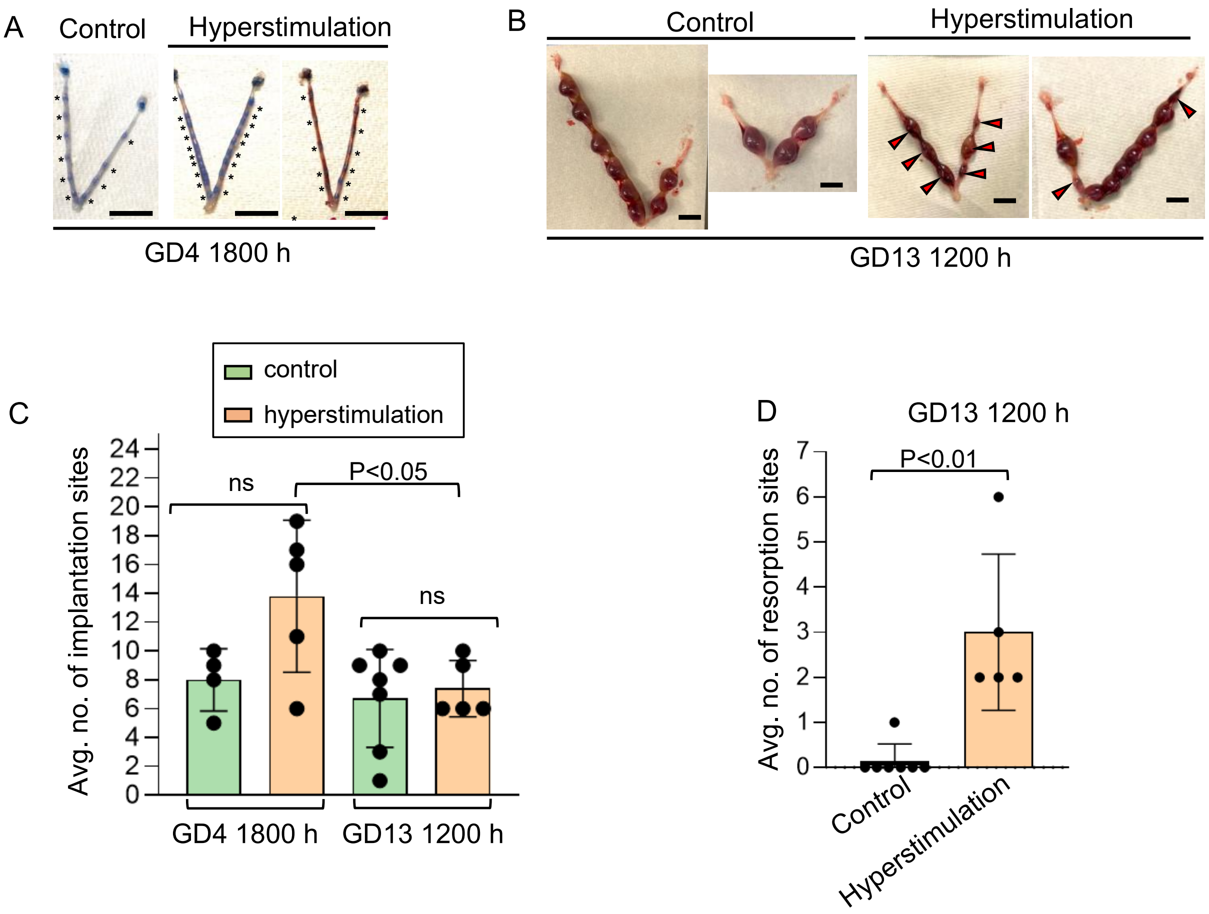

Figure 6.1: Hyperstimulation leads to compromised pregnancy.
(A) Implantation sites (blue bands) as observed using blue dye method in control (n=4) and hyperstimulation (n=5) mice on GD4 1800 h. Asterisk indicates blue bands at implantation sites. (B) Uterine horns with embryos on GD13 1200 h in control (n=7) and hyperstimulation (n=5) mice. Red arrows indicate resorption sites. (C) Average number of implantation sites on GD4 1800 h (blue bands) and GD13 1200 h (decidual balls containing embryos) in control and hyperstimulation mice. (*P*<0.05, Mann–Whitney *U*-test). (D) Average number of resorption sites on GD13 1200 h in control and hyperstimulation mice. (*P*<0.01, Mann–Whitney *U*-test).

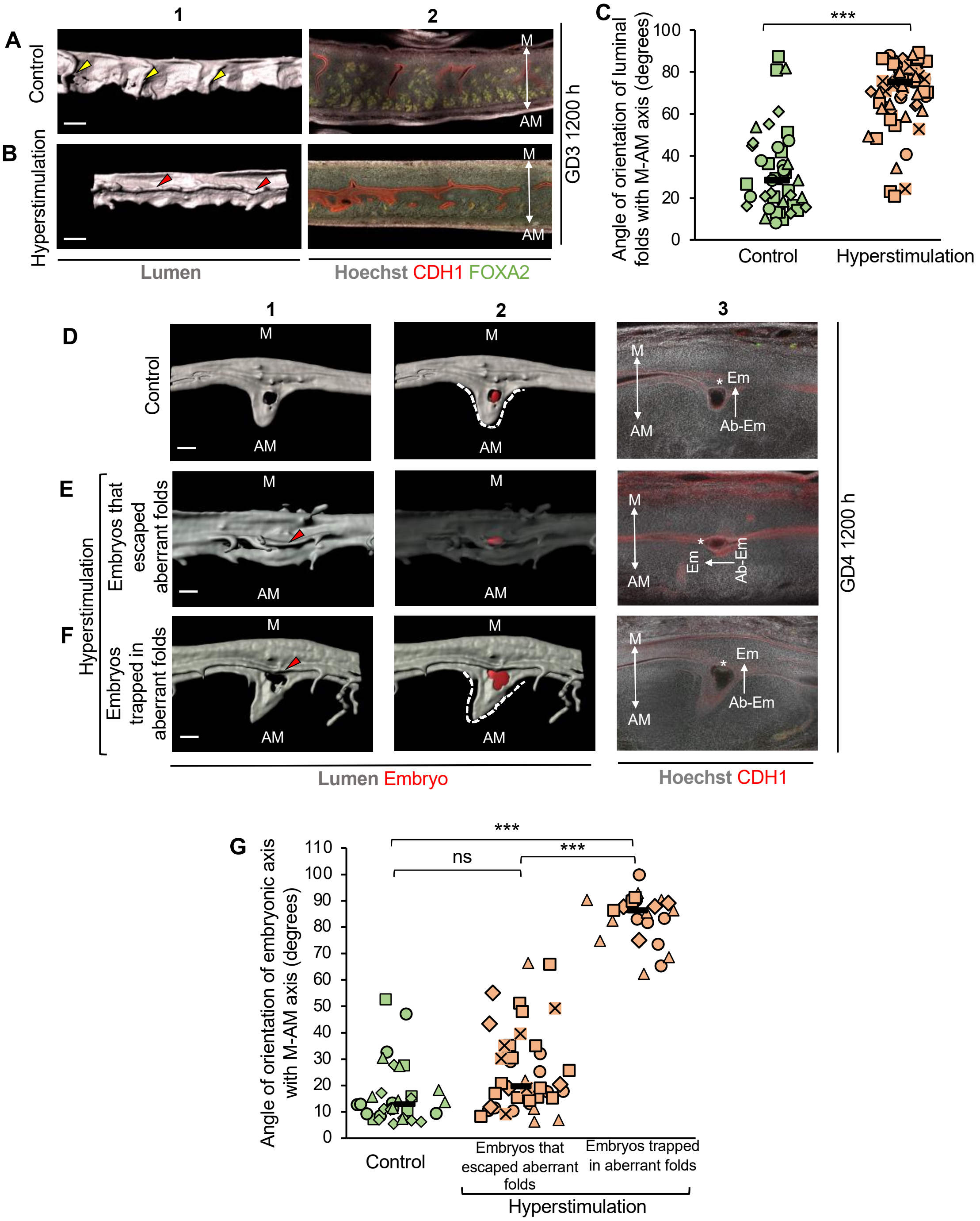

Figure 6.2: Hyperstimulation leads to aberrant pre-implantation folding and disrupted post-implantation embryo-uterine axes alignment and chamber formation.

Figure 6.2 (cont'd)
(A,B) 3D reconstruction of lumen in control (A) and hyperstimulation (B) uteri at GD3 1200 h. Yellow arrowheads indicate transverse folds. Red arrowheads indicate longitudinal folds. Blue arrowheads indicate embryos (red surface). Scale bars: 300 µm. (C) Quantification of fold angle with M-AM axis in control and hyperstimulation (n=4 mice/group) uteri on GD3 1200 h (***P<0.001, Mann–Whitney U-test). (D-F) 3D surface view and optical slice view of implantation sites at GD4 1800 h in control (D) and $Wnt5a^{cKO}$ (E,F) uteri. Implantation sites in $Wnt5a^{cKO}$ uteri where embryos have escaped folds (E) or where embryos are trapped in folds (F). Panel 1: 3D lumen surface (gray). Panel 2: transparent 3D lumen and embryo (red) surface. Panel 3: optical slice with frontal view. Scale bars: 100 µm. (G) Quantification of embryo orientation with respect to M-AM axis in control (n=4 mice, n_e=32 embryos) and hyperstimulation (n=5 mice, n_e=65 embryos) uteri at GD4 1800 h. (***P<0.001, Kruskal–Wallis test, Dunn's multiple comparison). ns, non-significant. M, mesometrial pole; AM, anti-mesometrial pole; Em, embryonic pole; Ab-Em, abembryonic pole. Black dashes indicate the median angle. Asterisks in D-F indicate inner cell mass.

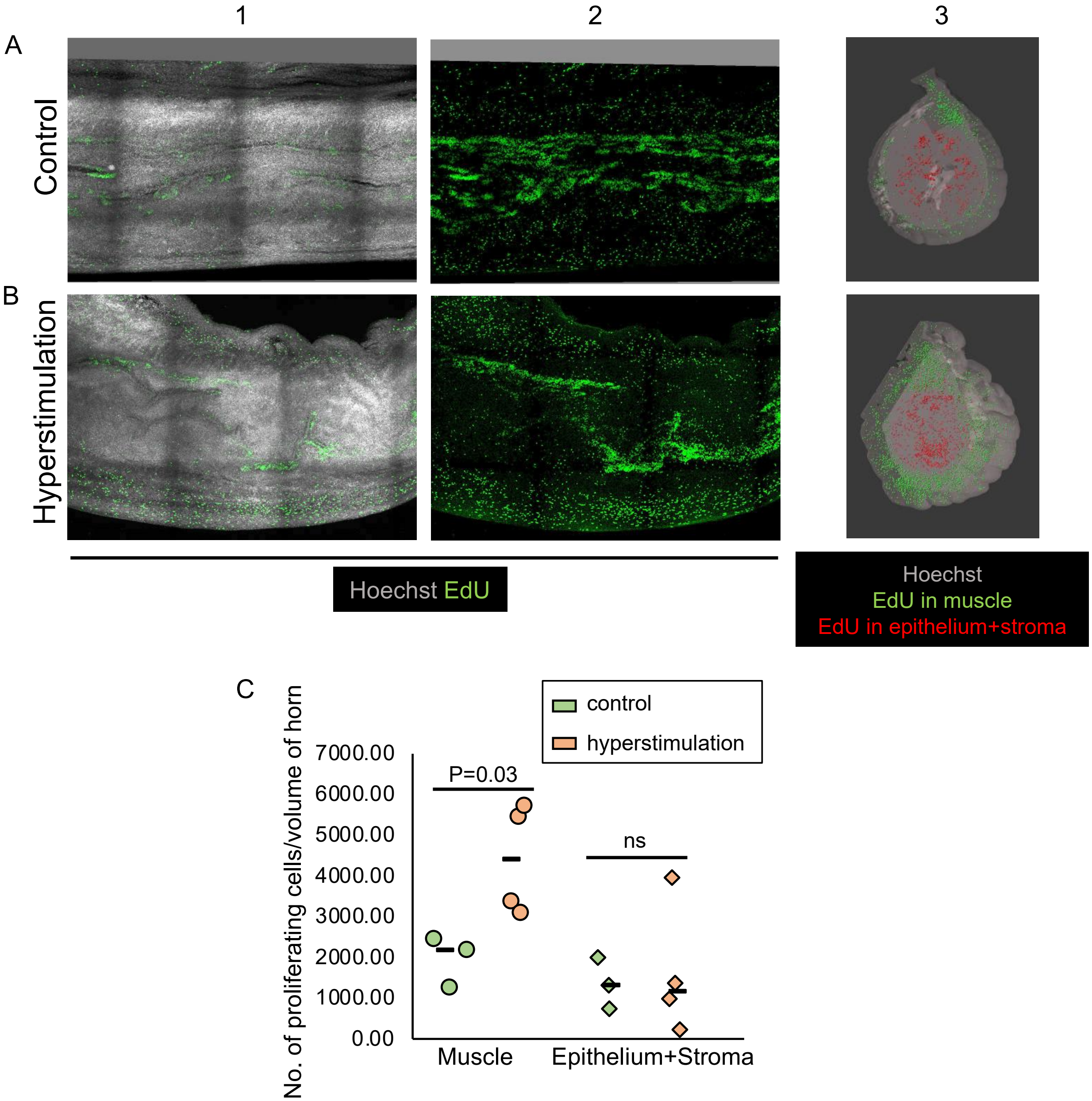

Figure 6.3: Hyperstimulation leads to increased proliferation in muscle layer. (A,B) EdU staining in control (A) and hyperstimulated (B) mice. Panel 1 and 2 shows optical slice view with Hoechst (in grey) and EdU (in green). Panel 3 shows cross-sectional 3D surface view with EdU in epithelium and stroma indicated by red surfaces and EdU in muscle indicated by green surfaces. (C) Quantification of EdU (number of proliferating cells) in control and hyperstimulation mice. (P<0.05, Mann-Whitney U-test).

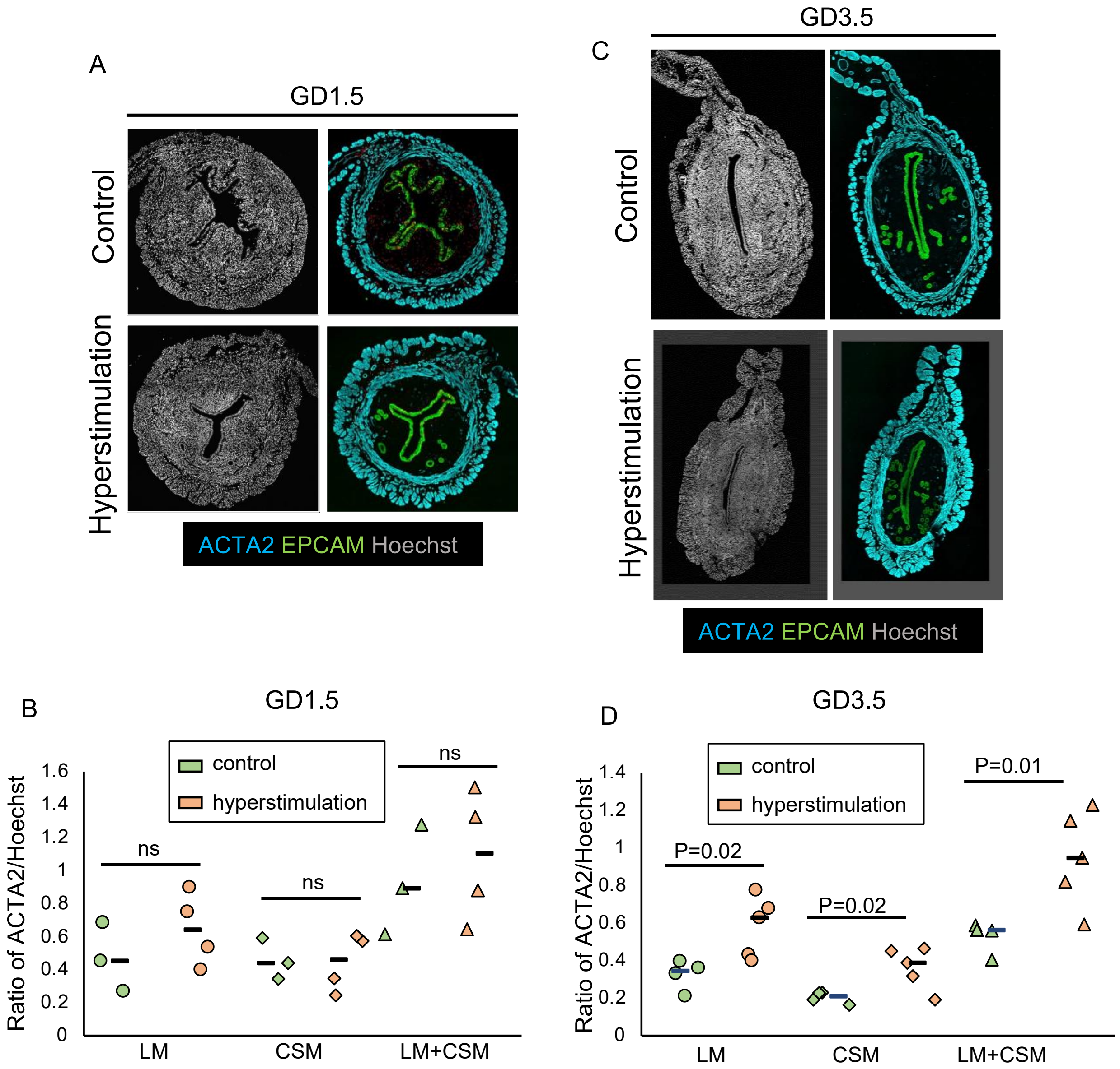

Figure 6.4: Hyper-proliferation in muscle leads to increased muscle thickness in hyperstimulated uteri.

(A,B) Expression of ACTA2 in histological sections of control and hyperstimulated uteri on GD1 1200 h (A) and GD3 1800 h (B) using immunofluorescence staining. (C,D) Quantification of ACTA2 expression in controls and hyperstimulated mice on GD1 1200 h (C) and GD3 1800 h (D). (P-values, Mann-Whitney U-test). LM – longitudinal muscle; CSM – circular muscle.

Chapter 7: Conclusion and future perspectives

Our study delineates how the 3D structure of the uterine lumen during early pregnancy is crucial to embryo implantation, chamber formation, E-U alignment and embryo morphogenesis (Fig. 7.1). Our study shows that: (1) the randomly folded uterine lumen organizes into longitudinal folds during unidirectional embryo movement and later into transverse folds during embryo spacing prior to implantation; (2) transverse folds are resolved to form flat peri-implantation regions; (3) peri-implantation regions are pre-established by luminal patterning, prior to completion of embryo spacing; (4) luminal folds (or 2D crypts) and implantation chambers are distinct structures; (5) chamber formation facilitates E-U alignment; (6) aberrant longitudinal folds trap embryos, leading to E-U misalignment and abnormal chamber formation; and (7) mis-alignment of embryos leads to abnormal buffer space between epiblast and maternal tissue, likely contributing to poor embryo growth later in pregnancy. Further, we show that reduced P4 signaling leads to longitudinal folds by modulating Wnt5a gradient. We also show that high levels of E2 signaling leads to longitudinal folds, and we validate our findings in a clinically relevant hyperstimulation model where E2 levels are high. We show that hyperstimulation leads to longitudinal folds which in turn lead to downstream defects ultimately leading to compromised pregnancy.

7.1 Future perspectives

Transcriptomic analysis: While a few genes including Wnt5a, Rbpj and Msx1/2 affect folding in the mouse uterus, the other signaling pathways involved in transverse folding remain largely unknown. Since our data shows that folding changes from random pattern on GD2 1200 h to transverse pattern on GD3 1200 h, single cell RNA sequencing of the entire uterus at these two time points can identify differentially expressed genes in the different cell populations of the uterus. Single cell RNA sequencing can also be used to identify targets that are dysregulated in the hyperstimulation condition. Furthermore, prediction algorithms can be used to delineate cell-cell communications, ligand-receptor interactions and entire transcriptional cascades that regulate transverse folding.

Since we observe that embryos always attach at the center of pre-formed peri-implantation regions, spatial transcriptomics can be employed to identify gene expression patterns at specific locations within peri-implantation regions.

Recreating uterine folds in vitro using tissue engineering: Several studies have used innovative tissue engineering approaches to identify the mechanisms involved in epithelial fold formation in other structures. For example, using recent advances in organoid culture and 3D bioprinting, intestinal crypts/folds have been recreated in vitro using intestinal epithelial organoid culture and embedding epithelial cells in hydrogels (Antfolk and Jensen, 2020; Sato et al., 2011). Similarly, uterine epithelial folds can be recreated in vitro and can be co-cultured with embryos to understand how folds impact implantation. Moreover, such in vitro conditions are also more amenable to live imaging studies which are not possible in native uteri due to technical limitations.

Computational modeling: Our understanding of uterine folding is limited partly due to challenges in deciphering the genetic, biochemical and mechanical interactions across multiple levels of tissue organization. Computational models based on our experimental data can be used as powerful means to understand multiscale interactions that facilitate folding. These models can take into account the parameters of the uterine structure from our 3D reconstructions and can simulate folding under different conditions. For example, our preliminary results point to the role of smooth muscle thickness in regulating folding pattern. Simulations of folding pattern can be generated by varying the smooth muscle thickness, luminal diameter and stromal compartment stiffness.

Human studies - SIH: Using SIH, endometrial folds were detected in approximately 50% of women in the secretory phase of menstrual cycle (Jokubkiene et al., 2015). However, it is possible that folds may exist in other phases of menstrual cycle. Moreover, folds may be detected depending on the plane of view. Hence, more studies need to be conducted in different phases of the menstrual cycle and hysterograms need to be captured at different planes. Such information can be useful in diagnosing pathological conditions that may impact pregnancy.

Genome wide association studies (GWAS): While mutations in genes such as *Wnt5a* and *Rbpj* disrupt uterine folding, whether these genes affect folding in humans is yet to be discovered. Although studies on uterine folding are limited, there have been several studies that have identified gene variants in patients with recurrent pregnancy loss. GWAS is used to identify gene variants across individuals that are associated with a disease phenotype (Uffelmann et al., 2021). Since our data from mouse studies shows a correlation between aberrant uterine folding and pregnancy loss, the GWAS catalog can be analyzed to determine possible association between these gene targets and recurrent pregnancy loss. Similarly, other targets identified using single cell RNA sequencing analysis can also be validated using the GWAS catalog. In the future, GWAS studies can be performed to identify genetic mutations in cohorts of patients that display abnormalities in uterine folding based on SIH studies.

7.2 Conclusion

Broadly, our research sheds light on the importance of uterine folding pattern in implantation and pregnancy. We show that pre-implantation transverse folds along M-AM axis are essential for flat PIR formation, chamber formation and E-U alignment. Using two different mouse models that disrupt two independent signaling pathways, we show that a common phenotype of aberrant longitudinal folds disrupts chamber formation and E-U alignment, leading to compromised pregnancy outcomes. We also show how hormones impact uterine folding pattern and provide evidence for translational relevance of our findings. Further studies with mouse models that display disrupted uterine folding pattern can lead to a better understanding of the role of endometrial folds in pregnant women. Recurrent pregnancy loss is a prevalent disorder that affects pregnancy outcomes in women, but about 33% of the losses remain unexplained (Ford and Schust, 2009). Moreover, pregnancy losses during ARTs also remain undiagnosed. In the future, research on uterine structure and folding can provide insights for diagnosis and treatment of unexplained pregnancy losses.

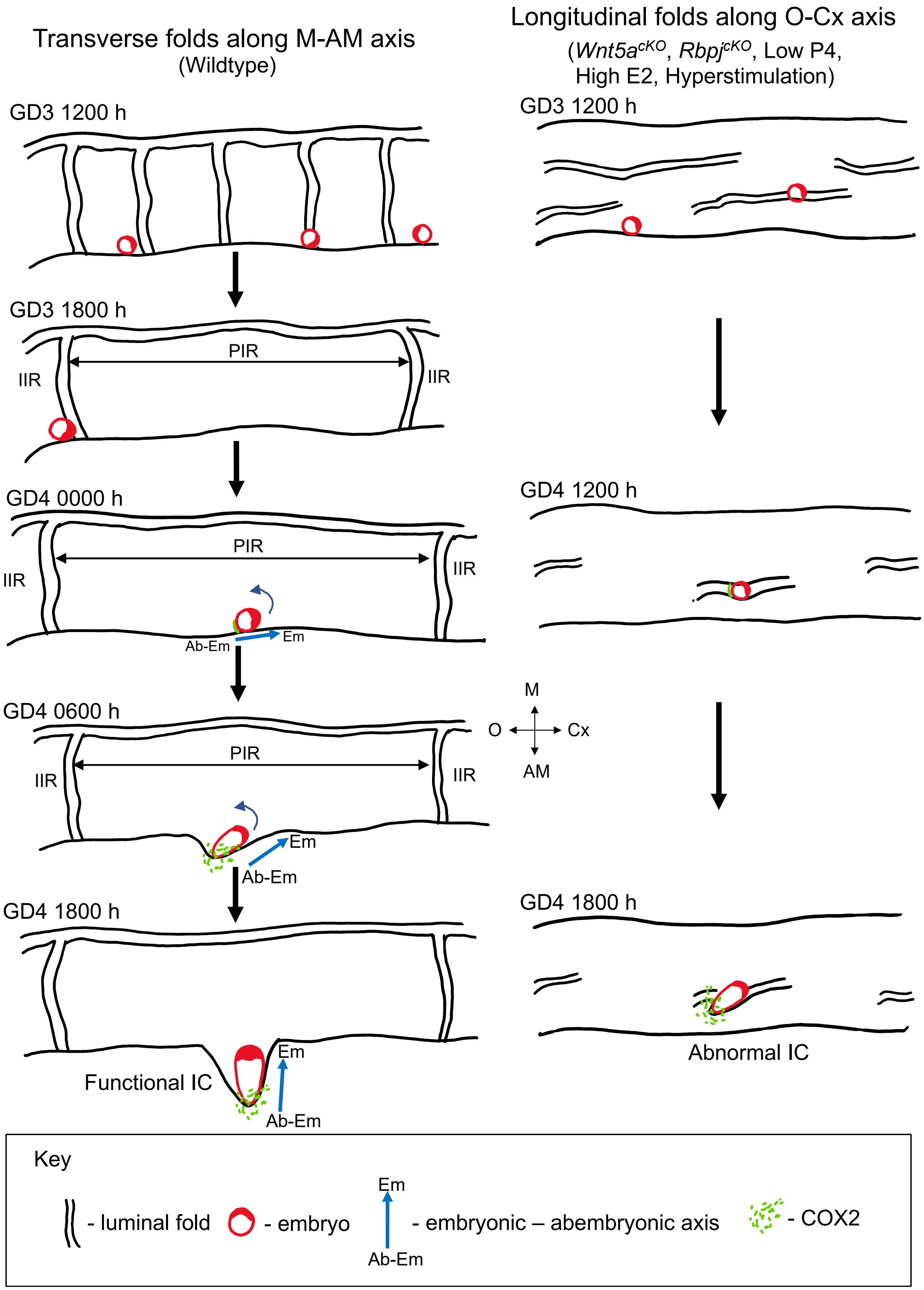

Figure 7.1: Schematic showing the effect of uterine luminal folding pattern on embryo implantation, orientation and chamber formation.

Figure 7.1 (cont'd)
(A) During mouse pregnancy, uterine lumen displays transverse folds along the M-AM axis at GD3 1200 h. These folds resolve in some regions to form flat PIRs at GD3 1800 h. PIRs are formed before the arrival of the embryo at the implantation site. Embryos arrive in the middle of the PIR, with their Em-AbEm axis perpendicular to the uterine M-AM axis at GD4 0000 h. Embryo attachment to the uterine luminal epithelium initiates at the mural trophectoderm of the embryo. Embryo orientation along the M-AM axis takes place as the implantation chamber forms and elongates towards the AM pole. (B) In models with aberrant uterine folding (*Wnt5a*^{cKO}, *Rbpj*^{cKO}, Low P4 signaling, High E2 signaling, Hyperstimulation), longitudinal folds aligned with the O-Cx axis are observed at GD3 1200 h. Folds along the O-Cx axis fail to resolve to form flat PIRs, resulting in embryos becoming trapped at GD4 1200 h. Embryos trapped in longitudinal folds display defective chamber formation and disrupted alignment of the embryo-uterine axes at GD4 1800 h. M, mesometrial pole; AM, anti-mesometrial pole; O, ovary; Cx, cervix; Em, embryonic pole; Ab-Em, abembryonic pole; IC, implantation chamber; IS, implantation site; PIR, peri-implantation region; IIR, inter-implantation region.

REFERENCES

Abd-Elkareem, M. (2017). Morphological, histological and immunohistochemical study of the rabbit uterus during pseudopregnancy. *J Cytol Histol* **8**.

Agarwala, R., Shah, J. and Dutta, U. (2018). Thickened gastric folds: Approach. *Journal of Digestive Endoscopy* **9**, 149-154.

Akinloye, A. and Oke, B. (2015). Histology and ultrastructure of the uterus of African giant rat (Cricetomys Gambianus, Waterhouse) during oestrous cycle. *Folia Morphologica* **74**, 311-317.

Antfolk, M. and Jensen, K. B. (2020). A bioengineering perspective on modelling the intestinal epithelial physiology in vitro. *Nature Communications* **11**, 6244.

Aplin, J. D. and Ruane, P. T. (2017). Embryo–epithelium interactions during implantation at a glance. *Journal of cell science* **130**, 15-22.

Arman, E., Haffner-Krausz, R., Chen, Y., Heath, J. K. and Lonai, P. (1998). Targeted disruption of fibroblast growth factor (FGF) receptor 2 suggests a role for FGF signaling in pregastrulation mammalian development. *Proceedings of the National Academy of Sciences* **95**, 5082-5087.

Arora, R., Fries, A., Oelerich, K., Marchuk, K., Sabeur, K., Giudice, L. C. and Laird, D. J. (2016). Insights from imaging the implanting embryo and the uterine environment in three-dimensions. *Development*, dev. 144386.

Barrau, M. D., Abel Jr, J. H., Torbit, C. and Tietz Jr, W. (1975). Development of the implantation chamber in the pregnant bitch. *American Journal of Anatomy* **143**, 115-129.

Bashiri, A., Halper, K. I. and Orvieto, R. (2018). Recurrent Implantation Failure-update overview on etiology, diagnosis, treatment and future directions. *Reproductive Biology and Endocrinology* **16**, 1-18.

BEAUMONT, H. M. and SMITH, A. F. (1975). Embryonic mortality during the pre-and post-implantation periods of pregnancy in mature mice after superovulation. *Reproduction* **45**, 437-448.

Beck, C. A., Weigel, N. L., Moyer, M. L., Nordeen, S. K. and Edwards, D. P. (1993). The progesterone antagonist RU486 acquires agonist activity upon stimulation of cAMP signaling pathways. *Proceedings of the National Academy of Sciences* **90**, 4441-4445.

Benjaminov, O. and Atri, M. (2004). Sonography of the abnormal fallopian tube. *American Journal of Roentgenology* **183**, 737-742.

Bogdanović, O., Delfino-Machín, M., Nicolás-Pérez, M., Gavilán, M. P., Gago-Rodrigues, I., Fernández-Miñán, A., Lillo, C., Ríos, R. M., Wittbrodt, J. and Martínez-Morales, J. R. (2012). Numb/Numbl-Opo antagonism controls retinal epithelium morphogenesis by regulating integrin endocytosis. *Developmental cell* **23**, 782-795.

Borrell, V. (2018). How cells fold the cerebral cortex. *Journal of Neuroscience* **38**, 776-783.

Botto, L. D., Moore, C. A., Khoury, M. J. and Erickson, J. D. (1999). Neural-tube defects. *New England journal of medicine* **341**, 1509-1519.

Branchfield, K., Li, R., Lungova, V., Verheyden, J. M., McCulley, D. and Sun, X. (2016). A three-dimensional study of alveologenesis in mouse lung. *Developmental biology* **409**, 429-441.

Cha, J., Bartos, A., Park, C., Sun, X., Li, Y., Cha, S.-W., Ajima, R., Ho, H.-Y. H., Yamaguchi, T. P. and Dey, S. K. (2014). Appropriate crypt formation in the uterus for embryo homing and implantation requires Wnt5a-ROR signaling. *Cell reports* **8**, 382-392.

Chanet, S. and Martin, A. C. (2014). Mechanical force sensing in tissues. *Progress in molecular biology and translational science* **126**, 317-352.

Check, J. H., Choe, J. K., Katsoff, D., Summers-Chase, D. and Wilson, C. (1999). Controlled ovarian hyperstimulation adversely affects implantation following in vitro fertilization–embryo transfer. *Journal of assisted reproduction and genetics* **16**, 416-420.

Chen, Z.-J., Shi, Y., Sun, Y., Zhang, B., Liang, X., Cao, Y., Yang, J., Liu, J., Wei, D. and Weng, N. (2016). Fresh versus frozen embryos for infertility in the polycystic ovary syndrome. *N engl j med* **375**, 523-533.

Chi, R.-p. A., Wang, T., Adams, N., Wu, S.-p., Young, S. L., Spencer, T. E. and DeMayo, F. (2019). Transcriptional and Progesterone Receptor Binding Profiles of the Human Endometrium Reveal Important Pathways and Regulators in the Epithelium During the Window of Implantation. *bioRxiv*, 680181.

Curtis Hewitt, S., Goulding, E. H., Eddy, E. and Korach, K. S. (2002). Studies using the estrogen receptor α knockout uterus demonstrate that implantation but not decidualization-associated signaling is estrogen dependent. *Biology of reproduction* **67**, 1268-1277.

Daikoku, T., Cha, J., Sun, X., Tranguch, S., Xie, H., Fujita, T., Hirota, Y., Lydon, J., DeMayo, F. and Maxson, R. (2011). Conditional deletion of Msx homeobox genes in the uterus inhibits blastocyst implantation by altering uterine receptivity. *Developmental cell* **21**, 1014-1025.

Daikoku, T., Ogawa, Y., Terakawa, J., Ogawa, A., DeFalco, T. and Dey, S. K. (2014). Lactoferrin-iCre: a new mouse line to study uterine epithelial gene function. *Endocrinology* **155**, 2718-2724.

Develioglu, O. H., Hsiu, J.-G., Nikas, G., Toner, J. P., Oehninger, S. and Jones Jr, H. W. (1999). Endometrial estrogen and progesterone receptor and pinopode expression in stimulated cycles of oocyte donors. *Fertility and Sterility* **71**, 1040-1047.

Elbling, L. and Colot, M. (1985). Abnormal development and transport and increased sister-chromatid exchange in preimplantation embryos following superovulation in mice. *Mutation Research/Environmental Mutagenesis and Related Subjects* **147**, 189-195.

Enciso, M., Aizpurua, J., Rodríguez-Estrada, B., Jurado, I., Ferrández-Rives, M., Rodríguez, E., Pérez-Larrea, E., Climent, A., Marron, K. and Sarasa, J. (2021). The precise determination of the window of implantation significantly improves ART outcomes. *Scientific reports* **11**, 1-8.

Enders, A. and Liu, I. (1991). Lodgement of the equine blastocyst in the uterus from fixation through endometrial cup formation. *Journal of reproduction and fertility. Supplement* **44**, 427-438.

Enders, A. C. (1975). The implantation chamber, blastocyst and blastocyst imprint of the rat: A scanning electron microscope study. *The Anatomical Record* **182**, 137-149.

Ertzeid, G. and Storeng, R. (1992). Adverse effects of gonadotrophin treatment on pre- and postimplantation development in mice. *Reproduction* **96**, 649-655.

---- (2001). The impact of ovarian stimulation on implantation and fetal development in mice. *Human reproduction* **16**, 221-225.

Evans, J., Hannan, N. J., Edgell, T. A., Vollenhoven, B. J., Lutjen, P. J., Osianlis, T., Salamonsen, L. A. and Rombauts, L. J. (2014). Fresh versus frozen embryo transfer: backing clinical decisions with scientific and clinical evidence. *Human reproduction update* **20**, 808-821.

Fauser, B. C. (2019). Towards the global coverage of a unified registry of IVF outcomes. *Reproductive biomedicine online* **38**, 133-137.

Fissore, R., Edmondson, A., Pashen, R. and Bondurant, R. (1986). The use of ultrasonography for the study of the bovine reproductive tract. II. Non-pregnant, pregnant and pathological conditions of the uterus. *Animal Reproduction Science* **12**, 167-177.

Flores, D., Madhavan, M., Wright, S. and Arora, R. (2020). Mechanical and signaling mechanisms that guide pre-implantation embryo movement. *Development* **147**, dev193490.

Ford, H. B. and Schust, D. J. (2009). Recurrent pregnancy loss: etiology, diagnosis, and therapy. *Reviews in obstetrics and gynecology* **2**, 76.

Franco, H. L., Rubel, C. A., Large, M. J., Wetendorf, M., Fernandez-Valdivia, R., Jeong, J.-W., Spencer, T. E., Behringer, R. R., Lydon, J. P. and DeMayo, F. J. (2012). Epithelial progesterone receptor exhibits pleiotropic roles in uterine development and function. *The FASEB Journal* **26**, 1218-1227.

Frederiksen, Y., Mehlsen, M. Y., Matthiesen, S. M., Zachariae, R. and Ingerslev, H. J. (2017). Predictors of pain during oocyte retrieval. *Journal of Psychosomatic Obstetrics & Gynecology* **38**, 21-29.

Ginther, O. (1983). Fixation and orientation of the early equine conceptus. *Theriogenology* **19**, 613-623.

---- (1985). Dynamic physical interactions between the equine embryo and uterus. *Equine Veterinary Journal* **17**, 41-47.

---- (1998). Equine pregnancy: physical interactions between the uterus and conceptus. In *Proc Am Assoc Equine Pract*, pp. 73-104: Citeseer.

Ginther, O. and Pierson, R. (1984). Ultrasonic anatomy and pathology of the equine uterus. *Theriogenology* **21**, 505-516.

Goldstein, S. R. (1994). Use of ultrasonohysterography for triage of perimenopausal patients with unexplained uterine bleeding. *American journal of obstetrics and gynecology* **170**, 565-570.

---- (2010). Modern evaluation of the endometrium. *Obstetrics & Gynecology* **116**, 168-176.

Goulet, O., Ruemmele, F., Lacaille, F. and Colomb, V. (2004). Irreversible intestinal failure. *Journal of pediatric gastroenterology and nutrition* **38**, 250-269.

Gu, Y., Forostyan, T., Sabbadini, R. and Rosenblatt, J. (2011). Epithelial cell extrusion requires the sphingosine-1-phosphate receptor 2 pathway. *Journal of Cell Biology* **193**, 667-676.

Gutzman, J. H., Graeden, E. G., Lowery, L. A., Holley, H. S. and Sive, H. (2008). Formation of the zebrafish midbrain–hindbrain boundary constriction requires laminin-dependent basal constriction. *Mechanisms of development* **125**, 974-983.

Hagstrom, D. J. (2003). The Breeding Soundness Exam. *Universty of Illions Extension*, s1-8.

Haigo, S. L., Hildebrand, J. D., Harland, R. M. and Wallingford, J. B. (2003). Shroom induces apical constriction and is required for hingepoint formation during neural tube closure. *Current biology* **13**, 2125-2137.

Hansen, M., Kurinczuk, J. J., Bower, C. and Webb, S. (2002). The risk of major birth defects after intracytoplasmic sperm injection and in vitro fertilization. *New England Journal of Medicine* **346**, 725-730.

Haraguchi, H., Saito-Fujita, T., Hirota, Y., Egashira, M., Matsumoto, L., Matsuo, M., Hiraoka, T., Koga, K., Yamauchi, N. and Fukayama, M. (2014). MicroRNA-200a locally attenuates progesterone signaling in the cervix, preventing embryo implantation. *Molecular endocrinology* **28**, 1108-1117.

Hayes, K., Pierson, R., Scraba, S. and Ginther, O. (1985). Effects of estrous cycle and season on ultrasonic uterine anatomy in mares. *Theriogenology* **24**, 465-477.

He, L., Wang, X., Tang, H. L. and Montell, D. J. (2010). Tissue elongation requires oscillating contractions of a basal actomyosin network. *Nature cell biology* **12**, 1133-1142.

Heer, N. C., Miller, P. W., Chanet, S., Stoop, N., Dunkel, J. and Martin, A. C. (2017). Actomyosin-based tissue folding requires a multicellular myosin gradient. *Development* **144**, 1876-1886.

Hildebrand, J. D. and Soriano, P. (1999). Shroom, a PDZ domain–containing actin-binding protein, is required for neural tube morphogenesis in mice. *Cell* **99**, 485-497.

Hiramatsu, R., Matsuoka, T., Kimura-Yoshida, C., Han, S.-W., Mochida, K., Adachi, T., Takayama, S. and Matsuo, I. (2013). External mechanical cues trigger the establishment of the anterior-posterior axis in early mouse embryos. *Developmental cell* **27**, 131-144.

Hiraoka, T., Hirota, Y., Fukui, Y., Gebril, M., Kaku, T., Aikawa, S., Hirata, T., Akaeda, S., Matsuo, M. and Haraguchi, H. (2020). Differential roles of uterine epithelial and stromal STAT3 coordinate uterine receptivity and embryo attachment. *Scientific reports* **10**, 1-12.

Holz, O., Apel, D., Steinmetz, P., Lange, E., Hopfenmüller, S., Ohler, K., Sudhop, S. and Hassel, M. (2017). Bud detachment in hydra requires activation of fibroblast growth factor receptor and a rho–rock–myosin ii signaling pathway to ensure formation of a basal constriction. *Developmental Dynamics* **246**, 502-516.

Hughes, A. J., Miyazaki, H., Coyle, M. C., Zhang, J., Laurie, M. T., Chu, D., Vavrušová, Z., Schneider, R. A., Klein, O. D. and Gartner, Z. J. (2018). Engineered tissue folding by mechanical compaction of the mesenchyme. *Developmental cell* **44**, 165-178. e166.

Jansen, A. and Andermann, E. (2005). Genetics of the polymicrogyria syndromes. *Journal of medical genetics* **42**, 369-378.

Jansen, C. H., Kastelein, A. W., Kleinrouweler, C. E., Van Leeuwen, E., De Jong, K. H., Pajkrt, E. and Van Noorden, C. J. (2020). Development of placental abnormalities in location and anatomy. *Acta obstetricia et gynecologica Scandinavica* **99**, 983-993.

Jobe, A. J. (1999). The new BPD: an arrest of lung development. *Pediatric research* **46**, 641-641.

Jokubkiene, L., Sladkevicius, P. and Valentin, L. (2015). Appearance of the endometrium at saline contrast sonohysterography in the luteal phase of the menstrual cycle: a prospective observational study. *Ultrasound in Obstetrics & Gynecology* **45**, 339-345.

Kim, H. Y., Pang, M.-F., Varner, V. D., Kojima, L., Miller, E., Radisky, D. C. and Nelson, C. M. (2015). Localized smooth muscle differentiation is essential for epithelial bifurcation during branching morphogenesis of the mammalian lung. *Developmental Cell* **34**, 719-726.

Kim, S.-M. and Kim, J.-S. (2017). A review of mechanisms of implantation. *Development & reproduction* **21**, 351.

Kirby, D., Potts, D. and Wilson, I. (1967). On the orientation of the implanting blastocyst. *Development* **17**, 527-532.

Koyama, H., Shi, D., Suzuki, M., Ueno, N., Uemura, T. and Fujimori, T. (2016). Mechanical regulation of three-dimensional epithelial fold pattern formation in the mouse oviduct. *Biophysical journal* **111**, 650-665.

Kähn, W., Leidl, W. and Rienmüller, R. (1989). The chambers of the bovine uterus during early pregnancy. A comparative morphologic, sonographic and nuclear spin tomographic findings. *Zentralblatt fur Veterinarmedizin. Reihe A* **36**, 641-652.

Large, M. J. and DeMayo, F. J. (2012). The regulation of embryo implantation and endometrial decidualization by progesterone receptor signaling. *Molecular and cellular endocrinology* **358**, 155-165.

Lee, M., Ahn, J. I., Lee, A. R., Ko, D. W., Yang, W. S., Lee, G., Ahn, J. Y. and Lim, J. M. (2017). Adverse effect of superovulation treatment on maturation, function and ultrastructural integrity of murine oocytes. *Molecules and cells* **40**, 558.

Leone, F., Timmerman, D., Bourne, T., Valentin, L., Epstein, E., Goldstein, S., Marret, H., Parsons, A., Gull, B. and Istre, O. (2010). Terms, definitions and measurements to describe the sonographic features of the endometrium and intrauterine lesions: a consensus opinion from the International Endometrial Tumor Analysis (IETA) group. *Ultrasound in Obstetrics and Gynecology: The Official Journal of the International Society of Ultrasound in Obstetrics and Gynecology* **35**, 103-112.

Liang, Y.-X., Liu, L., Jin, Z.-Y., Liang, X.-H., Fu, Y.-S., Gu, X.-W. and Yang, Z.-M. (2018). The high concentration of progesterone is harmful for endometrial receptivity and decidualization. *Scientific reports* **8**, 1-12.

Lohmann, I., McGinnis, N., Bodmer, M. and McGinnis, W. (2002). The Drosophila Hox gene deformed sculpts head morphology via direct regulation of the apoptosis activator reaper. *Cell* **110**, 457-466.

Lydon, J. P., DeMayo, F. J., Funk, C. R., Mani, S. K., Hughes, A. R., Montgomery, C., Shyamala, G., Conneely, O. M. and O'Malley, B. W. (1995). Mice lacking progesterone receptor exhibit pleiotropic reproductive abnormalities. *Genes & development* **9**, 2266-2278.

Mackens, S., Santos-Ribeiro, S., Van De Vijver, A., Racca, A., Van Landuyt, L., Tournaye, H. and Blockeel, C. (2017). Frozen embryo transfer: a review on the optimal endometrial preparation and timing. *Human Reproduction* **32**, 2234-2242.

Maheshwari, A., Pandey, S., Shetty, A., Hamilton, M. and Bhattacharya, S. (2012). Obstetric and perinatal outcomes in singleton pregnancies resulting from the transfer of frozen thawed versus fresh embryos generated through in vitro fertilization treatment: a systematic review and meta-analysis. *Fertility and sterility* **98**, 368-377. e369.

Manjón, C., Sánchez-Herrero, E. and Suzanne, M. (2007). Sharp boundaries of Dpp signalling trigger local cell death required for Drosophila leg morphogenesis. *Nature Cell Biology* **9**, 57-63.

Marquardt, R. M., Kim, T. H., Shin, J.-H. and Jeong, J.-W. (2019). Progesterone and estrogen signaling in the endometrium: what goes wrong in endometriosis? *International journal of molecular sciences* **20**, 3822.

Martin, A. C. and Goldstein, B. (2014). Apical constriction: themes and variations on a cellular mechanism driving morphogenesis. *Development* **141**, 1987-1998.

Martin, A. C., Kaschube, M. and Wieschaus, E. F. (2009). Pulsed contractions of an actin–myosin network drive apical constriction. *Nature* **457**, 495-499.

Matsuo, I. and Hiramatsu, R. (2017). Mechanical perspectives on the anterior-posterior axis polarization of mouse implanted embryos. *Mechanisms of development* **144**, 62-70.

McLAREN, A. and Michie, D. (1959). Superpregnancy in the Mouse: 1. Implantation and Foetal Mortality After Induced Superovulation in Females of Various Ages. *Journal of Experimental Biology* **36**, 281-284.

Mesen, T. B. and Young, S. L. (2015). Progesterone and the luteal phase: a requisite to reproduction. *Obstetrics and Gynecology Clinics* **42**, 135-151.

Mirkin, S., Nikas, G., Hsiu, J.-G., Díaz, J. and Oehninger, S. (2004). Gene expression profiles and structural/functional features of the peri-implantation endometrium in natural and gonadotropin-stimulated cycles. *The Journal of Clinical Endocrinology & Metabolism* **89**, 5742-5752.

Monier, B., Gettings, M., Gay, G., Mangeat, T., Schott, S., Guarner, A. and Suzanne, M. (2015). Apico-basal forces exerted by apoptotic cells drive epithelium folding. *Nature* **518**, 245-248.

Nikas, G., Develioglu, O. H., Toner, J. P. and Jones Jr, H. W. (1999). Endometrial pinopodes indicate a shift in the window of receptivity in IVF cycles. *Human Reproduction* **14**, 787-792.

Nishimura, T. and Takeichi, M. (2008). Shroom3-mediated recruitment of Rho kinases to the apical cell junctions regulates epithelial and neuroepithelial planar remodeling.

Njogu, A., Owiti, G. O. a., Oduor-Okelo, D., NJOGU, A., OWITI, G. and ODUOR-OKELO, D. (2013). Uterine Gland Microstructure in the Pregnant and the Non-pregnant Lesser Galago (Galago senegalensis). *Int. J. Morphol* **31**, 771-776.

Ossipova, O., Kim, K., Lake, B. B., Itoh, K., Ioannou, A. and Sokol, S. Y. (2014). Role of Rab11 in planar cell polarity and apical constriction during vertebrate neural tube closure. *Nature communications* **5**, 3734.

Pandey, S., Shetty, A., Hamilton, M., Bhattacharya, S. and Maheshwari, A. (2012). Obstetric and perinatal outcomes in singleton pregnancies resulting from IVF/ICSI: a systematic review and meta-analysis. *Human reproduction update* **18**, 485-503.

Pawar, S., Laws, M., Bagchi, I. and Bagchi, M. (2015). Uterine epithelial estrogen receptor-α controls decidualization via a paracrine mechanism. *Molecular endocrinology* **29**, 1362-1374.

Pelkonen, S., Koivunen, R., Gissler, M., Nuojua-Huttunen, S., Suikkari, A.-M., Hydén-Granskog, C., Martikainen, H., Tiitinen, A. and Hartikainen, A.-L. (2010). Perinatal outcome of children born after frozen and fresh embryo transfer: the Finnish cohort study 1995–2006. *Human Reproduction* **25**, 914-923.

Petracco, Á., Azambuja, R., Okada, L., Michelon, J., Oliani, A. and Badalotti, M. (2006). Comparison of embryo quality between sibling embryos originating from frozen or fresh oocytes. *Reproductive biomedicine online* **13**, 497-503.

Plageman Jr, T. F., Chung, M.-I., Lou, M., Smith, A. N., Hildebrand, J. D., Wallingford, J. B. and Lang, R. A. (2010). Pax6-dependent Shroom3 expression regulates apical constriction during lens placode invagination. *Development* **137**, 405-415.

Prapas, Y., Prapas, N., Jones, E., Duleba, A., Olive, D., Chatziparasidou, A. and Vlassis, G. (1998). The window for embryo transfer in oocyte donation cycles depends on the duration of progesterone therapy. *Human reproduction (Oxford, England)* **13**, 720-723.

Qu, Y., Zhang, J., Guo, S., Zhang, L., Qian, J., Zhu, X., Duan, E. and Zhang, Y. (2022). Three-Dimensional Visualization of Mouse Endometrial Remodeling After Superovulation. *Frontiers in Cell and Developmental Biology* **10**.

Rasweiler IV, J. and Badwaik, N. (1999). Relationships Between Orientation of the Blastocyst During Implantation, Position of the Chorioallantoic Placenta, and Vascularization of the Uterus in the Noctilionoid BatsCarollia perspicillataandNoctiliosp. *Placenta* **20**, 241-255.

Ray, R. P., Ganguly, P. S., Alt, S., Davis, J. R., Hoppe, A., Tapon, N., Salbreux, G. and Thompson, B. J. (2018). Apical and basal matrix remodeling control epithelial morphogenesis. *Developmental cell* **46**, 23-39. e25.

Renner-Martin, T., Forstenpointner, G., Weissengruber, G. and Eberhardt, L. (2009). Gross anatomy of the female genital organs of the domestic donkey (Equus asinus Linné, 1758). *Anatomia, histologia, embryologia* **38**, 133-138.

Richter, K. S., Shipley, S. K., McVearry, I., Tucker, M. J. and Widra, E. A. (2006). Cryopreserved embryo transfers suggest that endometrial receptivity may contribute to reduced success rates of later developing embryos. *Fertility and sterility* **86**, 862-866.

Rider, V., Talbott, A., Bhusri, A., Krumsick, Z., Foster, S., Wormington, J. and Kimler, B. F. (2016). WINGLESS (WNT) signaling is a progesterone target for rat uterine stromal cell proliferation. *The Journal of endocrinology* **229**, 197.

Robertshaw, I., Bian, F. and Das, S. (2016). Mechanisms of uterine estrogen signaling during early pregnancy in mice: an update. *Journal of molecular endocrinology* **56**, R127-R138.

Roellig, D., Theis, S., Proag, A., Allio, G., Bénazéraf, B., Gros, J. and Suzanne, M. (2022). Force-generating apoptotic cells orchestrate avian neural tube bending. *Developmental Cell* **57**, 707-718. e706.

Roque, M., Valle, M., Guimarães, F., Sampaio, M. and Geber, S. (2015). Freeze-all policy: fresh vs. frozen-thawed embryo transfer. *Fertility and sterility* **103**, 1190-1193.

Ryu, Y. K., Collins, S. E., Ho, H.-Y. H., Zhao, H. and Kuruvilla, R. (2013). An autocrine Wnt5a-Ror signaling loop mediates sympathetic target innervation. *Developmental biology* **377**, 79-89.

Samper, J. C. (2010). A review of a practitioner’s perspective on endometrial edema. *Pferdeheilkunde* **26**, 14-18.

Sato, T., Stange, D. E., Ferrante, M., Vries, R. G., Van Es, J. H., Van Den Brink, S., Van Houdt, W. J., Pronk, A., Van Gorp, J. and Siersema, P. D. (2011). Long-term expansion of epithelial organoids from human colon, adenoma, adenocarcinoma, and Barrett's epithelium. *Gastroenterology* **141**, 1762-1772.

Scherle, P. A., Ma, W.-g., Lim, H., Dey, S. K. and Trzaskos, J. M. (2000). Regulation of cyclooxygenase-2 induction in the mouse uterus during decidualization: an event of early pregnancy. *Journal of Biological Chemistry* **275**, 37086-37092.

Shi, D., Komatsu, K., Hirao, M., Toyooka, Y., Koyama, H., Tissir, F., Goffinet, A. M., Uemura, T. and Fujimori, T. (2014). Celsr1 is required for the generation of polarity at multiple levels of the mouse oviduct. *Development* **141**, 4558-4568.

Shyer, A. E., Tallinen, T., Nerurkar, N. L., Wei, Z., Gil, E. S., Kaplan, D. L., Tabin, C. J. and Mahadevan, L. (2013). Villification: how the gut gets its villi. *Science* **342**, 212-218.

Silva, L. and Ginther, O. (2006). An early endometrial vascular indicator of completed orientation of the embryo and the role of dorsal endometrial encroachment in mares. *Biology of reproduction* **74**, 337-343.

Simon, C., Cano, F., Valbuena, D., Remohi, J. and Pellicer, A. (1995). Clinical evidence for a detrimental effect on uterine receptivity of high serum oestradiol concentrations in high and normal responder patients. *Human Reproduction* **10**, 2432-2437.

Slezak, P. and Tillinger, K.-G. (1973). The occurrence and significance of broad longitudinal folds in the uterine cavity at hysterography. *Radiology* **106**, 87-90.

Sokol, E. (2011). Clinical anatomy of the uterus, fallopian tubes, and ovaries. *Global Library of Women’s Medicine, ISSN*, 1756-2228.

Soyal, S. M., Mukherjee, A., Lee, K. Y. S., Li, J., Li, H., DeMayo, F. J. and Lydon, J. P. (2005). Cre-mediated recombination in cell lineages that express the progesterone receptor. *genesis* **41**, 58-66.

Strug, M. R., Su, R. W., Kim, T. H., Mauriello, A., Ticconi, C., Lessey, B. A., Young, S. L., Lim, J. M., Jeong, J. W. and Fazleabas, A. T. (2018). RBPJ mediates uterine repair in the mouse and is reduced in women with recurrent pregnancy loss. *The FASEB Journal* **32**, 2452-2466.

Takeda, M., Sami, M. M. and Wang, Y.-C. (2018). A homeostatic apical microtubule network shortens cells for epithelial folding via a basal polarity shift. *Nature cell biology* **20**, 36-45.

Tan, J., Paria, B. C., Dey, S. K. and Das, S. K. (1999). Differential uterine expression of estrogen and progesterone receptors correlates with uterine preparation for implantation and decidualization in the mouse. *Endocrinology* **140**, 5310-5321.

Thiyagarajan, D. K., Basit, H. and Jeanmonod, R. (2021). Physiology, menstrual cycle. In *StatPearls [Internet]*: StatPearls Publishing.

Tozluoğlu, M. and Mao, Y. (2020). On folding morphogenesis, a mechanical problem. *Philosophical Transactions of the Royal Society B* **375**, 20190564.

Tozluoğlu, M., Duda, M., Kirkland, N. J., Barrientos, R., Burden, J. J., Munoz, J. J. and Mao, Y. (2019). Planar differential growth rates initiate precise fold positions in complex epithelia. *Developmental cell* **51**, 299-312. e294.

Trushko, A., Di Meglio, I., Merzouki, A., Blanch-Mercader, C., Abuhattum, S., Guck, J., Alessandri, K., Nassoy, P., Kruse, K. and Chopard, B. (2020). Buckling of an epithelium growing under spherical confinement. *Developmental cell* **54**, 655-668. e656.

Tu, Z., Wang, Q., Cui, T., Wang, J., Ran, H., Bao, H., Lu, J., Wang, B., Lydon, J. and DeMayo, F. (2016). Uterine RAC1 via Pak1-ERM signaling directs normal luminal epithelial integrity conducive to on-time embryo implantation in mice. *Cell Death & Differentiation* **23**, 169-181.

Ueda, Y., Kimura-Yoshida, C., Mochida, K., Tsume, M., Kameo, Y., Adachi, T., Lefebvre, O., Hiramatsu, R. and Matsuo, I. (2020). Intrauterine pressures adjusted by Reichert's membrane are crucial for early mouse morphogenesis. *Cell Reports* **31**, 107637.

Uffelmann, E., Huang, Q. Q., Munung, N. S., De Vries, J., Okada, Y., Martin, A. R., Martin, H. C., Lappalainen, T. and Posthuma, D. (2021). Genome-wide association studies. *Nature Reviews Methods Primers* **1**, 59.

Van der Auwera, I. and D'Hooghe, T. (2001). Superovulation of female mice delays embryonic and fetal development. *Human reproduction* **16**, 1237-1243.

Varga, I., Kachlík, D., Žišková, M. and Miko, M. (2018). Lymphatic lacunae of the mucosal folds of human uterine tubes—A rediscovery of forgotten structures and their possible role in reproduction. *Annals of Anatomy-Anatomischer Anzeiger* **219**, 121-128.

Veerati, P. C., Mitchel, J. A., Reid, A. T., Knight, D. A., Bartlett, N. W., Park, J.-A. and Grainge, C. L. (2020). Airway mechanical compression: its role in asthma pathogenesis and progression. *European Respiratory Review* **29**.

Visetsouk, M. R., Falat, E. J., Garde, R. J., Wendlick, J. L. and Gutzman, J. H. (2018). Basal epithelial tissue folding is mediated by differential regulation of microtubules. *Development* **145**, dev167031.

Wang, L., Heffner, C., Vong, K. I., Barrows, C., Ha, Y.-J., Lee, S., Lara-Gonzalez, P., Jhamb, I., Van Der Meer, D. and Loughnan, R. (2023). TMEM161B modulates radial glial scaffolding in neocortical development. *Proceedings of the National Academy of Sciences* **120**, e2209983120.

Wang, Y.-C., Khan, Z., Kaschube, M. and Wieschaus, E. F. (2012). Differential positioning of adherens junctions is associated with initiation of epithelial folding. *Nature* **484**, 390-393.

Weng, M. and Wieschaus, E. (2017). Polarity protein Par3/Bazooka follows myosin-dependent junction repositioning. *Developmental biology* **422**, 125-134.

Wiggs, B. R., Hrousis, C. A., Drazen, J. M. and Kamm, R. D. (1997). On the mechanism of mucosal folding in normal and asthmatic airways. *Journal of Applied Physiology* **83**, 1814-1821.

Wilcox, A. J., Weinberg, C. R., O'Connor, J. F., Baird, D. D., Schlatterer, J. P., Canfield, R. E., Armstrong, E. G. and Nisula, B. C. (1988). Incidence of early loss of pregnancy. *New England Journal of Medicine* **319**, 189-194.

Winkelmann, A. and Spornitz, U. (1997). Alkaline phosphatase distribution in rat endometrial epithelium during early pregnancy: a scanning electron-microscopic study. *Cells Tissues Organs* **158**, 237-246.

Winuthayanon, W., Hewitt, S. C., Orvis, G. D., Behringer, R. R. and Korach, K. S. (2010). Uterine epithelial estrogen receptor α is dispensable for proliferation but essential for complete biological and biochemical responses. *Proceedings of the National Academy of Sciences* **107**, 19272-19277.

Winuthayanon, W., Lierz, S. L., Delarosa, K. C., Sampels, S. R., Donoghue, L. J., Hewitt, S. C. and Korach, K. S. (2017). Juxtacrine activity of estrogen receptor α in uterine stromal cells is necessary for estrogen-induced epithelial cell proliferation. *Scientific reports* **7**, 1-15.

Xia, X., Zhang, Y., Cao, M., Yu, X., Gao, L., Qin, L., Wu, W., Cui, Y. and Liu, J. (2023). Adverse effect of assisted reproductive technology-related hyperoestrogensim on the secretion and absorption of uterine fluid in superovulating mice during the peri-implantation period. *Frontiers in Endocrinology* **14**.

Yoshinaga, K. (2013). A sequence of events in the uterus prior to implantation in the mouse. *Journal of assisted reproduction and genetics* **30**, 1017-1022.

Yuan, J., Cha, J., Deng, W., Bartos, A., Sun, X., Ho, H.-Y. H., Borg, J.-P., Yamaguchi, T. P., Yang, Y. and Dey, S. K. (2016). Planar cell polarity signaling in the uterus directs appropriate positioning of the crypt for embryo implantation. *Proceedings of the National Academy of Sciences* **113**, E8079-E8088.

Yuan, J., Deng, W., Cha, J., Sun, X., Borg, J.-P. and Dey, S. K. (2018). Tridimensional visualization reveals direct communication between the embryo and glands critical for implantation. *Nature communications* **9**, 1-13.

Zallen, J. A. (2007). Planar polarity and tissue morphogenesis. *Cell* **129**, 1051-1063.

Zhang, S., Kong, S., Wang, B., Cheng, X., Chen, Y., Wu, W., Wang, Q., Shi, J., Zhang, Y. and Wang, S. (2014). Uterine Rbpj is required for embryonic-uterine orientation and decidual remodeling via Notch pathway-independent and-dependent mechanisms. *Cell research* **24**, 925-942.

APPENDIX

Publications

1. **Manoj Madhavan**, Francesco DeMayo, John Lydon, Niraj Joshi, Asgerally Fazleabas, and Ripla Arora. (2022). Aberrant uterine folding in mice disrupts implantation chamber formation and embryo-uterine axes alignment. *Development*. doi:10.1242/dev.200300.
2. **Manoj Madhavan**, Ripla Arora. (2022). Tracing early postnatal lineage of progesterone receptor in the mouse uterus. Mol Reprod Dev, DOI: 10.1002/mrd.23557.
3. **Manoj Madhavan**, Kaylie Chiles, Madeline Dawson, Ripla Arora. Elevated Estrogen levels during hyperstimulation cause disrupted uterine folding and embryo-uterine axes alignment. (under preparation).
4. Diana Flores, **Manoj Madhavan**, Savannah Wright, Ripla Arora. (2020). Mechanical and signaling mechanisms that guide pre-implantation embryo movement. *Development* 147, doi:10.1242/dev.193490.
5. Hannah Lufkin, Diana Flores, Zachary Raider, **Manoj Madhavan**, Madeline Dawson, Anna Coronel, Dhruv Sharma, Ripla Arora. (2022). Pre-implantation mouse embryo movement under hormonally altered conditions. *Molecular Human Reproduction*. https://doi.org/10.1093/molehr/gaac043.
6. Xu QX, **Madhavan M**, Wei SW, Zhang WQ, Lu L, Wang KZ, Zhao Y, Shao HT, Kang JW, Fazleabas AT, Arora R, Su RW. (2023). Aberrant activation of Notch1 signaling in the mouse uterine epithelium promotes hyperplasia by increasing estrogen sensitivity. FASEB J.

Conference Presentations

1. Poster presentation at Michigan Alliance for Reproductive Technologies (2019)
2. Poster presentation at IQ research day (2019)
3. Oral Presentation at Midwest meeting for the Society for Developmental Biology, Case Western Reserve University (2019)

4. Poster presentation at Annual meeting for the Society for Developmental Biology, Virtual (2020)
5. Oral Presentation at Reproductive and Developmental Sciences Annual Research Day (2020)
6. Oral presentation at virtual IQ imaging symposium (2021)
7. Poster presentation at Flatiron Institute Turing symposium, New York (2022)